Master of Science Thesis

Advanced Optoelectronics Driver System for Biomedical Application

Shanliang Deng

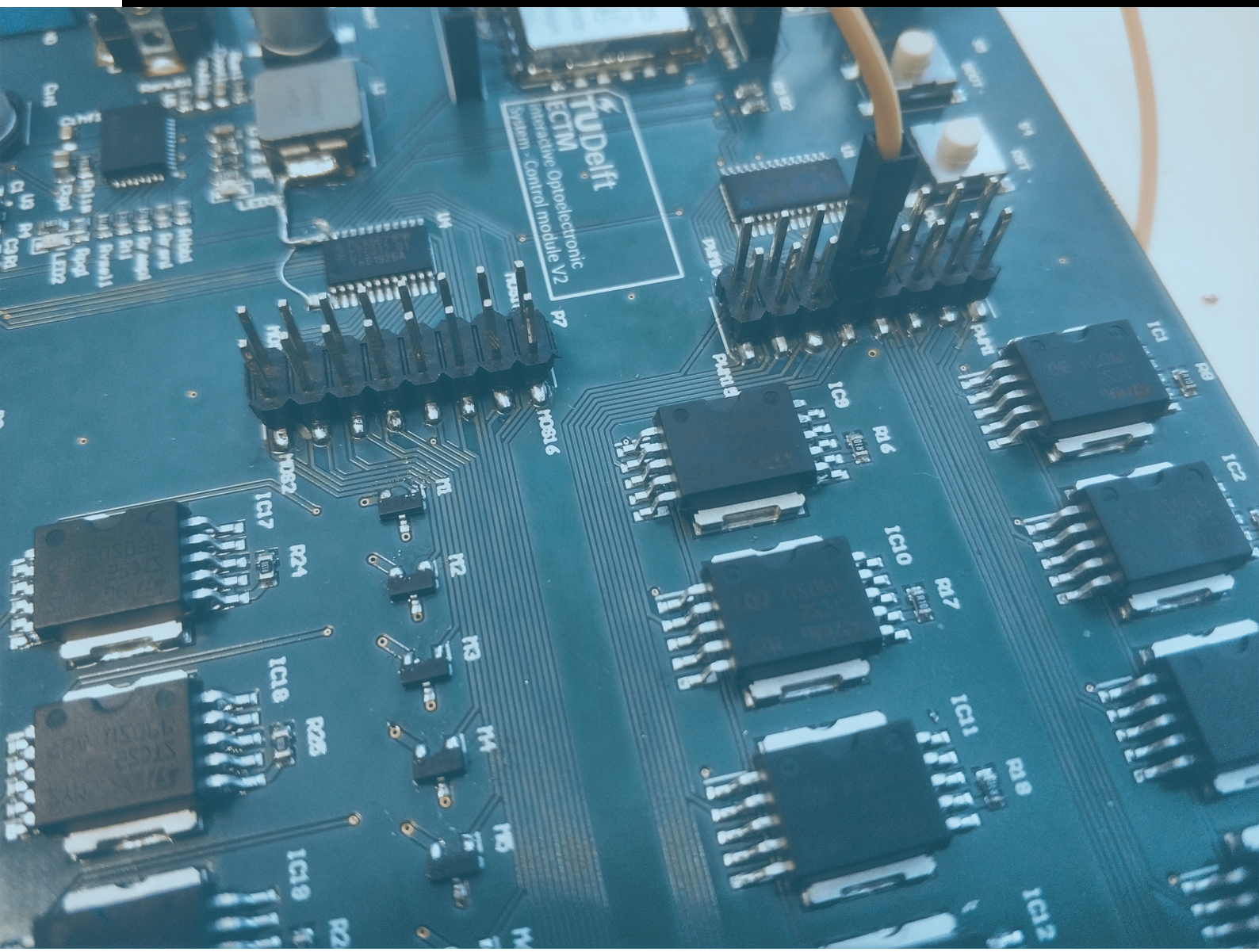

Electronic Components, Technology and Materials

TU Delft

ADVANCED OPTOELECTRONICS DRIVER SYSTEM FOR BIOMEDICAL APPLICATION

A thesis submitted to the Delft University of Technology in partial fulfillment
of the requirements for the degree of

Master of Science in Microelectronics

by

Shanliang Deng

May 2021

Shanliang Deng: *Advanced optoelectronics driver system for biomedical application* (2021)

The work in this thesis was made in the:

Electronic Components, Technology and Materials
Department of Microelectronics
Faculty of Electrical Engineering, Mathematics &
Computer Science
Delft University of Technology

Supervisors:	Prof. dr. ir. G.Q. Zhang, TU Delft, supervisor
	Dr. ir. R.H. Poelma, Nexperia, supervisor
	T. Jing, TU Delft, Daily supervisor
Committee:	Dr. ir. A. Bossche, TU Delft

This thesis is confidential and cannot be made public until May 31, 2023.

ABSTRACT

With the development of biomedical technology such as optogenetics, optoelectronics devices, especially light-emitting diode(LED), becomes wildly used in biomedical researches and applications. Unlike traditional illumination and display applications, biomedical applications have more unique requirements like intensity and response speed. The existing optoelectronics systems cannot fulfill all the requirements of biomedical applications. It is essential to design particular light sources and drivers to fill the blank area of biomedical-compatible optoelectronics systems. However, each biomedical application has its environment and setup. One specific optoelectronics system will not suitable for all circumstances. This work focuses on *developing a methodology to design advanced optoelectronics driver systems for biomedical applications* to solve this problem.

It takes three steps to develop and verify the driver design methodology. The first step is producing a high-power biomedical array driving system to verify the array control strategy. UVC virus inactivation test platform, which successfully finishes virus inactivation test in Erasmus MC, is produced in this step. The second step is extending the array driver to the matrix driver. An interactive optoelectronics system is designed to perform optogenetics experiments in LUMC. Finally, aiming at the ultimate goal-implantable, self-powered driver feasibility research is performed to prove it is feasible to design a self-power optoelectronics driver system in the future.

Keywords: smart driver, biomedical electronices, high power LED driver, matrix control, system intergration

ACKNOWLEDGMENTS

I want to express my gratitude to Prof. G.Q Zhang for providing me this research topic and financial support. Thanks to Dr. D.A. Pijnappels and N.Harlaar from LUMC (Netherlands) for optogenetics experiments. M.R. Pronk from Erasmus MC (Netherlands) for virus inactivation experiments. Special thanks to *TU Delft COVID-19 Response Fund* for supporting this thesis work.

Shanliang Deng
May, 2021

CONTENTS

LIST OF FIGURES

LIST OF TABLES

ACRONYMS

UV Ultraviolet
LED Light-emitting diode
PWM Plus-width modulation
COB Chip-on-board
ASIC Application-specific integrated circuit
DOE Design of experiment
UI User interface
LUMC Leiden university medical center
NG Nanogenertor
PCB Print circuit board
MCU Microcontroller unit
IIC Inter-integrated circuit communication protocol
CCS Constant current source
FFC Flat flex cable
OP Operation point
SMD Surface mount device
AF Atrial fibrillation
AI Artificial intelligence
DLP Digital light processing
PC Personal computer
RAM Random-access memory
GPIO General-purpose input/output
SPI Serial peripheral interface bus
API Application programming interface
PMOS P-channel metal–oxide–semiconductor
WPT Wireless power transfer
TENG Triboelectric nanogenerato
ECG Electrocardiogram
PENG Piezoelectric nanogenerator
AC Alternate current
DC Direct current

1 INTRODUCTION

1.1 PROBLEMS AND OBJECTIVE

1.1.1 Problems

Even though there are many commercially available dedicated LED drivers, suitable LED driver systems for biomedical application are still a blank area. Because biomedical application has the following requirements:

1 Quick response speed. Optogenetics modified cells react to light in milliseconds time level[1].

2 Enough intensity. UVC virus inactivation test requires a certain amount of light intensity to inactivate the virus[2]. Optogenetics experiments also require enough intensity to excite the ion channels[1].

3 Precise control. Biomedical application is sensitive to optical dose, which is time times intensity. The system should control the time and output power precisely[3].

4 Complex logic. A biomedical experiment requires different experimental protocols. The driver system should able to set logic according to DOE.

5 Customized pattern. Pattern optimization is important in optogenetics to improve the efficiency of some applications.

6 User friendly. Biomedical researchers are not familiar with electrical engineering. So the driver system should make the connection as simple as possible with a user-friendly UI to avoid any complex programming.

7 Self-powered. The biomedical application's ultimate goal is in-vivo and wearable long-term monitoring where power cables are not feasible anymore[4].

The existing LED drivers listed in the state-of-the-art part can only fulfill one or two requirements stated above. As a result, an advanced optoelectronics driver system is necessary to be developed to fill the blank of LED drivers for biomedical applications.

1.1.2 Objective

In this thesis work, *research into the methodology of developing an advanced optoelectronics system for biomedical application* will be conducted in three steps. In each step, part of the requirements stated in motivation will be fulfilled. At the end of this thesis work, an advanced driver system that covers all the requirements will be designed. A demonstration system or system design should be developed to fulfill a specified biomedical application to verify the design by doing each step. This thesis's novelty is the first design strategy research of optoelectronics drivers focusing on biomedical application to fill the blank area of current optoelectronics drivers.

The first step is designing an array driving system. This system will be used to perform a virus inactivation test using UVC LED. To reach the requirement of the virus inactivation test, the system needs to fulfill the first four and user-friendly requirements. The second step is to expand array control system to matrix control system to realize the customized pattern requirement. This system is used to stimulate optogenetic modified epicardium cell layers. Finally, self-power system research will be done, seeking available solutions to power up the system for future in-vivo applications.

1.2 BACKGROUND

1.2.1 Introduction of optoelectronics

Opto-electronics is the electronics devices and system which generate, control, and detect light. In this context, light covers invisible radiation like X-ray, ultraviolet (UV), and infrared, adding visible light. Opto-electronic devices are transducers that convert electrical to optical vice versa or instruments using such devices in their operation [5]. Technically speaking, all kinds of light sources used in daily life can be considered as optoelectronics devices and systems. To control and power up these optoelectronics devices suitable driver system is required. In the electronics field, a driver is a certain circuit that controls other circuits or components, such as high-power transistors, current sources, and numerous others.

1.2.2 History of optics in the biomedical field

Early in 1878, short-wavelength light has fund has the sterilization effect[6]. UV has been known as mutagen at the cell level for more than a hundred years. Since 1980, light has been first discovered to help treat diseases such as winter depression[7, 8, 9] and shift circadian rhythms[10, 11]. In later years, more and more opto-biomedical effects have been found. In 1987, Red light was found can accelerate

wound healing[12]. In 1997, the combination of blue and red light was found can treat acne vulgaris[13]. With the development of modern optoelectronics and biomedical technology, new light sources like LEDs and new biomedical techniques like genetic engineering give this combination even broader application scenarios.

1.2.3 Solid-state optoelectronics

Light-emitting diode (LED) is a solid-state light source emitting light when current flows through it. Recombination of excited electrons and electron holes in semiconductors releasing energy in the form of photons. The emitted light color is determined by the bandgap energy of semiconductor material consisting of the LED[14] using Planck's Equation 1.1.

$$E = h\frac{c}{\lambda} \tag{1.1}$$

Where E stands for the bandgap energy (in J) in semiconductor, h is Plank's constant, c is the light speed in vacuum, and λ is wavelength. For example, *GaP* has a bandgap of 2.19 eV, using Equation 1.1, the emitted light wavelength should be 566nm, which is green. Use a different kind of semiconductors or a layer of light-emitting phosphor on the semiconductor device, LEDs can have multiple emit wavelengths from UVC (250 nm) to infrared (1100 nm). Table 1.1 lists some common LED wavelengths together with their semiconductor materials and possible biomedical applications.

Peak wavelength	Color	Materials	Possible biomedical application
>760	Infrared	AlGaAs	Oral mucositis[15], Hair removal[16]
730	Infrared	GaAs	Mucositis prevention, wound healing, and tissue repair [17]
700	Red	GaP:Zn–O	Low level light therapy[18]
660	Red	$GaAlo.35Aso.65$	Allergic rhinitis treatment[19], incision recovering[20]
610	Orange	$GaAso.25Po.75$:N	Wound healing[11]
590	Yellow	$GaAso.15Po.85$:N	
565	Green	GaP:N	
530	Green	AlGaInN	
500	Green	InGaN	Treatment of seasonal affective disorder[21]
450	Blue	GaN	Optogenetics trigger, deep brain trigger[22]
400	UVA	AlGaN	Water and air purification[2]
210-400	UVB-UVC	AlGaInN	Virus inactivation[23]

Table 1.1: Some common LED wavelengths and possible biomedical applications

Comparing to other conventional optoelectronic light sources such as incandescent bulbs, chemical gas tubes, and fluorescent lamps, LEDs have many advantages over them, listed below.

- Lifetime: LEDs have a theoretical estimated 35,000 to 50,000 hour lifetime. In real usage, commercial LEDs have an average of 3,600 to 6,000 hours of lifetime[24].

- Efficiency: LEDs' energy conversion efficiency is much higher than other light sources[25] and not affected by shape and size.

- Robustness: Because LEDs are solid-state light sources manufactured with semiconductor processes, the physical robustness is much better. External vibration and drop will not easily damage LEDs.

- Size: The size of LEDs is much smaller than conventional light sources. The smallest LED can be in micrometers.[26] So, LEDs can be easily attached to any circuits.

- Switching speed: LED can be switch on and off at a very high speed (over 1 MHz). Thus, LEDs can be easily dimmed precisely by pulse-width modulation (PWM). Moreover, this feature will not affect the LED's lifetime, unlike most other kinds of light sources.

As a result, in modern optical biomedical applications, LEDs are the first-choice light source[27].

Different from other light sources, LED is a current-driven low voltage device. According to *the Shockley diode equation* 1.2,

$$I = I_s \left(e^{\frac{V_D}{nV_T}} - 1 \right) \tag{1.2}$$

where I is the current through the LED and V_D is the voltage across the LED, the current through an LED rises exponentially with the voltage applied to it, meaning a small change in voltage will lead to a large current change. To prevent damage and manage output power precisely, LED must be driven by dedicated LED drivers such as constant current drivers (CCS).

1.3 STATE-OF-ART

1.3.1 Industrial LED drivers

Lighting LED drives

This type of LED driver is aiming to drive super high power LEDs. Usually in lighting applications. Multiple LEDs will connect in series to keep the current through each LED is the same, controlled by the driver. For example, to reach the required illumination intensity, 20 W, 20 LEDs (3.3 V, 300 mA) will be connected to the driver in series using a driving voltage over 60V. The output voltage range of this kind of driver usually very high, and the current is equal to the operation current of one LED. Large scale LED manufactures like *Signify* and *Philips* have a large number of similar products shown in Figure 1.1a.

Moreover, to reach a stable output performance, lighting drivers have large output capacitors to avoid flashing[28], leading to the lack of switching ability. The enclosure of this type of driver is a sealed plastic or metal box of large size. Each driver usually only have 1 output channel except some high-end model.

(a) (b)

Figure 1.1: (a)Lighting LED driver produced by *Signify* (b)Laboratory LED driver produced by *Thorlabs Inc.*

Indication LED driver

Indication LED drivers are usually in the form of chips and have multiple output channels which can drive LED arrays. Each channel's output capacity is fixed to drive low power single LED, whose operation current is below 20 mA. External

controllers can connect to these drivers to realize control logic. The internal or external clock signal can provide a PWM output function to control the output power. Semiconductor manufactures like *NXP* and *TI* has different models of indication LED driver.

1.3.2 Specialized LED drivers

Laboratory LED driver

Laboratory LED driver can drive single high power LED. It has a maximum output current of 1.2 A and supports external controller input. By tuning the output current limit, the laboratory LED driver is compatible with different LEDs with different operating currents. External PWM modulation signal can control the output power. However, same as the lighting LED driver. Each driver only has single-channel output. Laboratory instrument providers such as *Thorlabs Inc.* has similar products like Figure 1.1b.

OLED driver

OLED driver has the ability to drive high-density LED matrix like a smartphone screen. OLED chip always in COB packaging and placed on the same substrate of OLED array. However, each output column's drive current is in the microampere level, which is too weak to drive inorganic LED.

ASIC LED driver

In 2019, Zhang et al. developed an ASIC chip using CMOS technology to drive a 64×36 pixel monolithic micro-LED matrix. The driver output current for each column is 30uA[29]. In 2020, semiconductor company *Plessey* developed an ASIC driver for a 384×128 monolithic micro-LED matrix.

1.4 OUTLINE

The system designed for the first step is called *UVC virus inactivation test platform*. This platform will become generic lab equipment to perform virus inactivation tests. In this research, a high-power LED array precise control strategy will be developed. Also, a suitable UI will be designed to interact with users. A series of optical measurements will be performed in Signify to verify the driver capability, followed by a virus inactivation test in Erasmus MC. The advantage and disadvantages of this system will be concluded to help improve the next step.

The matrix optoelectronics driver system will be designed in step two, called *Interactive optoelectronics system*. On the basis of step one, adding scanning function, the array driver will become a matrix driver. This system will drive a pre-designed LED matrix to perform an optogenetics experiment in LUMC. Before the design process, research of suitable matrix control topology and expandable communication methods needs to be finished. Output timing, communication latency, and output light intensity will be measured after the system assembly to verify the system before performing optogenetics experiments. A future matrix driver for micro LEDs matrix will also be designed to drive more advanced LED matrix in the future.

To fulfill the in-vivo optoelectronics application goal, self-powered driver research is necessary to perform. Potential self-power strategies, including nanogenerator (NG) and wireless charging, will be studied in the third step to finding out the possibility of developing self-powered drivers.

Using the three steps mentioned above, a suitable design methodology of advanced optoelectronics driver systems will become available to fill the blank area of LED drivers for biomedical application.

2 UVC VIRUS INACTIVATION TEST PLATFORM

2.1 INTRODUCTION

This chapter will introduce the first step, designing the *UVC Virus Inactivation Test Platform*, by giving a detailed description of the designing process, measurement, and virus inactivation result. In this design, a high-power LED array driver is developed to drive 24 individual UVC LEDs simultaneously with a maximum current of 300 mA each.

2.1.1 Background

Since the beginning of 2020, the outbreak of a kind of coronavirus has disrupted our life greatly. Most virologists' priority is to find out the features of the virus and then to study the method to suppress the spread of the virus. The condition for inactivation of a kind virus is an important aspect of research. There are physical (heat, ultraviolet light, ionizing radiation, and filtration) and chemical methods to reach this purpose[30]. Chemical methods have many side effects because of using toxic chemicals like chlorine, chlorine dioxide, or ozone[31]. Heating and ionizing radiation are not proper inactivation methods under many circumstances like public utilities. Filtration devices required large upfront investment and professional maintenance during operation, which is not feasible for a wide range of applications. More recently, ultraviolet light has drawn large attention for its user-friendly, low cost of equipment, energy-efficient, and easy maintenance[32]. Also, it is safe to apply ultraviolet light with eye and simple skin protections according to ISO 15858:2016.

Ultraviolet (UV) light can be divided into three general types, UVA, UVB, and UVC. Ultraviolet C (UVC) light has been proven an efficient method of inactivation virus. It can alter the genetic information saved in the DNA or RNA, causing organisms such as viruses to be incapable of replicating[33]. It has a wavelength range from 100 nm to 280 nm, which is shorter than UVA and UVB. According to Planck–Einstein relation, Equation 2.1, light with a shorter wavelength has higher energy[34]. As a result, UVC has the highest energy in UV light with better virus

inactivation efficiency.

$$E = hv \tag{2.1}$$

In the equation, E is photon energy, h is known as Planck constant, and v is frequency. The shorter the wavelength is, the higher the frequency.

At present, a large number of UVC virus inactivation systems apply low or medium-pressure mercury lamps as their light source. Mercury lamps have many drawbacks, such as short lifetime, toxicity, and very low efficiency[35]. As an alternative, UVC LED becomes a better choice. Because UVC LEDs have a smaller size and higher energy efficiency. Moreover, UVC LED uses toxic-free material that will not harm the environment[36]. The virus inactivation efficiency of UVC LED has been proven as high as a mercury lamp at certain wavelengths[37]. However, LEDs have a narrow spectrum with a half-width smaller than 10nm. Inside the dominant germicidal UVC region (250 nm to 280 nm), UVC LED has multiple center wavelengths such as 255 nm, 265 nm, 275 nm and 285 nm. The existing UVC LED virus inactivation tests are almost based on one, maximumly two wavelengths[35, 37, 38, 39]. There is currently no research including the systematic UVC LED virus inactivation efficiency test containing all UVC LED wavelengths. The main reason for this problem is that the UVC LED system can reach in the market are mainly containing only one or two wavelengths and do not have direct control of exposure time and intensity.

In this project, a UVC virus inactivation test platform will be developed. This platform can test all UVC LED wavelengths within the germicidal UVC region individually or test the combination of two or more wavelengths together. The platform has 6 groups of UVC LED install on the LED array module. Each group contains 4 individual LEDs with different wavelengths. Commercial Eppendorf 6-well cell culture plate can be aligned to the platform, each LED group matching one well in the plate. These types of cell culture plates are wildly used in all kinds of biology research, including virus study. This feature will enable this platform to become a generic research tool for all biology studies. Figure 2.1 shows the system diagram of the UVC Virus Inactivation system.

2.1.2 Objective

These 24 LEDs are controlled by a smart driver module, which can adjust each LED's exposure time and power separately. The driver module is the core part of the whole system by processing all the user input information and give real-time control of all LEDs. In addition, the control module is designed to be compatible with all kinds of UVC LEDs by jumper selection. As a result, the LED array module can be fully customized according to the user application. This is the main novelty of this UVC virus inactivation test platform. Moreover, this platform is aiming to be

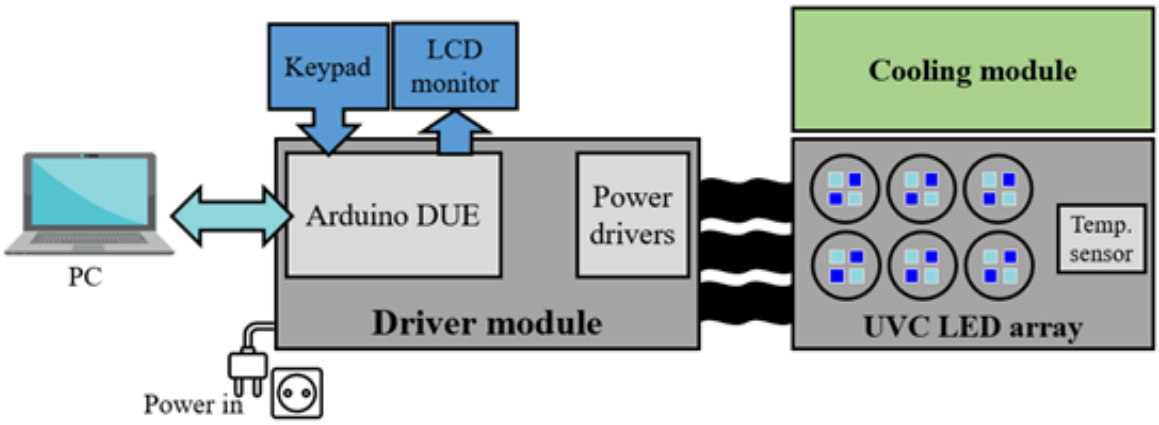

Figure 2.1: System diagram of UVC Virus Inactivation system

operated by nonelectrical background personnel. The control module user interface (UI) design is also important as another novelty. Figure 2.2 shows the final demo image.

2.1.3 Requirements

This part will show a detailed method to design a suitable control module for the UVC virus inactivation platform. The driver module should meet the following requirements:

Safe and reliable

UVC light is dangerous for human eyes and skin, so the driver module should ensure the UVC LEDs are in the right state. A hardware kill switch should be designed to turn off the UVC LED at any time. This is also important for the virus inactivation experiment that the virus is not exposed to unintended UVC light.

Precise

The UVC turned on time and power should be controlled precisely. In the virus inactivation test, UVC dose is the most important input variable which requires precise control. This is controlled by illumination time and UVC power. According to the system design requirements, the LED time control accuracy should be 1ms, and power accuracy should be 100 steps.

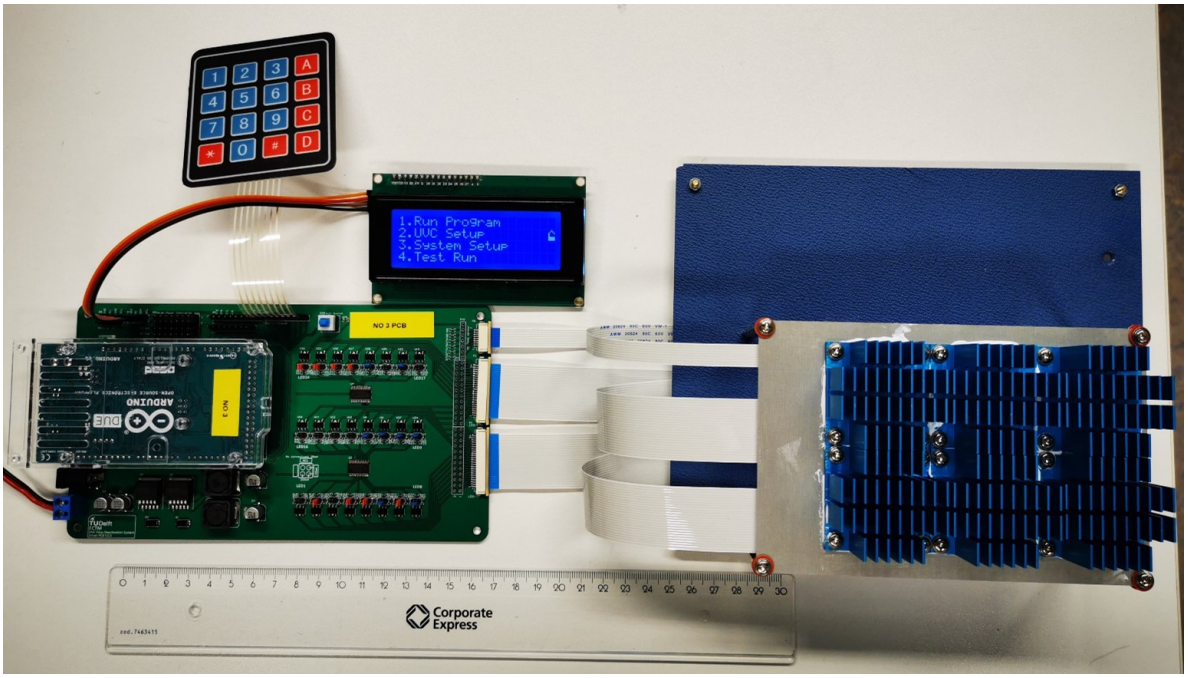

Figure 2.2: The real system overview image. Driver module is the left part with input keypad and output screen. The UVC LED array (right part) is connected to the driver module via FFC cables

User-friendly and flexible

This virus inactivation system is designed for non-electronic background users. So, it should be equipped with UI that requires no programming. Different commercial UVC LEDs have different electrical parameters. Most common UVC LEDs have the following operation currents: 30mA, 150mA, and 200mA. As a result, the driver module should have a flexible output ability that can match different kinds of UVC LEDs, including but not limited to currents listed above.

2.2 MATERIALS AND METHODS

2.2.1 Hardware design process

The whole driver module is designed on a stackable PCB. The module has 5 sub-sections that respond to different tasks. The base PCB rendering image is shown in Figure 2.3. The sub-sections are marked in red boxes. Section 1, 3-5 is located on the base PCB.

The function of each sub-section is listed in Table 2.1.

Upper layer of the driver module is MCU. Arduino DUE is used in this system. The connection socket on the base PCB is also compatible with Arduino mega 2560. All

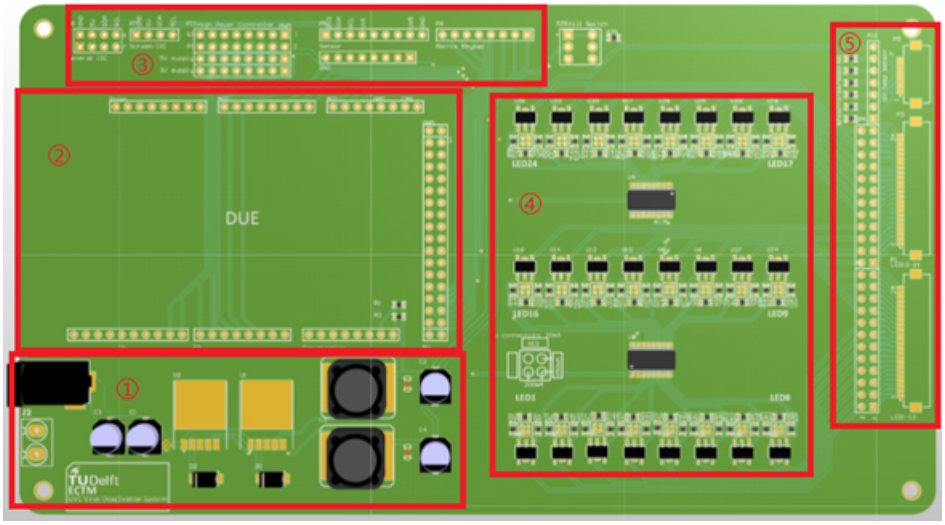

Figure 2.3: Driver module base PCB, with different sub-sections marked

Sub-section number	Function
1	Power supply
2	MCU
3	Communication ports
4	UVC LED controllers
5	Output ports

Table 2.1: Function table of driver module base PCB sub-sections

five sub-sections will be introduced in detail.

Power supply

To power all the sub-sections on the driver module, a suitable power supply is required. And different chips installed need different power supplies. So on the power supply section, 2 different output voltage is designed, which is 5V and 3.3V.

Figure 2.4 shows the power supply on the assembled base PCB, two LM2596 step-down power regulators with different output voltage chip is used here, which can drive a 3-A load with excellent line and load regulation. The input voltage can vary from 9 V to 12 V. In this case, an adapter higher than 30 A is recommended to power the driver module and UVC LED array.

MCU

The MCU is the upper layer of the driver module, which stack over the MCU sub-section on the base PCB. Shown in the Figure 2.5 bottom part. Arduino DUE (Figure 2.5 top) is a powerful MCU. It is based on an ARM 32-bit microcontroller with

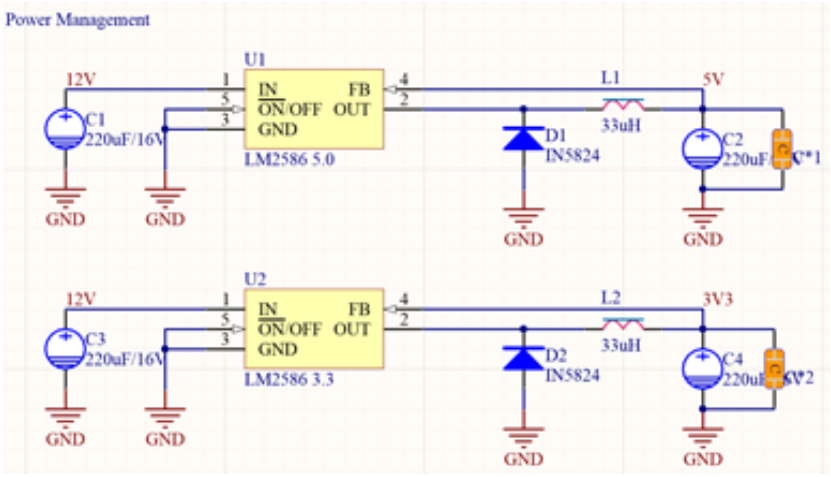

(a)

(b)

Figure 2.4: (a)The schematic of power supply design. (b)Power supply sub-section PCB image. The red arrow at the left side is the main power input port support 9-12V

an 84 MHz clock speed. Different from using a single microcontroller chip, Arduino developing board is fully equipped with all kinds of circuit protection that can make sure the microcontroller works properly. With this stackable strategy, the MCU can be isolated from the base PCB. As a result, the possible jitter caused by the switching of high power UVC LED will not affect the MCU operation.

This stackable PCB design also makes offline programming possible. Multiple MCUs can be programmed in advance and installed onto the base PCB when needed. In case anything goes wrong with the MCU, reinstall a new one can bring the system back to work again. The MCU socket on the base PCB is also compatible with Arduino MEGA 2560, a low-end, low-price MCU that can be used when the control logic is simple. This feature can make the system fulfill different applications easily.

Communication ports

The driver module can connect various peripheral devices such as keypad, liquid crystal screen, cooling fan, external sensors, etc. So, a dedicated communication

(a)

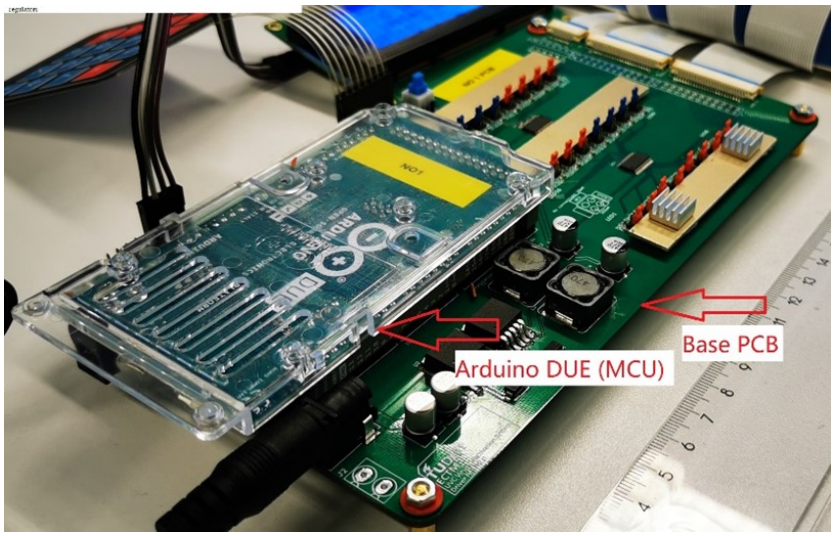

(b)

Figure 2.5: (a)A standard Arduino DUE. (b)Arduino DUE (MCU) stack over the base PCB

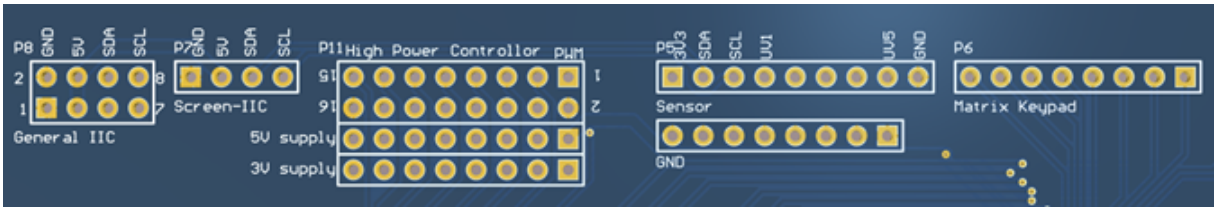

Figure 2.6: Communication port sub-section pin layout. The function of each pin group is marked beside the pins.

Port name	Port type	Compatible devices
General IIC	IIC*	General devices using IIC protocol
Screen IIC	IIC	Liquid crystal screen using IIC protocol
High power controller	PWM	High power device using PWM control signal
Sensor	IIC+ADC**	Sensors using IIC protocol and analog readout
Matrix keypad	IO***	Accept 4x4 matrix scanning keypad

*IIC is the abbreviation of Inter-integrated circuit communication protocol
**The resolution of ADC is 12 bit
***Do not connect other devices to this port except 4x4 matrix keypad

Table 2.2: Communication port function table

port sub-section is designed to connect all these external devices. The layout of the communication ports is shown in Figure 2.6.
The compatible external devices for each port are listed in Table 2.2.
All communication ports are connected to the MCU via the MCU socket. The MCU will process all the input and output signals.

LED controllers

To control all 24 UVC LEDs according to the program stored in the MCU, LED constant current controllers are required. The circuit schematic for a constant current source (CCS) is shown atFigure 2.7 top.

All LED devices, including UVC LEDs, are current-driven devices. It means the standard electrical operation point of a LED is a certain current value rather than voltage. So, it requires current feedback to make sure the current flow through the LED is correct. From the internal control logic diagram Figure 2.7 bottom, the LED cathode's current flow will go through an internal NMOS and some external feedback resistors. The internal reference voltage is 0.2 V. So, the output current can be calculated using the following Equation 2.2

$$I_{out} = \frac{V_{REF}}{R_{FB}} \tag{2.2}$$

Using the equation, the feedback resistor for the required current can be easily calculated, see Table 2.3. However, the UVC LED layout can be different between each

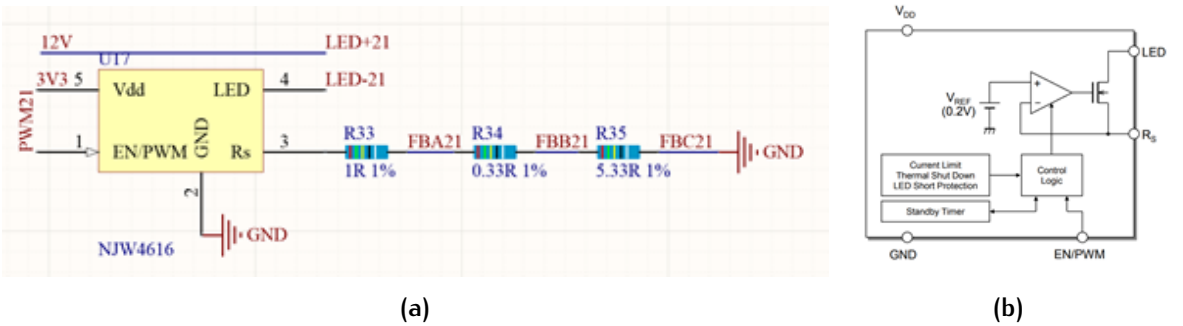

(a) (b)

Figure 2.7: (a)Schematic of the constant current driver of each LED. The LED is connected between LED+ and LED- port. (b)Internal control logic of the constant current source.

Required current	200 mA	150 mA	30 mA
Feedback resistor	1 Ω	1.33 Ω	6.66 Ω
Jumper selection	AB	BC	None

Table 2.3: Required feedback resistor for certain current

UVC LED array. As a result, every current source should be able to fit all the current mentioned in Table 2.3. Then a jumper is designed to select the required current. The jumper position is marked in Figure 2.7 top, FBA, FBB, and FBC. By connecting different jumpers, different feedback resistance can be selected and get the required current. The jumper connection point for each current is listed in Table 2.3.

Apart from the constant current source, 24 individual control signals are also needed to control every CCS at pin 1. (See Figure 2.7 EN/PWM pin). Then, two PCA9685 chips are used. PCA9685 is a 16 channel PWM generator produced by NXP using the IIC communication protocol. It can produce 16 individual PWM signals at duty cycles from 0 to 100% with 12-bit high resolution (4096 steps). This high resolution can make sure the UVC light power is accurate. Figure 2.8 Shows part of the components layout on base PCB. It includes one PCA9685 and 16 CCS controlled by it.

Since UVC LED requires a higher voltage, normally around 5V, to reach desired operation current than normal visible light LED. Because there is a 0.8 V internal voltage drop on the CCS and feedback resistors, the 5 V power supply can't drive UVC LED. The anode of the UVC LED is directly connected to input power (9 V to 12 V). By doing this, assuming using a 9 V supply, the real voltage drop on the CCS will be around 4 V, and the current that goes through CCS is the same as that go through UVC LED. Thus according to current heating theory, there will be a large amount of heat dissipate on the CCS. So, appropriate heat sinks should be installed on the CCS to avoid overheat and unstable.

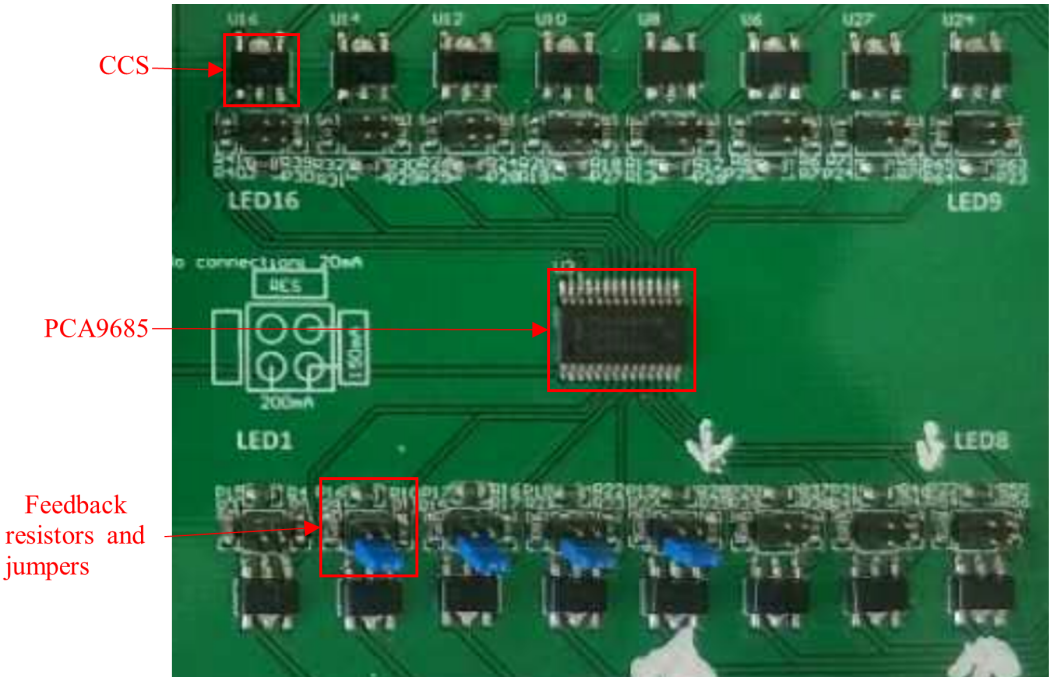

Figure 2.8: Components layout on base BCP, names for each part is marked on the left side

Output ports

Each LED needs 2 wires, cathode, and anode, to power up. Also, there are a total of 6 temperature sensors installed in each group of UVC LED. So, at least 55 wires are required to connect UVC LED array to the driver module. If using normal cables, 55 cables will occupy a lot of space and make the system bulky to use. In this circumstance, Flat flex cable (FFC) is adopted, shown in Figure 2.9 left. FFC is a kind of flat cable that can custom the core numbers, pitch, and core width. Unlike normal wires, FFC can move, bend and twist million times without damage. Moreover, it can save 70% more space than using normal wires[40]. In this case, 3 FFC cables are used. Two of them are 22 cores FFC, which is used to power UVC LED, another one is 8 cores FFC to connect temperature sensors. The socket layout is shown in Figure 2.9 right. The FFC core pitch is 1 mm.

2.2.2 Final assembling

The reflow technic is used for the final assembling. The reflow profile is shown in Figure 2.10.

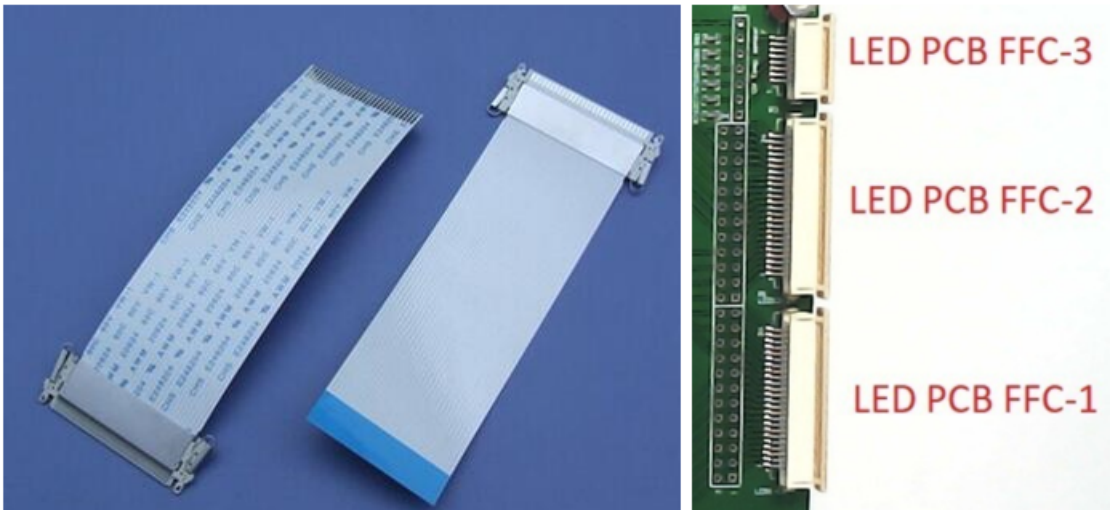

Figure 2.9: Left: FFC cables. Right: FFC output port on base PCB

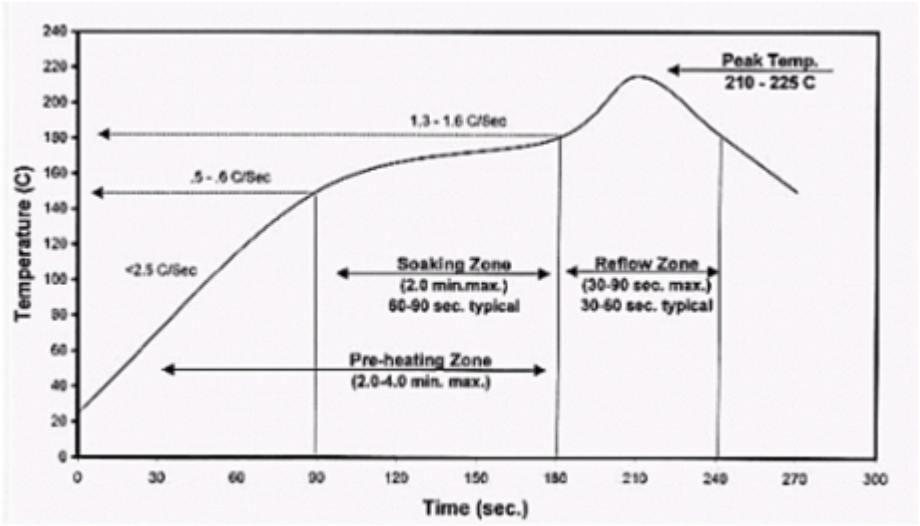

Figure 2.10: The reflow technic is used for the final assembling

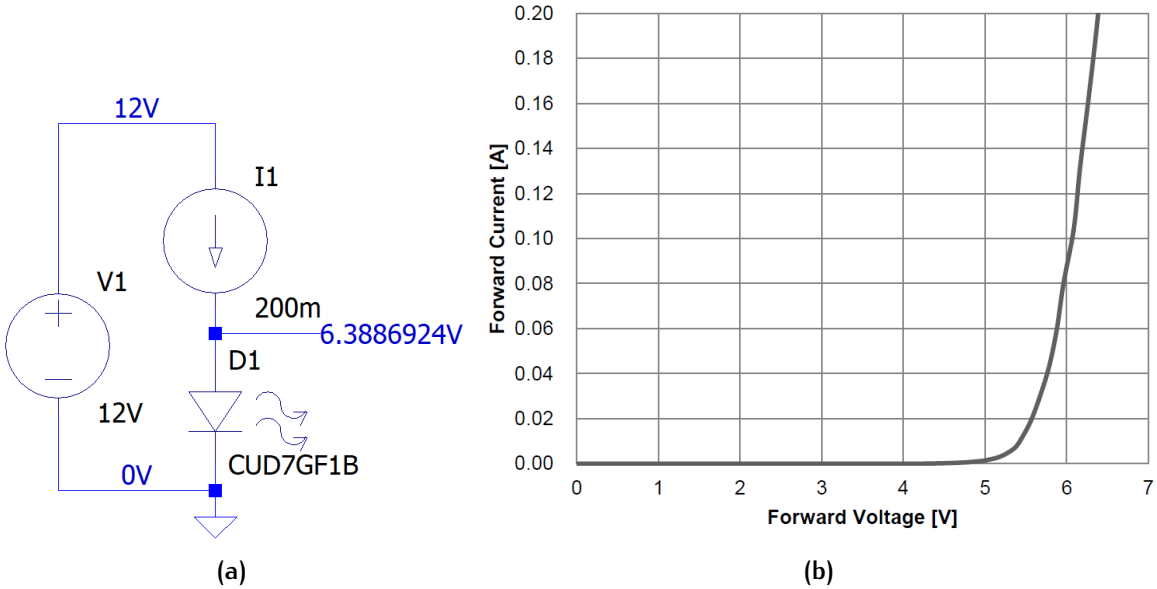

Figure 2.11: (a)Spice OP simulation result showing the UVC LED operation voltage. (b)Forward Current vs. Forward Voltage from datasheet.

2.2.3 CCS thermal simulation

The acceptable power input voltage of the system is from 9 V to 12 V. However, according to the UVC LED datasheet IV curve and OP simulation using the LED model in Figure 2.11, the LED's operation voltage at 200 mA current is 6.4 V when the supply voltage is 12 V. That means the constant current source will take the rest of the voltage and dissipate it in the form of heat. The power of heat dissipation on CSS is equivalent to its electrical power, which can be calculated with Equation 2.3.

$$P = UI \tag{2.3}$$

In the equation, P is the heat dissipated on the CCS, U is the voltage added on the CCS, and I is the current go through. The maximum dissipation power is 1.12 W using 12 V input. Refereeing to datasheet of the CCS, the maximum junction temperature it can tolerate is 150 °C. The junction temperature of CCS will become critical in these circumstances[41]. An over-high junction temperature will cause irreversible damage to the chip. Suitable cooling methods need to be adopted. A thermal simulation will be performed to look for a suitable cooling solution and ensure the junction temperature not exceeding the tolerance value.

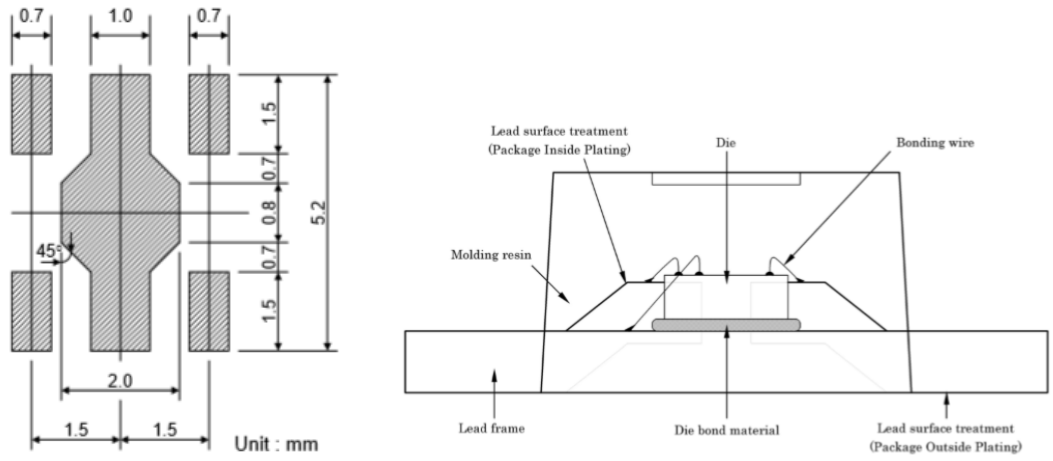

(a) (b)

Figure 2.12: (a)Footprint of SOT-89-5 package, the middle foot is the Vdd pin as well as the thermal pad. (b)Internal structure of a SOT chip.

CCS without heat sink

The heat transfer in the solids model Equation 2.4is applied in this situation to simulate the junction temperature.

$$\begin{aligned} \rho C_p u \cdot \nabla T + \nabla \cdot q &= Q + Q_{ted} \\ q &= -k \nabla T \end{aligned} \tag{2.4}$$

In the equation, ρ is density, C_p is heat capacity, and k is the thermal conductivity of the matter.

The package of CCS is SOT-89-5, whose footprint is shown in Figure 2.12a. There are 5 pins as different functions. The middle one is the Vdd pin and serves as the thermal pad. The CCS die is bond to this pad internally shown in Figure 2.12b. So, the interconnect wire on PCB will also serve as a backside heat sink.In the simulation, one classic SOT-89-5 chip model is created using COMSOL 5.4 shown in Figure 2.13a. This chip is surface mounted on an SMD pad to a PCB. Wires connections are connected to the middle thermal pad. Figure 2.13b is a cutaway diagram of this model. Inside the molding resin, the chip die is bound to the lead frame. The materials properties for a different part in the model used in the simulation are listed in Table 2.4.

The simulation's conditions are as following: Initial condition: All parts at temperature 21 °C; Boundary condition: Convective heat flux exists at all boundaries shown in Equation 2.5.

$$q_0 = h \cdot (T_{ext} - T) \tag{2.5}$$

In the equation, the external room temperature is set to 21°C, the heat transfer coefficient is set to 50 $W/(m^2 \cdot K)$; The die inside molding resin is set as a heat source,

Part name	Material	Thermal conductivity $W/(m \cdot K)$	Heat capacity $J/(kg \cdot K)$	Density kg/m^3
Foot pin Lead frame	Copper	400	385	8960
PCB wire	Copper	400	385	8960
PCB	FR4	0.3	1369	1900
Molding resin	Plastic	0.2	900	2700
Die	Silicon	130	700	2329
Heat sink	Aluminum	130	700	2329

Table 2.4: Materials properties for structures used in COMSOL model

the dissipation power is 1.2W constant.

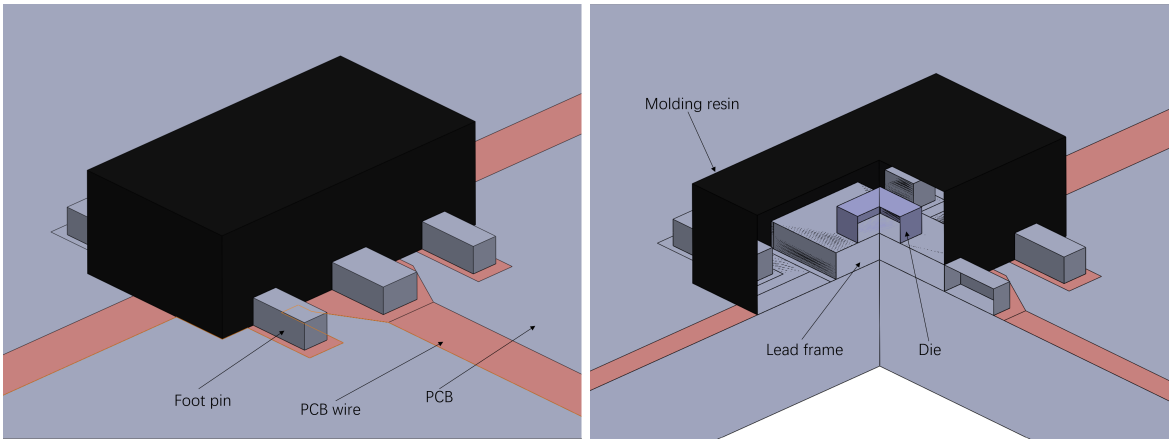

(a) (b)

Figure 2.13: (a)COMSOL modle of simulated SOT chip, (b)Cutaway diagram of the SOT chip

Run the simulation and get the result shown in Figure 2.14. The junction temperature is 133°C, which is slightly below the maximum temperature. More margin should be reserved. Also, it can be observed in the result, a part of the heat is dissipated through the thermal pad and PCB wire, and the other is accumulated in the molding resin. Thus, install a heat sink on the upper surface of the chip can improve the cooling effect.

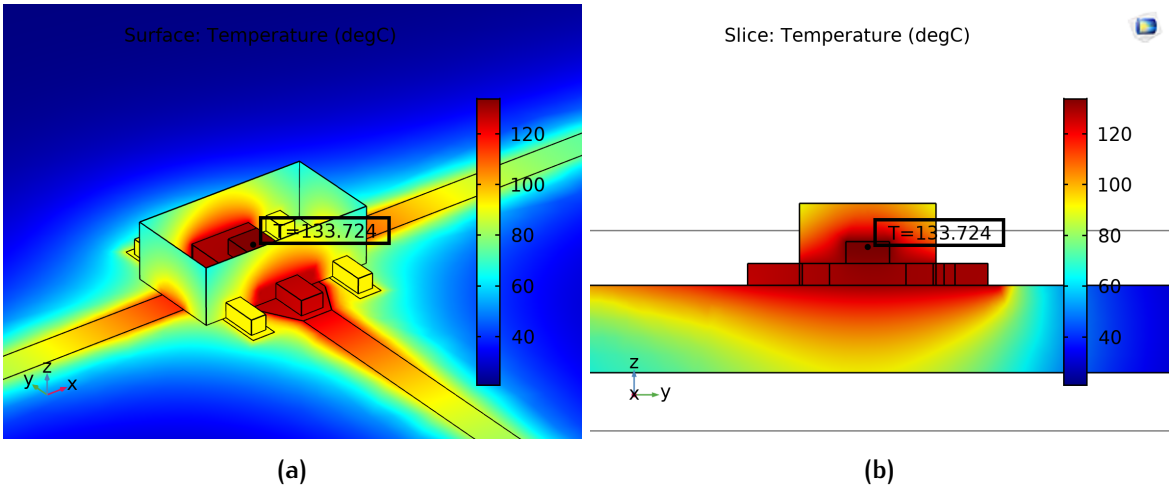

Figure 2.14: COMSOL thermal simulation result of SOT-89-5 package without a heat sink operating at 1.2 W power.

CCS with heat sink

Based on the previous simulation, keep the simulation condition and model unchanged, add a heat sink on top of the package. The material of the heat sink is also aluminum, the most common material for a heat sink.

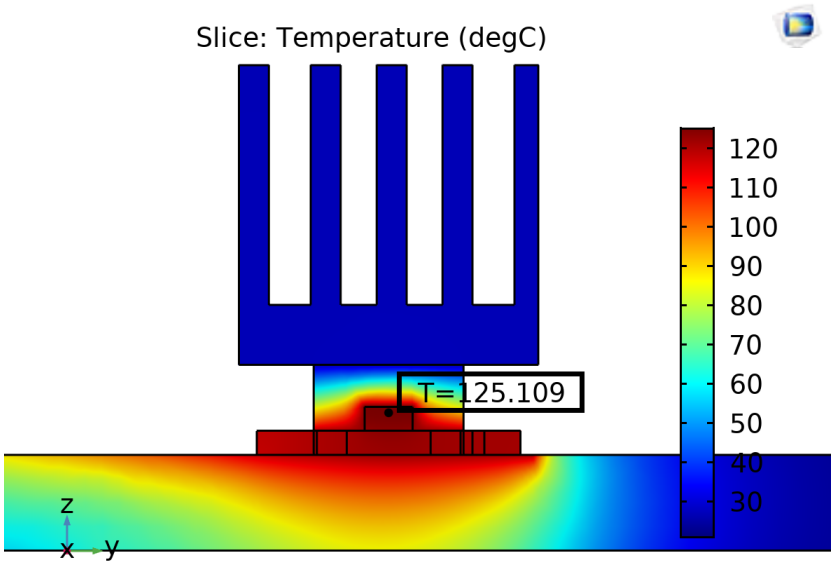

Figure 2.15: COMSOL thermal simulation result of SOT-89-5 package with a heat sink operating at 1.2 W power

The simulation result is shown in Figure 2.15. After adding the heat sink, junction temperature becomes 125 °C, almost 10 degrees lower than no heat sink added. The heat accumulated in molding resin dissipated through heat sink.

Figure 2.16: Left: Startup screen; Right: Main menu, the lock sign at right of the screen means the kill switch is open, LEDs will not glow

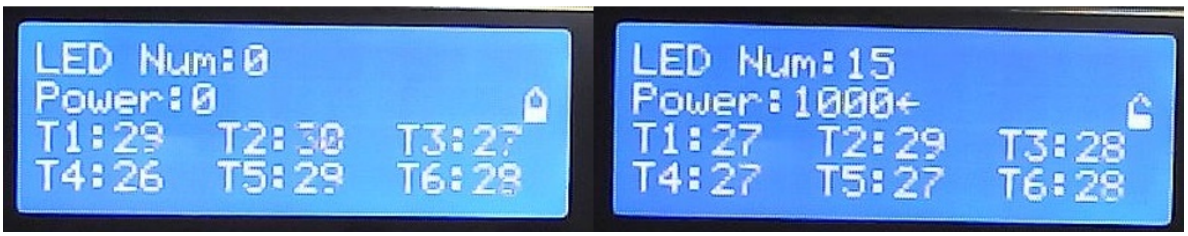

Figure 2.17: Left: Test run screen, press B can make the cursor show; Right: Set LED 15 to 1000/4096 full power

Result

In conclusion, to cooling the chip, using wider PCB wires and adding heat sinks are both useful. In this application, these two methods are all needed to keep the junction temperature of CCS as low as possible.

2.2.4 Software design and test

Test run

When the power supply is connected, the system will start up automatically. The screen will show the startup screen as Figure 2.16 left. After 2 seconds, then the main menu will show up in Figure 2.16 right. Use key 1-4 to choose functions. Here, choose function 4 (Test run) by pressing key 4. The screen will show Figure 2.17 left. Press A or B key can choose the cursor. You can change the LED number and power by type in the numbers using the number keys, press * key to delete the last digit. LED numbers can be 1-24, and power can be 0-4096. For example, Figure 2.17 right means setting LED 15 to 1000/4096 of full power. Power=0 means turn off the LED, and power = 4096 is fully on. The number between them means dimming the light. LED num = 0 means to change all the LEDs together. T1 T6 means the temperature of each LED group.

When the test profile is set, press C to run the test, the corresponding LED will be turned on according to the set power.
Do not look directly at the LED array when it is turned on. Most output is not in the visible wavelength region, so that no significant visible light will be seen,

Figure 2.18: Left screen is experiment setup; Right screen is setting LED1 to be 50% power and 1 minute time

except slight blue or white light. The UVC LED operation visible light image during operation is in appendix A.

The LEDs will keep turned on until pressing D to back to the main menu.

Experimental profile setup

The system can automatically control the LED array with pre-set duration and output power.

In the main menu, press 2 to enter LED program mode, shown in Figure 2.18 left. Press A and B to move the cursor pointing to the timing unit to adjust. Type in the number by pressing number keys and use * to delete the last digit. Use C to save the current test profile. All 24 LED profiles must be set and save before run. For example, LED 1 at 50% of full power and turn on for 1 min (Figure 2.18 right) and press C. After all LEDs are set, press D to exit to the main menu.

Run program

In the main menu, press 1 and enter Program running mode shown in Figure 2.19 left. All parameters, including power and remaining time, are shown. Press C to change viewing groups. The group number is shown at the upper right.

Press A to start the program, the clock at the top of the screen shows the total running time, and the remaining time below LED number will be counting down, shown in Figure 2.19 right. Press A again to pause the program. The counting down will stop, and LEDs will turn off. Press B to reset the experiment to the beginning state.

Press D to exit to the main menu. Don't forget to press down the kill switch.

Figure 2.19: Left screen is entering experiment running mode; Right screen is starting the experiment for 17 seconds.

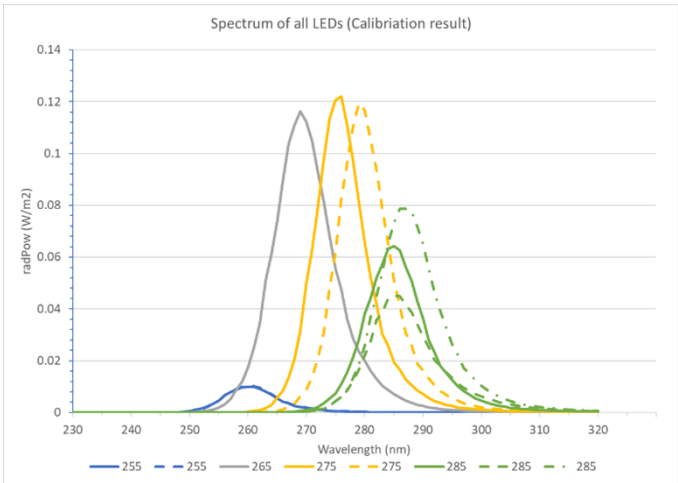

Figure 2.20: Spectrum of all 8 tested LED

2.3 MEASUREMENT

Totally 2 individual UVC virus inactivation test platforms are assembled at last. They were sent to Signify to perform a test. Totally 8 individual UVC LEDs have been tested. The test result will be shown in this part, and analysis will also be made.

2.3.1 UVC LED spectrum and radiant power measurement

Spectrum

After measurement from Signify, the measured spectrum of all 8 LEDs is obtained in Figure 2.20. The Y-axis is radiant power, and all the data is shown was tested when LED is on maximum power.

Radiant power & peak wavelength

Different operation current will affect the emitted wavelength of UVC LED, and the output light radiant power will not be linear with the input electrical power. This test is to measure the wavelength shift and radiant power under different power

output.

The integrated radiant power will give the information of the total optical power output of the LED. The efficiency has a direct relationship with peak wavelength. The radiant power and peak wavelength of all conditions are listed in Table 2.5:

Array Num LED Num*	Wavelength (nm)	Dimming	Radiant power (W/m2)	Peak wavelength (nm)	Average wavelength (nm)	Standard deviation
Arr. 1 No.1	255	1000	0.0313	260.3878	260.3388	0.043025
		2000	0.0614	260.3075		
		3000	0.0910	260.3617		
		4096	0.1230	260.2982		
Arr. 1 No.5	265	1000	0.3957	268.8805	269.0218	0.119938
		2000	0.7715	268.9716		
		3000	1.1247	269.0832		
		4096	1.4851	269.1518		
Arr. 1 No.10	285	1000	0.2327	284.3876	284.717	0.364308
		2000	0.4449	284.4226		
		3000	0.6349	284.9643		
		4096	0.8314	285.0936		
Arr. 2 No.1	255	1000	0.0298	259.8637	260.1441	0.189323
		2000	0.0590	260.2075		
		3000	0.0879	260.2267		
		4096	0.1190	260.2785		
Arr. 2 No.2	278	1000	0.3433	279.0116	279.1403	0.140603
		2000	0.6787	279.0797		
		3000	0.9980	279.1322		
		4096	1.3330	279.3378		
Arr. 2 No.5	278	1000	0.3431	275.0874	275.1643	0.097371
		2000	0.6783	275.2739		
		3000	1.0053	275.0773		
		4096	1.3565	275.2186		
Arr. 2 No.6	285	1000	0.2795	286.2777	286.4168	0.112517
		2000	0.5488	286.3887		
		3000	0.8059	286.4563		
		4096	1.0763	286.5444		
Arr. 2 No.9	285	1000	0.1676	285.0785	285.2055	0.087233
		2000	0.3288	285.2398		
		3000	0.4778	285.2268		
		4096	0.6394	285.2767		

*The configuration of the driver current and LED wavelength is attached in appendix A.

Table 2.5: Radiant power and peak wavelength by change the input power

2.3.2 Result analysis

Peak wavelength stability

For each LED, the peak wavelength must be stable during operation.

Temperature change and current change should not affect the emitted wavelength. Calculate the standard deviation of these LEDs, which is listed in the table above. It is easy to find that the standard deviations of all the LEDs are relatively small see Figure 2.21a. The highest number is from one of 285 nm LED, where the worst deviation is 0.27 nm. All the LEDs show good stability under input current variation.

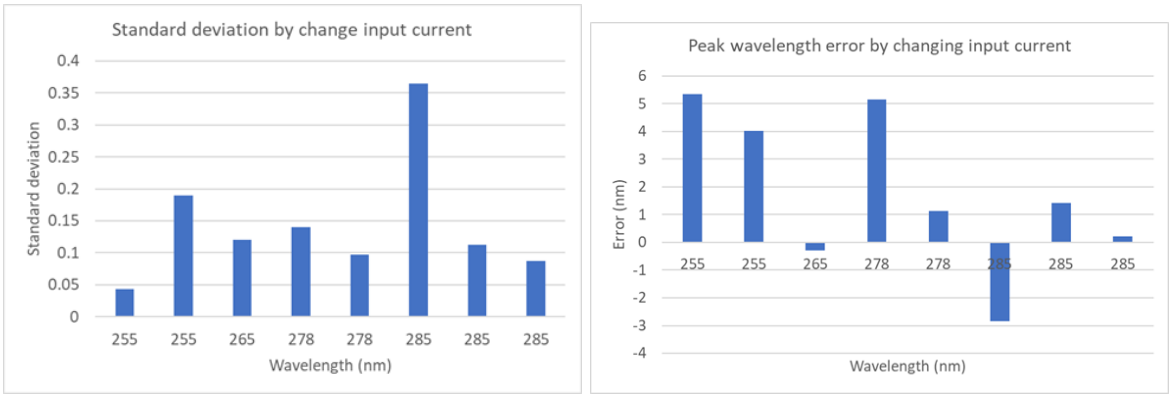

(a) (b)

Figure 2.21: (a)Standard deviation. (b)Peak wavelength error of all tested LEDs.

Peak wavelength error

Peak wavelength is one of the key variables that will affect virus inactivation efficiency. The error of the peak wavelength is calculated in Figure 2.21b.

According to the data from Figure 2.21a, the error of 255 nm LED is highest, about 5nm longer than the data from the datasheet. Moreover, many LEDs have a positive error compared to datasheets, meaning the actual wavelength is longer than the rated. All the errors are controlled below 2%, which meets the requirements.

Linearity

To control the output light power, the optical output should be linear according to the input current. Plot the radiance according to the input current (Fig2.21b) can measure the linearity.

According to Figure 2.22, all the tested LED has good linearity. The radiant power is not the same for the same type of LED. Because during the testing, the LED aligned to the detector manually, slightly tilting or moving can cause tested radiant power lost due to uniform distribution of LED waveform.

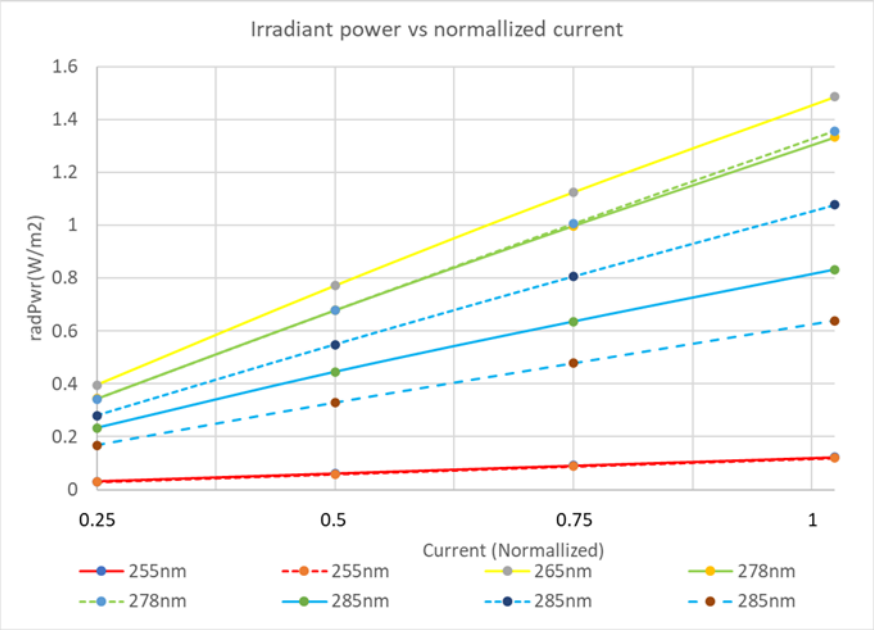

Figure 2.22: Radiant power according to input power change

2.4 RESULT

After finishing measurement at Signify, *UVC virus inactivation test platform* was sent to *Erasmus MC* to perform the virus inactivation test shown in Figure 2.23. The UVC LED array was placed inside the fume hood to run the inactivation test, connecting to the control module outside the fume hood. The inactivation protocol and system status can be set and monitored via the keypad and LCD screen.

The targeted testing virus is *Influenza*. According to DOE, the different combination of wavelengths and doses was chosen to test the virus inactivation efficiency. Figure 2.24a is the inactivation result. The solution in the small wells can test the existence of the active virus. Active virus concentration below a certain threshold value can be considered as not existing. Figure 2.24b shows the indication of the active virus, red dot meaning virus is inactivated. Meanwhile, no dot means the virus is still active. Each row in Figure 2.24a means one virus test. The lower well is 10 times diluted of the upper well. Using this method, the concentration of active virus can be determined. From left to right in the virus test well plate, the same inactivation wavelength combination is used with UV dose from low to high. It is obvious to see that the virus inactivation efficiency is rising along with the dose.

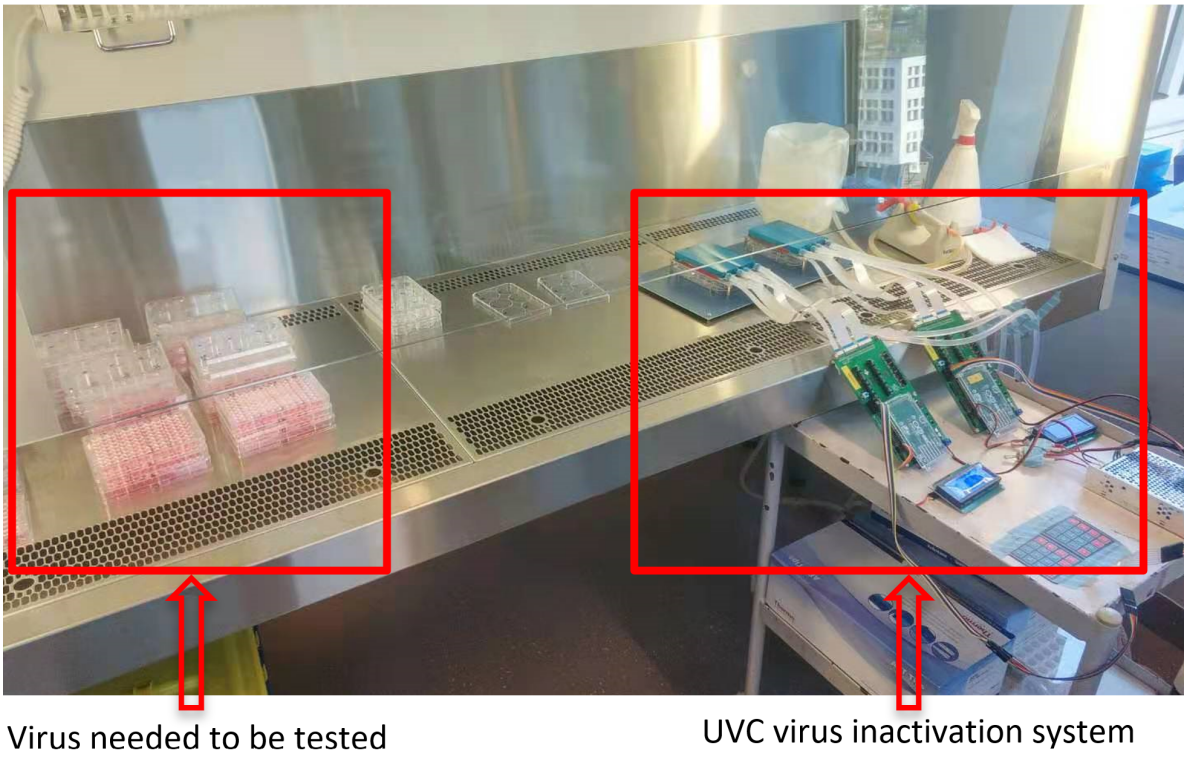

Figure 2.23: Virus inactivation test experiment setup.

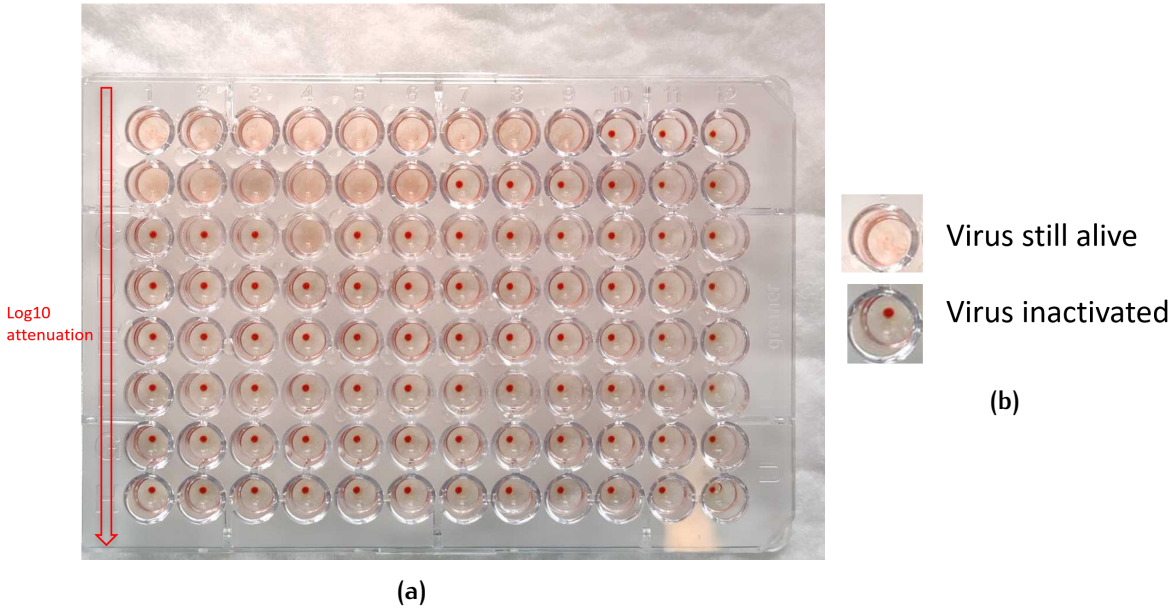

Figure 2.24: (a)Virus inactivation test result. (b)Legend of wells.

2.5 CONCLUSION

After design and measurement, the *UVC virus inactivation test platform* was successfully finished virus activation test in a real application. This platform currently

becomes a genetic research tool for another project related to virus inactivation mechanism research. The design of the driver module of this platform fulfilled all the requirements. The design methodology of combining indication LED drivers with single high-power CCSs is proven as feasible to drive high-power LED arrays. Moreover, adding redundancy test points and communication ports is another key design rule to make sure the driver system is expandable. Regarding the connection between LED array (matrix) and driver module, FFC is a good choice comparing to conventional cables with a higher power limit and flexible size. Last but not least, a hardware switch is important for all driving systems to shut down the system in an emergency to prevent any damage when software stops.

2.5.1 Future developments

Apart from all the advantages of design methodology currently discussed, some improvements should be made in further designs.

Customized pattern

In the objective of this thesis work, customized patterns is a key feature of the advanced optoelectronic driver system. In future work, the array driver capability should upgrade to matrix control capability to display customized patterns.

Higher light intensity

Some biomedical application requires even higher light intensity. Future work should have either a higher operation current limit or denser matrix drive capability to reach this goal.

Better UI

Currently, the UI is designed together with the driver module. In the future, the driver system will become wearable or implantable. So the UI should be separated from the driver module and be easier to operate. For example, design a UI on PC and communicate wirelessly with the driver module forming a complete driver system.

3 INTERACTIVE OPTO-ELECTRONICS SYSTEM

3.1 INTRODUCTION

In this chapter, step two of researching the design methodology of advanced opto-electronics driver system for biomedical application will be introduced. *Interactive Optoelectronics System* includes a pre-designed 16 × 16 ultra-high power LED matrix, which needs to be driven. The operation current of LEDs used in the matrix is 1 A. The driver can reach a 125 Hz refresh rate and total latency less than 60 ms.

3.1.1 Background

Optogenetics theory

Optogenetics represents a biological technology that includes the use of light to control cells that have been genetically modified to express ion channels[42, 43]. Optogenetics is a cell-level modulation method that combines optoelectronics and genetics to control cells' activity in living tissue, including freely-moving animals.

Early in the 1990s, light has been discovered to activate ion flow in bacterio-rhodopsin yeast[44]. Since 2002, after the first genetically targeted method to excite rhodopsin-sensitized neurons[45], the optogenetics technique is mainly used to control neurons.

In later years, optogenetics was applied on cardiomyocytes to terminate arrhythmias, which could lead to atrial fibrillation (AF)[46]. Recent research shows that whole heart arrhythmia, including ventricular arrhythmias, can be terminated by local epicardial illumination[47]. Using a customized stimulation pattern based on arrhythmias mechanisms can lower the defibrillation illumination energy[48]. This method has the potential ability becoming an alternative to painful electric cardioversion treatment.

In this project, a genetically modified epicardial cell monolayer with the Chireff gene needs to be tested. The basic theory of this project is shown in Figure 3.1. First, prepare an epicardial cell monolayer (a). Then introduce the Chireff gene, which sensitive to blue (460 nm) light, into the cells, and the cells will express new light-sensitive ion channels (b). When exposed to blue light, the light-sensitive ion channels will open (c). Then ions can flow through the channels create a membrane

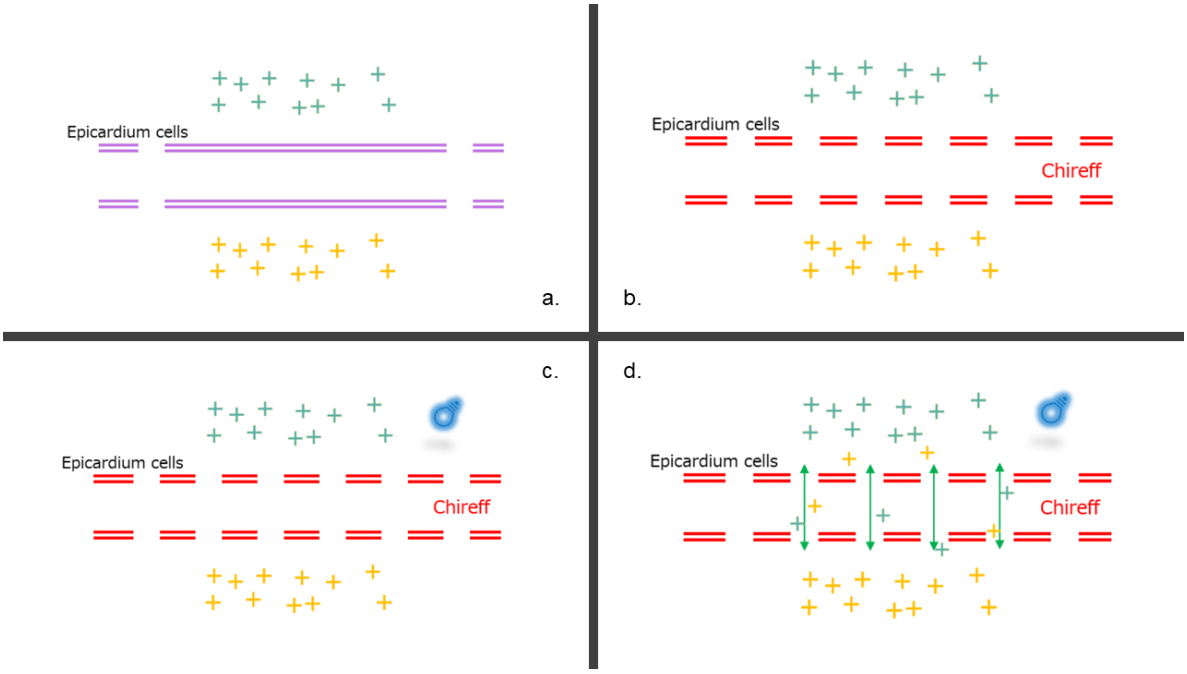

Figure 3.1: Optogenetics theory of tested epicardial cell mono layer

voltage difference that polarizes the cell and defibrillate the AF (d).

Existing result

To successfully excite the ion channels in the optogenetic modified cells, the light intensity needs to reach a certain threshold value. The illumination pattern also should update in real-time to adapt to different arrhythmias models. There are already AI algorithms that can provide optimized defibrillation patterns.

To meet the intensity and customized pattern requirements, the current experiment system uses a mono color high power DLP projector to reach the required light intensity and display patterns[48]. However, though a DLP projector can meet the requirements, it needs a high-power light source and complex optics system to realize the function. The current system's size is too large to be considered a possible solution in future in-vivo research.

High power LED matrix is one of the most feasible solutions to excited the optogenetics cell layers. However, the current commercially available LED matrix is mainly for display purposes, whose light intensity is much smaller than what is needed for exciting the cells. So, a high-power LED matrix for optogenetics application is designed using high-power mini LED. This LED matrix needs a suitable driver to operate it. Yet, there is no existing driver system that compatible with such LED matrix. Thus, an advanced LED driver system needs to be designed for

this biomedical application.

3.1.2 Objective

An advanced LED matrix driver system will be designed in this project to drive a 16×16 high power matrix. The driver system should meet the latency requirement and output requirements. A PC user interface also will be designed to process image data and user input. Suitable matrix drive topology and communication protocol need to be designed first. All the parameters should be measured before the system is applied to biomedical applications.

3.1.3 Requirements

Communication requirements

A general communication protocol should be defined to exchange the pattern data between systems, like PC controlling software, AI software, and the driver module. This protocol needs to be expandable to suit different matrix sizes.

The data format should be a $N \times M$ matrix with 8-bit (0-255 level) grayscale elements. N and M refer to the LED matrix dimension, N being the width pixel and M being the height pixel. This can be modified to match different sizes of the matrix, ensuring compatibility of the system.

Latency requirement

Input image refresh time should be shorter than 60ms. This means the maximum time from system receiving a new frame to this frame displayed on the matrix is 60 ms. The total time includes these parts:

- PC RAM access (Reading result from AI)
- PC-Driver communication
- Driver process and register configure
- LED matrix response

Moreover, the communication should have flow control to avoid package loss and incomplete data.

Output requirement

The LED array's radiant power should be higher than $30mW/cm^2$. To fulfill this requirement, high-power LEDs were adopted in this case. The matrix uses LXZ1-PB01 as single pixels. The operation current for each LED is 1A. As a result, the matrix driver should have matched output capacity to drive the matrix.

Apart from the output capacity, the driver should have output linearity better than 5% to ensure the accuracy of the experiments. Together with output stability during the experiments. Each experiment takes at least 30 min according to the biomedical protocol.

3.2 METHOD AND MATERIALS

3.2.1 Matrix driver topology discussion

To drive the high power LED matrix, a suitable driving strategy needs to be defined before starting the designing process. After searching through the literature[49], three possible solutions are being considered. In this section, these methods will be evaluated. The matrix size is assumed as $M(Column) \times N(Row)$, and the radiant power of each LED is R.

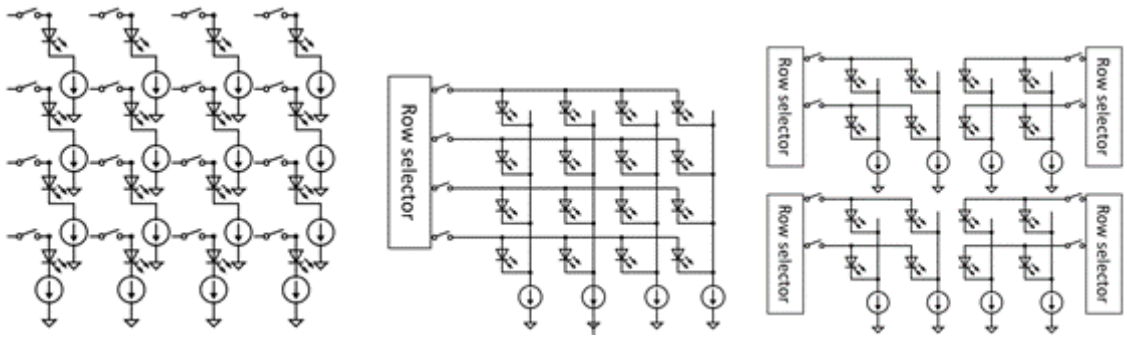

(a) Individual CCS control **(b)** Row-column scanning **(c)** Zone scanning control

Figure 3.2: LED matrix driver with different topology

Individual control

This method assigns each LED an individual CCS and a switch. The control topology is shown in Figure 3.2a. Using this topology, the number of signal wire and CCS is $M \times N$, and radiant power is $M \times N \times R$. This topology's advantage is that the refresh rate can be infinite high because no scanning is used to drive this matrix. However, it uses N times more CCSs and signal ports, which cost a lot of space and price. Moreover, it is also challenging to find such controllers with $M \times N$ GPIOs.

Row-column scanning

A scanning technology is to display a pattern in rows by switching the active row fast enough, faster than human eye visual persistence interval, then this pattern can be seen by eyes[50]. This topology in Figure 3.2b requires M CCSs and $M + N$ signal wires. Compare to individual control, the needed CCSs and GPIOs are much less. But the refresh speed is limited by the speed of the controller. The desired refresh speed is as high as possible. Moreover, because of scanning, there will be only one row of LED is turned on at each moment, cause the total radiant power to become $M \times R$, N times less than individual control topology.

Multiple zone control

To reach higher refresh speed and radiant power, separate a large matrix into zones will help. Using this topology, a row-column scan matrix is divided into $X(Column) \times Y(Row)$ zones shown in Figure 3.2c, requiring $M \times Y$ CCSs and $M \times Y + N \times X$ signal wires. The optical radiant power is $M \times R \times X$, X times higher than without zones together with X times higher refresh speed. This topology combines the advantage of individual control and row-column scanning by setting suitable zone numbers to reach a balance between performance and system complexity.

Conclusion

In Table 3.1, specifications of three control topologies are listed. In this case, to design a smart driver for 16×16 LED matrix, the simplest row-column driver topology is chosen. Because the matrix size is relatively small compared to displays with thousands of rows. Moreover, the size of CCS that can drive chosen LED is $1cm \times 1cm$. This topology can save the system size and complexity.

	Individual control	Row-column scanning	Multiple zone control
No. of CCSs	$M \times N$	M	$M \times Y$
No. of signal wires	$M \times N$	$M + N$	$M \times Y + N \times X$
Total radiant power*	$M \times N \times R$	$M \times R$	$M \times R \times X$
System complexity	High	Low	Medium

*The driver heat dissipation and electrical power are proportional to radiant power.

Table 3.1: Comparison between different driver topology

3.2.2 Communication method discussion

According to the project requirement, the latency of the system should be shorter than 60ms. Thus communication time should strictly keep below 20ms to make

sure the total latency under the limit. According to Equation 3.1, the communication speed should at least be 12.8 KB/s. Apart from the latency requirement, each experiment takes at least half an hour to finish. So, the system should be stable and keep required speed at least 30 minutes.

$$16 \times 16 \times 1Byte \times 50Hz = 12.8KB/s \tag{3.1}$$

There are many ways to transmit data from the computer to the MCU controller. A suitable communication method should be determined and adopted by this system. Table 3.2 lists major communication methods and their properties.

Medium	Name	Standard	Speed	Complexity
Wired	Serial port	RS232	Slow	Simple
	USB	2.0	Fast	Complex
Wireless	Bluetooth	4.0	Medium	Simple
	Wi-Fi	802.11b/g	Medium	Medium

Table 3.2: Qualitative, speed and complexity comparing between different communication methods.

Serial port is the most common port that transmits data between devices. The standard baud rate of the serial port is the divisor of 921600. In practical use, 115200 (921600/8) is the fastest baud rate recommended by IEEE[51]. It means there are 115200 voltage level changes in one second, as known as 115 200 bit/s . To transmit a byte data, 10 bits need to be used for 1 start bit, 8 data bits, and 1 stop bit. So the real maximum speed of the serial port is $115200/10 = 11.520KB/s$.

USB 2.0 can reach a much higher speed than the serial port, up to 20 MB/s. However, it needs complex driver both on PC and MCU, which is difficult to develop and takes a lot of time to write driver programs.

Bluetooth is a widely used wireless communication method, whose communication speed is up to 3 MB/s within 0.5m distance in the air. However, due to its low energy feature, any obstacles between receiver and transmitter will cause connection loss or unstable link[52].

Same as Bluetooth, Wi-Fi is also wireless connection using 2.4GHz baud with a higher power. 802.11b/g can have a stable link within 10m distance in the air. Moreover, Wi-Fi has local area network access [52]. Thus, all the standard communication protocols such as TCP/IP can be used to ensure communication correctness.

Serial port cannot reach the speed requirement of the system, see Equation 3.1. A wired connection like USB requires a complex driver, which difficult to develop. According to the previous discussion, Wi-Fi is chosen to be the communication

method between PC and control module because it can provide wireless connection and enough speed with a mature communication protocol.

3.2.3 System design

After confirming the driver topology and communication method, the next step is system design. Because of the existence of output capacitors and input capacitors of PWM generator output and CCS input pin, there will be charge and discharge time. This time causes a nonequal delay which will change the real output duty cycle. According to the datasheet of these two chips, the total capacitance is 15pF and the output resistor is 1KΩ. An equivalent model was built in LTSpice to simulate the charge and discharge of the capacitors, the result is shown in Figure 3.3. In this case, the PWM frequency is set to 100 kHz (10 µs per cycle) and sweep the duty cycle from 1% to 10% (0.1μs to 1μs).

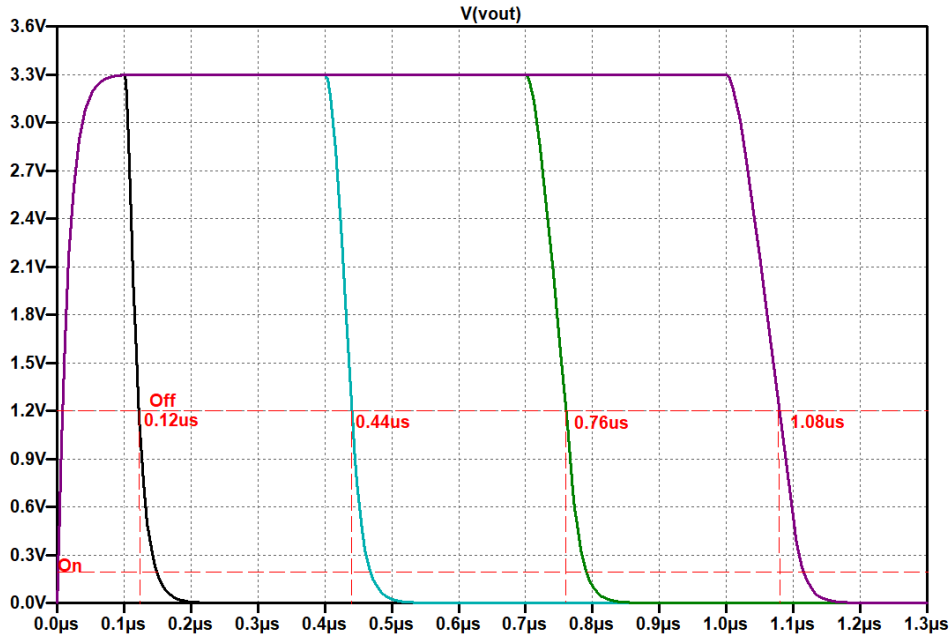

Figure 3.3: Simulation of input output capactor charge procedure in low duty cycle

From the simulation result, at duty cycle 1% (0.1 µs), the output time is 0.12 µs, cause a 20% error. When the duty cycle is 10%, the error decrease to 8%. To ensure good output linearity, especially at low PWM duty cycle, two identical CCS arrays except for the current limits are used, one having one-tenth of maximum current than another. Thus the driver has two output ranges, the LED matrix should connect to the low range when the duty cycle is below 10%. Using this method, the error at low output power will be reduced by ten times. Figure 3.4 is the system diagram, which will be introduced in detail in the next section.

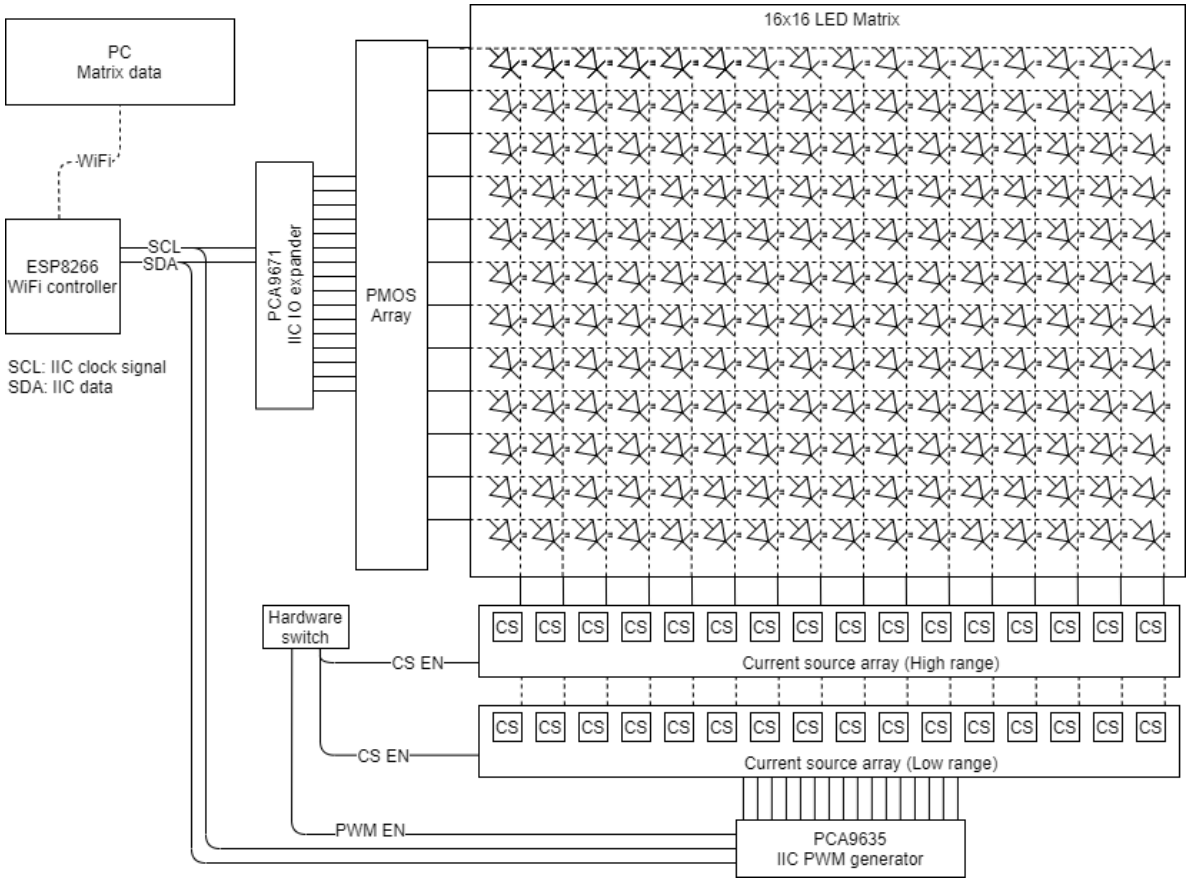

Figure 3.4: System diagram of *Interactive opto-electronics system*

3.2.4 Hardware design

In this section, design of the driver PCB will be introduced. Figure 3.5 is the 3D rendering image. Different function groups are marked on the image.

MCU

Almost all MCUs equipped with hardware IIC port can serve as the controller in this Interactive Opto-electronics system. The connection between MCU and Wi-Fi module is an essential part. Usually, a Wi-Fi module is connected to the MCU via SPI port. However, unpredicted vibration or touch will cause a connection problem of SPI, and PCB routing problem will also affect the SPI speed. As a result, the ESP8266 module shown in Figure 3.6 is chosen to be the controller in the system. ESP8266 has an internal Wi-Fi transceiver connected to MCU, which can be reached easily by API programming. Moreover, the clock speed of ESP8266 is 160MHz which is fast enough for this application. The connection method of Wi-Fi is flexible. MCU can connect directly to a PC by direct Wi-Fi link or connect to a Wi-Fi router.

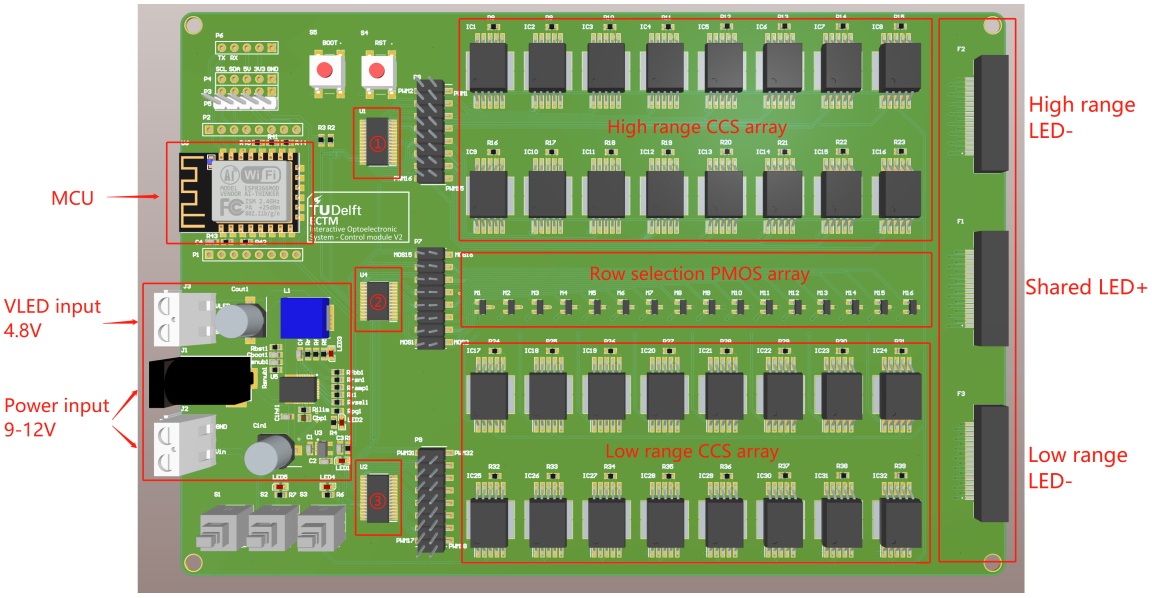

Figure 3.5: PCB 3D rendering image of *Interactive opto-electronics system*

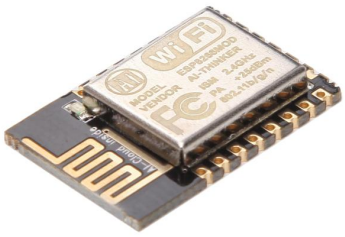

Figure 3.6: An ESP8266 micro controller

LED controller

Considering the scalability of the system, IIC based LED controllers are suitable for this system. Because with 2 wires-SDA and SCL, multiple LED drivers can be connected without any more wires. Below some possible chips are listed in Table 3.3. To reach a higher refresh rate, the higher IIC speed is better. PWM light intensity control will perform at column control (constant current dimming). Row select chip does not require the PWM function. So, *PCA9635* is chosen to be the column control chip and *PCA9671* to be the row selection chip. In Figure 3.5, chips number 1 and 3 are column control chip *PCA9635*. Chip number 2 is row selection chip *PCA9671*.

As the column control chip, *PCA9635* generates PWM signal to control the CCS array. Figure 3.7 is the footprint of this chip. A0 to A6 pin can define the chip address, thus let the system choose high or low range. LED0 to LED15 are 16 output PWM signals connected to the CCS array. OE pin connected to a hardware switch can cut off the PWM signal immediately.
Same as UVC virus inactivation test platform, a suitable CCS is also needed in this system. The CCS maximum output current should higher than 1 A with PWM in-

Model number	PCA9555	PCA9635	PCA9671	PCA9685
Manufacture	NXP	NXP	NXP	NXP
Max IIC speed	400 kHz	1 MHz	1 MHz	1 MHz
PWM steps	I/O *	256	I/O	4096
PWM frequency	0	97.6 kHz	0	24 Hz to 1526 Hz
Output channels	16	16	16	16
Available address	8	128	64	62

*This is an IO expansion chip, which doesn't have an internal clock for PWM output.

Table 3.3: Available IIC LED drivers

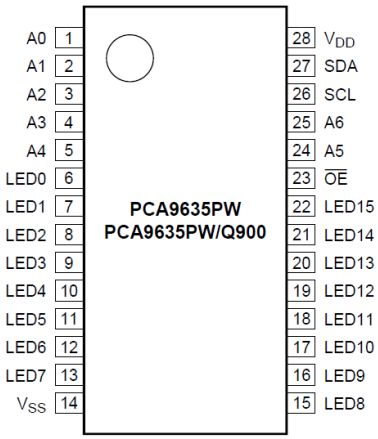

Figure 3.7: Footprint of column control chip *PCA9635*

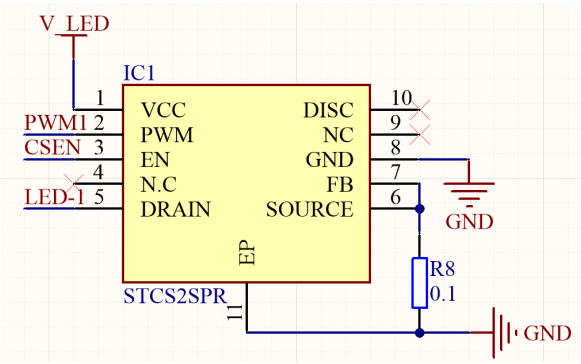

Figure 3.8: CCS connection of *Interactive opto-electronics system*

put function. *STCS2* produced by *STMicroelectronics* with up to 2 A output current is adopted.

The system has two output ranges: 0 A to 1 A and 0 mA to 100 mA. The current limit is set by external feedback resistor R_{FB}. For this current source, V_{REF} is 0.1V. Using Equation 2.2, R_{FB} can be calculated as 1Ω and 0.1Ω to reach required output currents. Connection of CCS is shown in Figure 3.8. Apart from PWM input, hardware enables *CSEN* to be controlled by a switch to ensure the current source can be disabled immediately by manual if the system is down and PWM chips have no response.

Power supply

Different from UVC LED, the operation voltage of 470 nm LED in this system is 3.2 V, lower than 5 V of UVC LED. If still powering the LED with the 9 V to 12 V input voltage, around 7 watts of heat will dissipate on the CCS, calculated with Equation 2.3. According to the thermal simulation of CCS in chapter 2, the die of CCS can't tolerate this high power and will break. As a result, a high power step-down power converter is needed to convert 9 V to 12 V input DC voltage to suitable

driving voltage.

The driving voltage should slightly higher than the maximum LED operation voltage plus CCS voltage drop. Referring to the datasheet of PB01 and CCS, the LED maximum forward voltage is 3.5 V, and CCS maximum voltage drop is 0.8 V. Thus, the driving voltage should be slightly higher than 4.3 V. In this case, 4.8 V is chosen to be the driving voltage, not heating the CCS and leave enough margin to drive LED.

There are 16 LEDs in one row with 1 A maximum current, making the total current requirement 16 A maximum. The step-down power convertor output capacity should higher than 16 A to drive the entire matrix. After searching the commercial product, there is no suitable external power supply with such output profile. *TPS543B20* manufactured by TI, which has a maximum output capacity of 24 A, is applied in the system to build up an onboard step-down converter circuit. This chip also has a power management function that enables monitoring the output voltage stability.

The input power connection terminal is shown in theFigure 3.5 power input part. There are three terminals with different functions. The top side one is directly connected to the *VLED*. If the onboard step-down power convertor breaking down, an external power supply could still maintain the system operation during the experiment. On the lower side, the other two terminals are the 9 V to 12 V power connected to onboard power convertor for different connectors. Commercial power supplies with output from 9 V to 12 V are wildly available.

Scanning controller

Scanning control part includes row selection chip and PMOS array. Figure 3.9b is the footprint of row selection chip. According to system diagram, the row selection is realized by switching on and off the LED array's anode. A simplified PMOS LED control model is shown in Figure 3.9a, the gate of each PMOS is connected to the output pin P00-P17 of row selection chip. By sending signals to turn on next PMOS in the array and turn off current one, LEDs in the matrix can be turned on row by row, thus realizing the scanning function.

Output terminal

Using the verified connection method in *UVC Virus inactivation test platform*, there are three FFC output terminals on the driver, see Figure 3.5. Each terminal containing 16 internal wires which connect the driver to LED matrix. The middle one is the shared LED positive output pin connected to the drain of row selection PMOS array. The top and bottom terminals are high and low range CCS output. During the

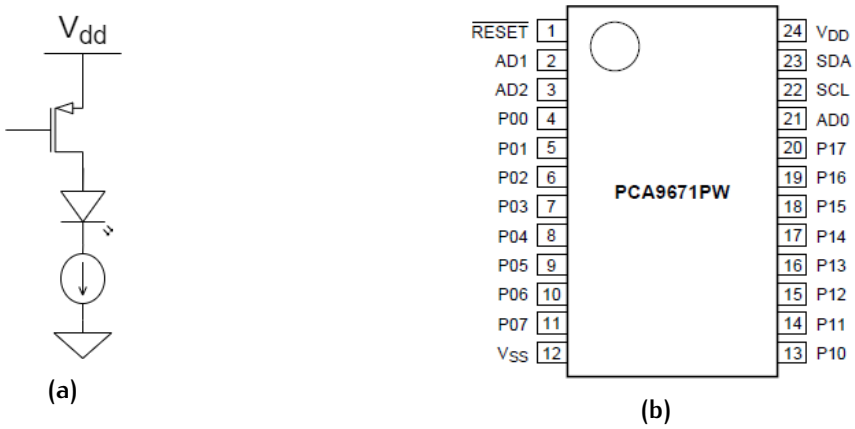

Figure 3.9: (a)PMOS LED control model. (b)Footprint of row selection chip *PCA9671*

experiments, switching the cathode wire between these two terminals can realize range switching.

Enclosure

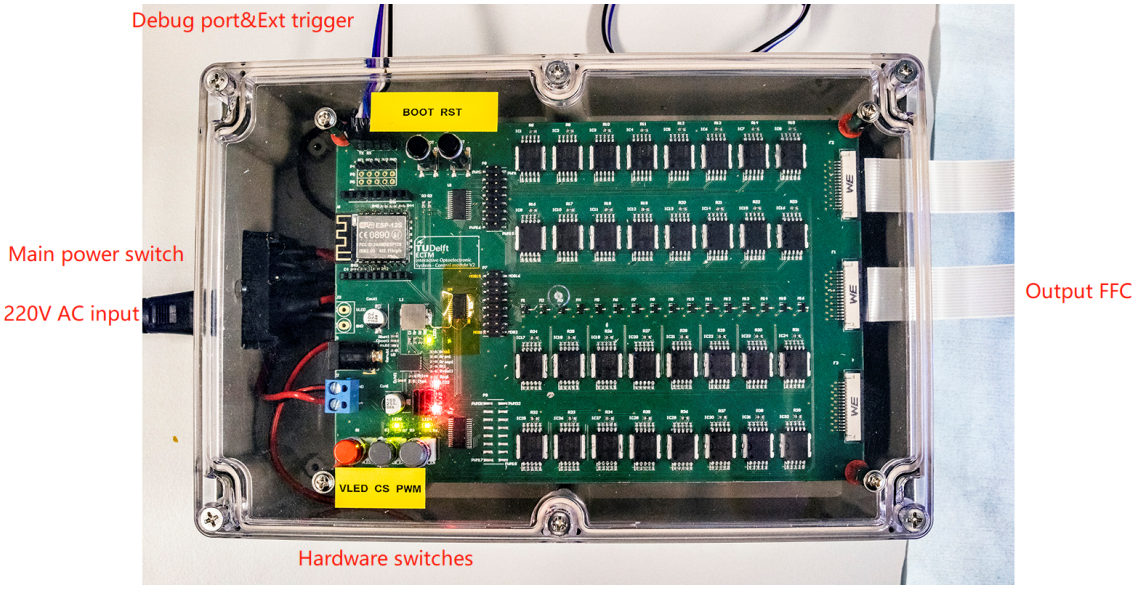

Figure 3.10: *Interactive opto-electronics system* control module

To further enhance the robustness of the system, all system parts, including driver PCB and power supply will be installed inside a suitable enclosure, becoming a *Control Module*. Only necessary connectors and switches are lead out. The functions of them are marked in Figure 3.10. On left side of the control module is the main 220 V power input together with the main switch. Debug port can reprogram and check system status through the serial port. External trigger port enables using other signal generators to control the *Interactive optoelectronic system*. Hardware

switches that control the onboard power converter, PWM generator, and CCSs are on the lid.

3.2.5 Software design

After finishing hardware design, software is another essential part consists the completed system. To operating the system, two software are required. One is the MCU software running on *ESP8266* controlling the hardware. Another one is running on the PC that processes the user input and patterns and then sends them to *Control Module*.

MCU software design

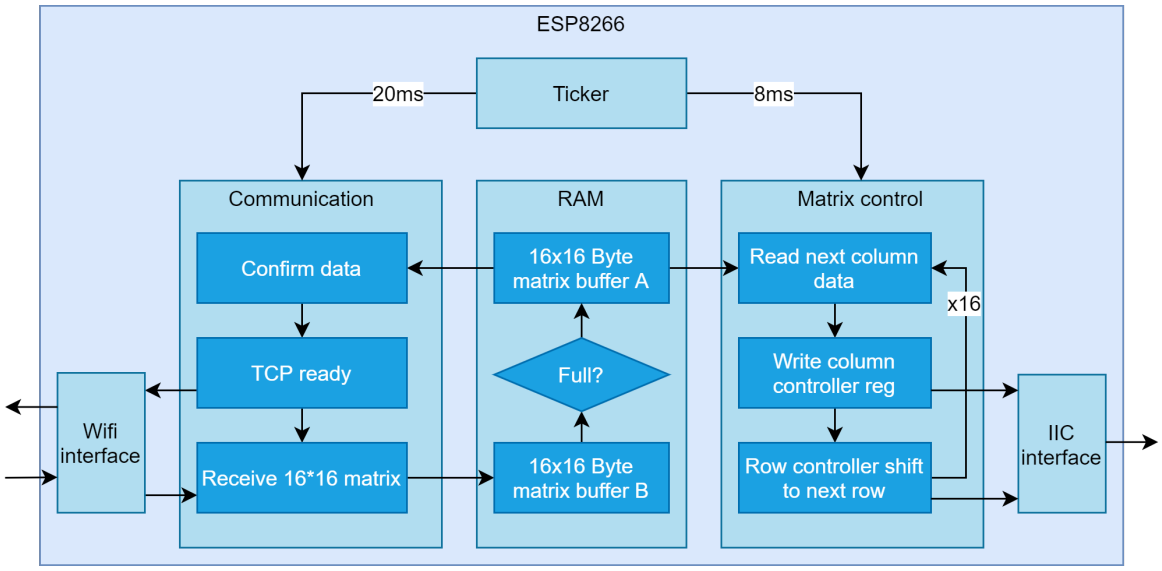

Figure 3.11: Software design diagram of MCU

Figure 3.11 is a software diagram of the software running on *ESP8266* MCU. This software is divided into three parts, which are communication, RAM control, and matrix control.

Before the software starts running, the Wi-Fi and IIC interface will be initialized. The *Control Module* will connect to the PC automatically and configure the IIC protocol.

Communication and matrix control is controlled by a precise ticker generated by system clock. Communication action is called every 50 ms to fetch new matrix data from PC software. Assuming the Wi-Fi connection at 50 KB/s speed, it takes $(16 \times 16)/50K = 5.12ms$ to transfer the matrix. 50ms interval can make sure the data is finished. Also, fulfill the latency requirement that system latency is below 60 ms with a 10ms margin. Another advantage is that lower down the frequency

of Wi-Fi communication can save the system power. During a communication call, the first thing is to confirm the last data in RAM is complete. Then send a ready signal to PC representing the system is ready for the next matrix data. When the data stream is coming, they are stored temporarily in a $16 \times 16 Byte$ buffer B in the RAM. If the buffer is full, it will be pushed to buffer A with the same size, waiting for being retrieved by matrix control program.

Matrix control is called every 8 ms to realize a 125 hertz refresh rate. When called, the column data of the next row will be read and write to column control chip via IIC port. After column data finishing writing, a signal will send to row control chip to turn on this row and turn off the last row. Repeating this action 16 times, the whole matrix is refreshed for once.

PC software design

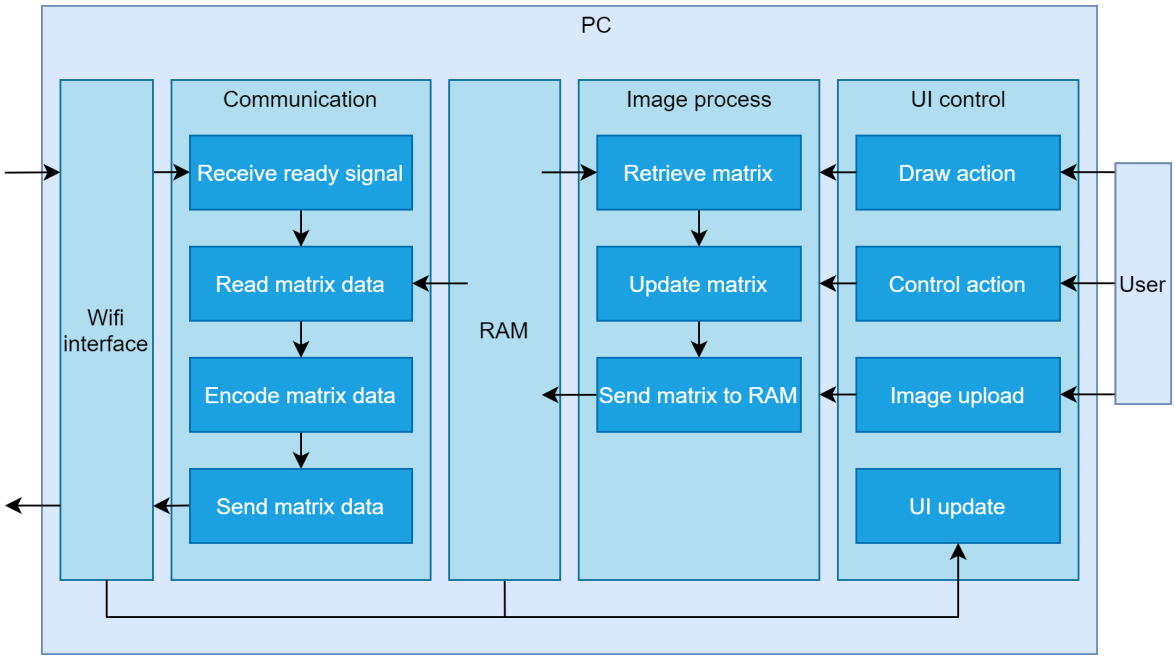

Figure 3.12: Software design diagram of PC

Figure 3.12 is the software diagram running on PC. The main task of PC software is processing the user input and visualizing matrix data. Moreover, processing matrix data before sending it to *Control Module*. Different tasks in PC software are running with different threads. Thus no tickers are needed for them. Also, usually, a PC has a powerful CPU running at GHz, the execution time of PC software can be ignored.

Pc software is programmed with *Python* language, which has become the most common programming language enabling the PC software to merge into other programs easily. Also, *Python* has excellent compatibility with different operating systems such as *Windows*, *Linux*, and *macOS*.

When receiving the ready signal from *Driver Module*, PC software will immediately read matrix data from PC RAM and encode it into *Byte* form. Then send the encoded matrix to *Driver Module* through Wi-Fi. The matrix data stored in RAM and Wi-Fi connection status will be displayed on UI real-time.

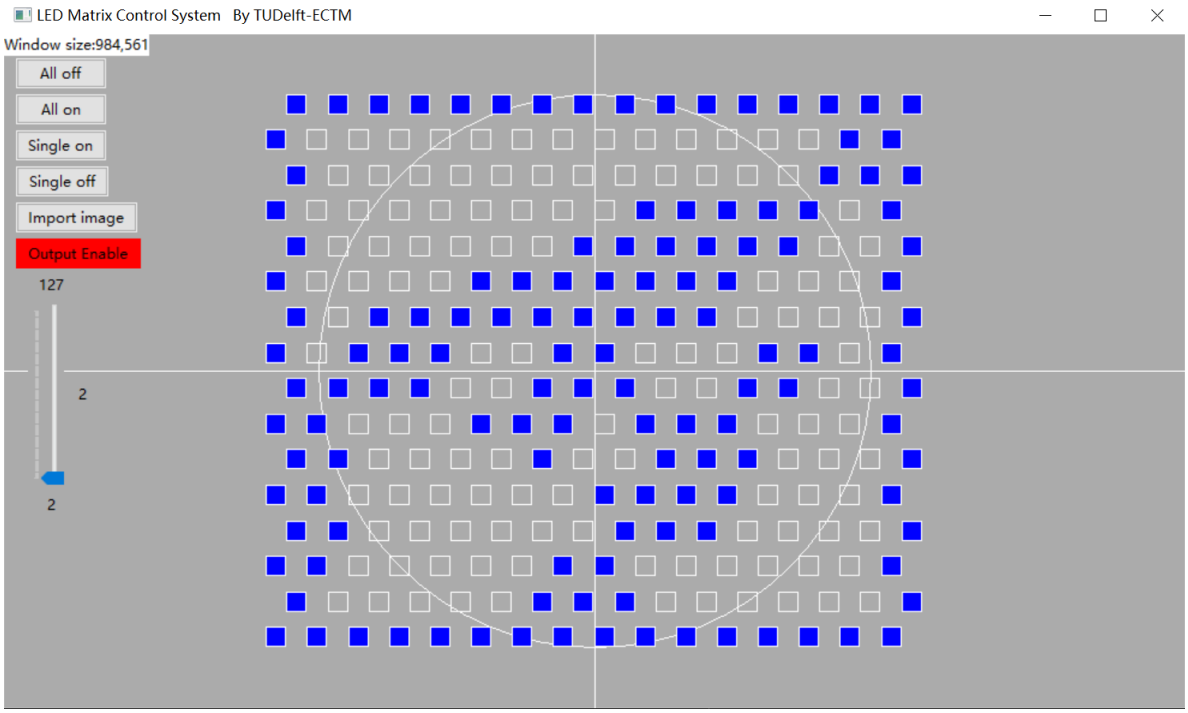

Figure 3.13: PC software UI showing *TUDelft* logo

Figure 3.13 is the UI of PC software. In the middle of the UI is the visualization of matrix pattern. The layout of the matrix in UI is identical to the real LED matrix. A rectangle in the UI matrix represents an LED. Empty box meaning the LED is off. Otherwise, blue box means the LED is on. There is a list of widgets on the left side, including 6 buttons and a slide bar. The first 2 buttons can turn on or off all LEDs. The next two can modify the status of one specified LED. Any external mono channel images with 16×16 pixel can be imported into the software by pressing the *Import Image* button. The matrix will keep off if *Output Enable* is off. Press the button can switch the output enable status, red meaning false, blue meaning true. Apart from that, this button is also an indicator of Wi-Fi status. If Wi-Fi is connected with *Control Module*, the button text *Output Enable* will keep blinking from white to black. The scroll bar at the bottom can adjust the global output radiant intensity from 0 to 127, representing off to maximum power.

Any matrix modification operation made on the UI will immediately be processed by the background image process thread. It will retrieve the current matrix data from RAM and update it according to the user input and store it back to RAM. This will make sure the communication thread using the up-to-date matrix data.

3.2.6 System overview

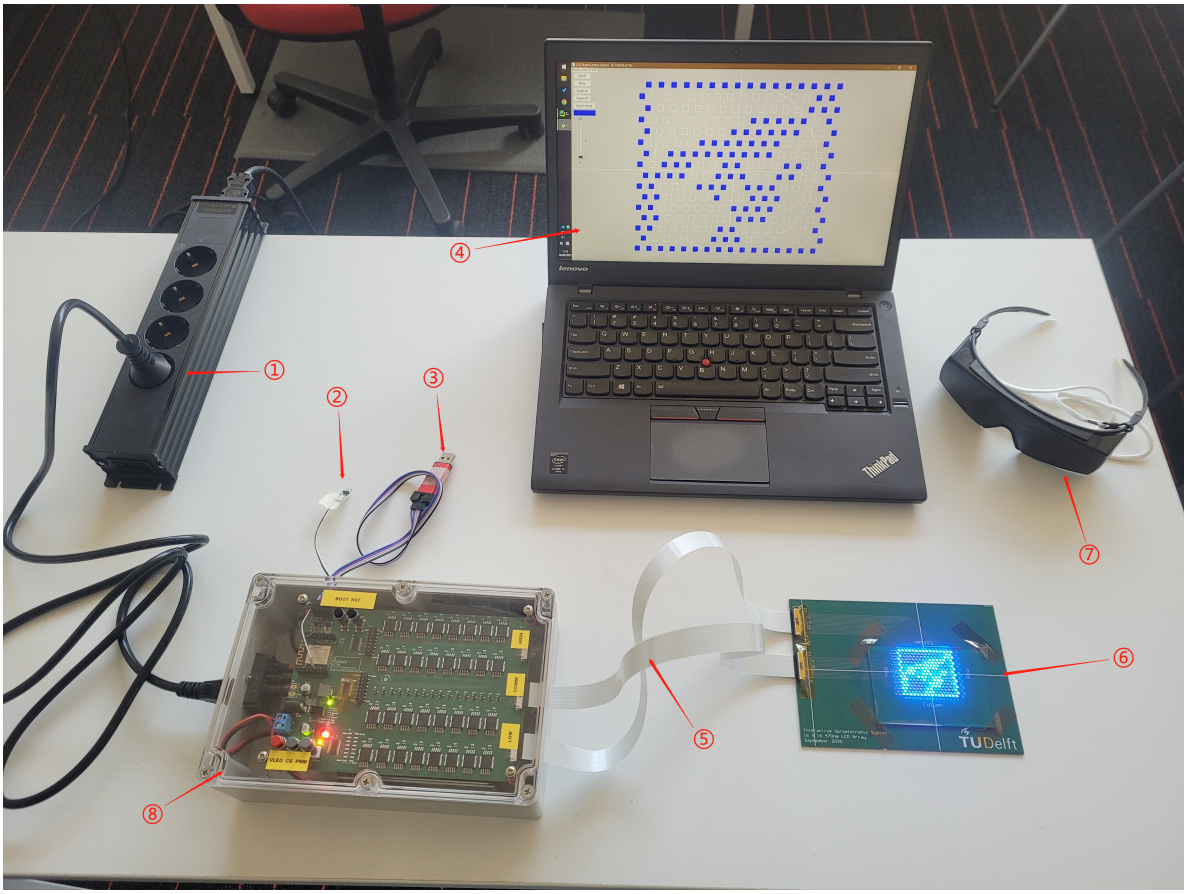

Figure 3.14: *Interactive opto-electronics system* overview

After finishing the hardware and software design, a system overview including all the system components are shown in Figure 3.14 with labels:

1 220V power socket

2 External trigger

3 Debug port

4 PC software UI displaying *TUDelft* logo

5 FFC cable connecting *Control Module* and LED matrix

6 LED matrix displaying *TUDelft* logo

7 Eye protection goggles

8 *Control Module*

3.3 MEASUREMENT

After the whole system finishing assembling, a series of measurements are performed to test the system's performance. Moreover, to check if the system meets the design requirements.

3.3.1 Latency measurement

Measurement protocol

In this measurement, using PC software to generate a random 16*16, 0-255 matrix and transmit this matrix to *Control Module* via Wi-Fi network. *Control Module* will send a "Ready" signal to PC software first, then PC software will generate the matrix and send it back as soon as it receives the "Ready" signal. The time used for PC software to generate the matrix can be ignored compared to transmit time. *Control Module* will record the time between it send the "Ready" signal and fully receive the matrix data. Repeat this operation 1000 times and record all time values. Then, keep the system running for 1 hour to check the stability by taking another 1000 time values after 1 hour.

To simulate the worst application condition, *Control Module* and PC are both connected to a router placed 3 meters away from each other shown in Figure 3.15.

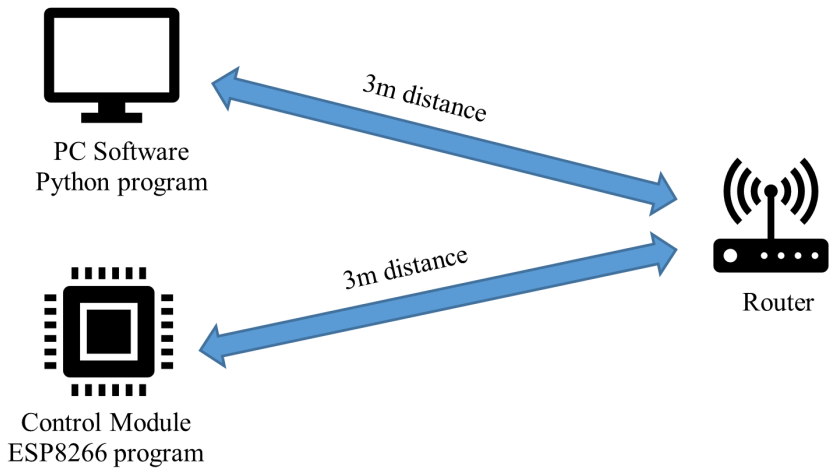

Figure 3.15: Experiment setup of latency measurement

Result analysis

Choose the first 1000 time points from the data set and list the latency in Figure 3.16a. Only 3 out of 1000 points are exceeding the 60ms latency requirement limit. The average latency is 6.7 ms. Then choose 5 ms as a section and distribute

all the data points into these sections as shown in Figure 3.16b. According to Figure 3.16, over 85% of transmission takes less than 8ms. In some infrequent situations, less than 0.1%, it takes more than 60 ms to transmit one matrix due to some rare interference. The overall latency can still shorter than 60 ms.

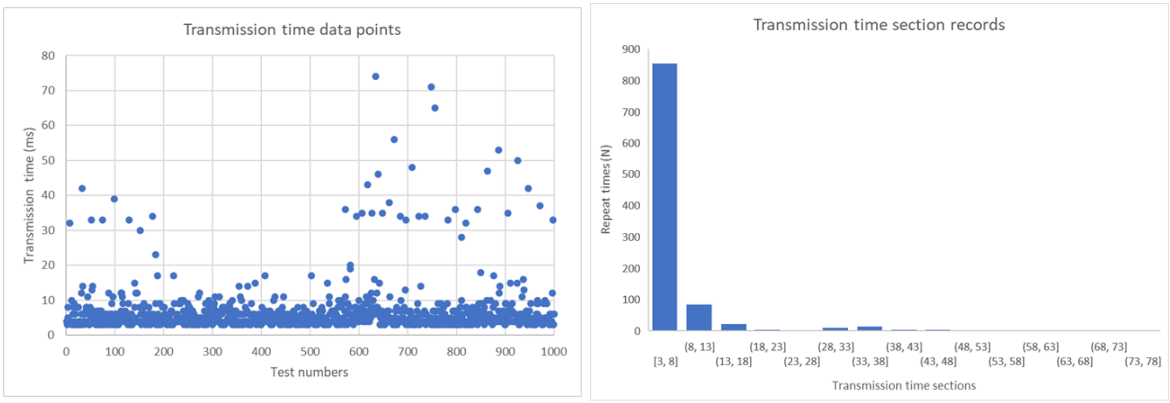

(a) (b)

Figure 3.16: (a)The first 1000 data points from latency measurement. (b)Distribution of system latency by section of 5ms.

After a 1-hour operation, another 1000 data points are recorded in Figure 3.17a. There are no data points that exceed the 60 ms upper limit after 1-hour continuous operation. The average latency is 4.8 ms. To see the distribution of time points, sort the data points into 5 ms sections in Figure 3.17b.

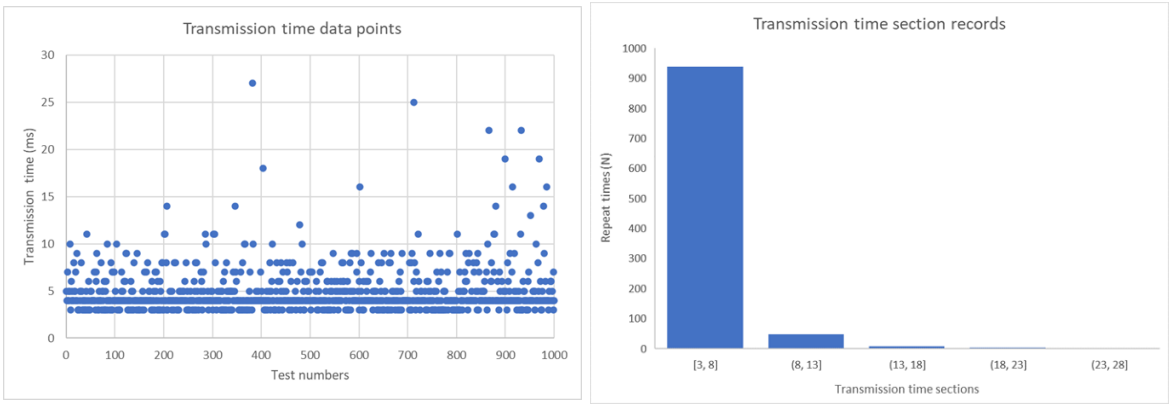

(a) (b)

Figure 3.17: (a)1000 data points after 1 hour latency measurement. (b)Distribution of system latency by section of 5ms.

The system keeps stable after a 1-hour stress test achieving the system requirements.

3.3.2 Waveform measurement

Measurement protocol

After finishing the development of the system, waveform tests are performed to specify the actual illumination power and system refresh speed. The total power reduction can be derived by waveform test using the timing relations between each line sweep. The output pin test points of PCA9635 are shown in Figure 3.18. Tests are performed in the following steps using oscilloscope: 1) Test the singe pin output waveform at point a. This test aims to test the single sweep time by measure the pulse width of the sweep signal. The result can reflect the IIC communication speed of the row control chip. 2) Test the waveform of pin a and b using two channels. By measuring the time interval between the pulses, the sweep delay of two different rows can be defined. This parameter can also represent the IIC communication time of the column chip. 3) Test the waveform of pin a and c using two channels and record the time from the pulse of pin a to the pulse of pin c. Then, total sweep time can be measured.

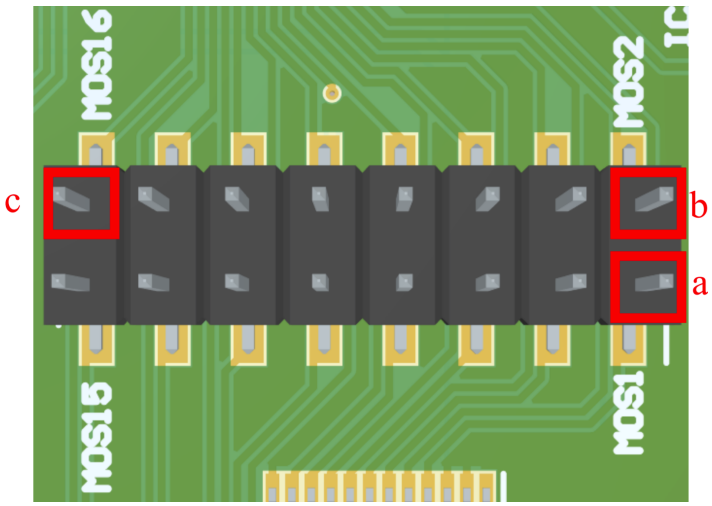

Figure 3.18: Test point of row control (row) chip.Pin a and b is the output control signal of the first and second row, pin c is the output for the last (16) row.

Figure 3.19 shows the control logic of the matrix sweep. First, prepare all the column data of the first row and write it to the row control chip through IIC port, then turn on the first row and wait for a concise time. Then turn off the first row and begin to prepare the data for the second row, and light up the second row. After repeat this logic 16 times, the whole matrix finishes one sweep loop. If this sweep action is faster than 24 Hz, higher than human visual persistence, the matrix can display patterns that the human eye can observe[50]. The sweep loop time in this system is set to 8 ms (125 Hz) in this application.

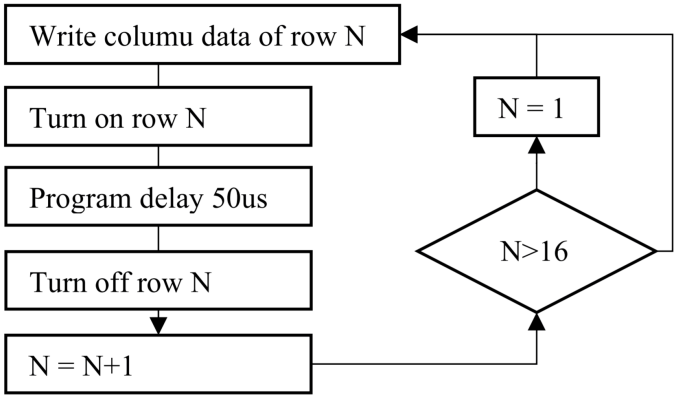

Figure 3.19: Flow chart of the matrix sweep logic. This loop repeats 16 times in 8ms.

Data analysis

Figure 3.20 is the waveform measured at test pin a in Figure 3.18, it represents the gate voltage of row selection PMOS transistors. The source of the PMOS is connected to the LED power source, which is 4.8 V. According to the technical specification of the PMOS transistor, the typical threshold voltage is -0.65 V, meaning that the transistor will turn on when the gate voltage is 0.65 V lower than the source voltage. In Figure 3.20 left, the time of each row selection is from turn-on point to cut-off point. So, each row selection time is 162 µs. This time includes the program delay, row selection signal transmission time, and gate capacitor discharge time. From Figure 3.20 right, the interval of every sweep action is 8 ms, which is fixed by the sweep loop ticker.

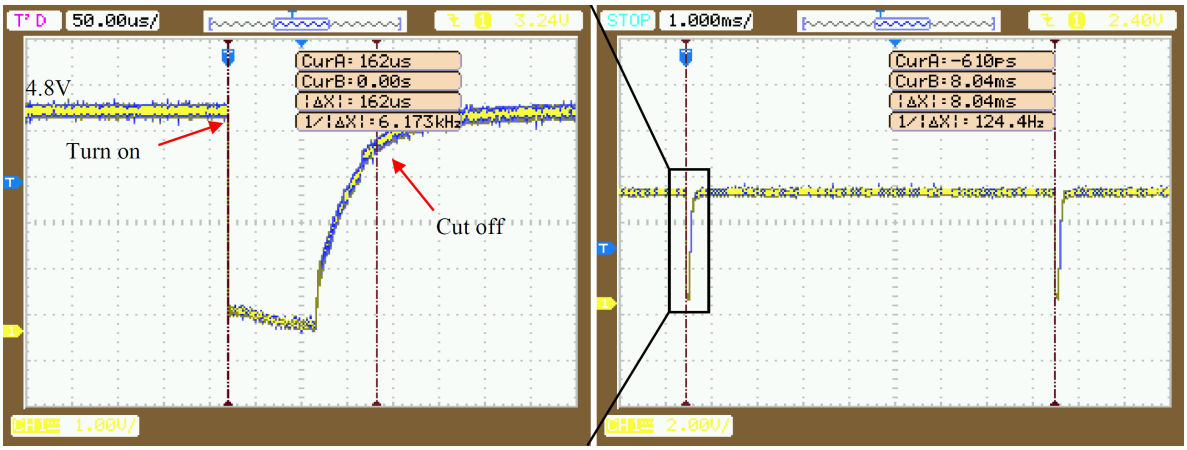

Figure 3.20: Waveform measured at test pin a in Figure 3.18. Left is the magnification waveform of each row sweep action.

Using the sweep action interval and time for single row selection time, the total power reduction coefficient can be calculated. At every sweep moment, only one row of LED will turn on for 162 µs. So, in the whole scan loop, the total turn-on

time is 162 µs times the total row number (16), equivalent to the full power of one LED row, which means the final result should be divided by total row number to get the true coefficient, which is 0.02 after calculation (2% of the full power of LED). The maximum power of each LED chip is 3.5 W. So, the LED matrix maximum power consumption is $3.5W \times 256 \times 0.02 = 17.92W$.

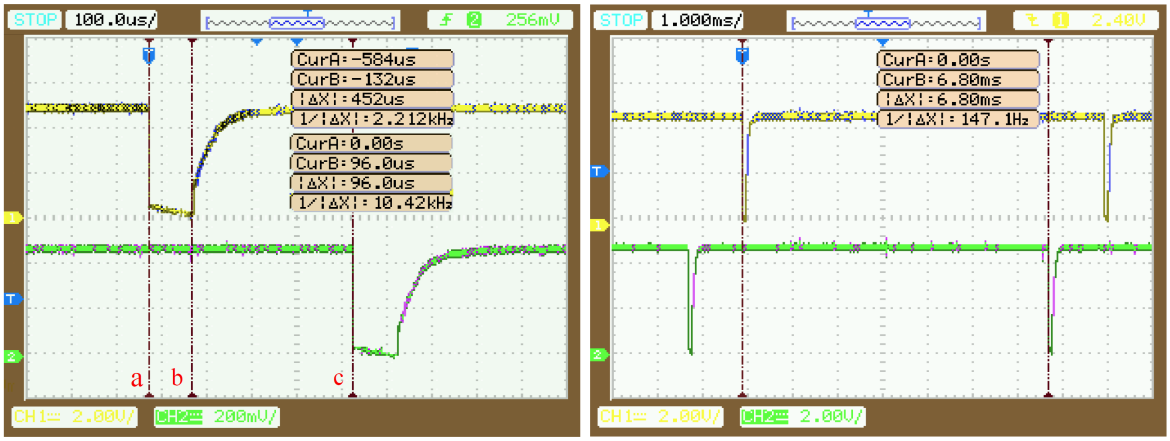

(a) (b)

Figure 3.21: (a)Waveform measured at pin a and b in Figure 3.18 with two channels. (b)Waveform measured at pin a and c in Figure 3.18 with two channels.

Figure 3.21a is the waveform measured at pin a and b with two channels of the oscilloscope. The yellow waveform is measured from pin a, and the green one is measured from pin b. This figure shows the sweep action from the previous row to next row. Point a shows row N is turned on and turn off at point b. Then from point b to c is the preparation of column data of N+1 row and turn on the N+1 row when column data is ready at point c. Time between a and b is 96 µs (program delay + row signal transmission) and between a and c (program delay + 2×row signal transmission + column signal transmission) is 452 µs. As a result, time for signal transmission can be calculated. Row signal transmission time is 46 µs and column signal transmission time is 310 µs.

Figure 3.21b shows the total sweep time by measure the time between the first row and the last row. To prevent the flicker and unstable image, an interval is designed between the end of each sweep loop and the start of next loop. So, the total sweep time is 6.8 ms which still has 1.2 ms before the start of next tick.

3.3.3 Light intensity measurement

Measurement protocal

The tool to measure the light intensity is *Thorlabs S142C* optical power meter. Place the measurement window against the center of the matrix shown in Figure 3.22a.

Set the pattern as full-on and set the light intensity from low to high by changing the number from 2 to 127 in UI, reading and recording the value on *Thorlabs PM400* console, the whole measurement setup is shown in Figure 3.22b.

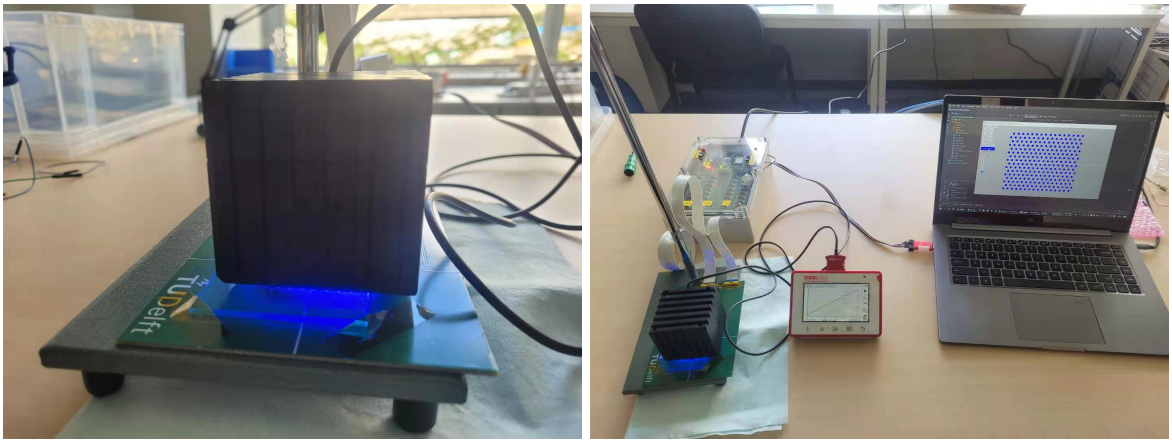

(a) (b)

Figure 3.22: (a)*Thorlabs S142C* placed on the center of the matrix. (b)The overall measurement setup.

Repeat the measurement procedure both on low range output and high range output.

Data analysis

The light intensity data is plotted in Figure 3.23. High range output and low range output is plotted in the same figure.

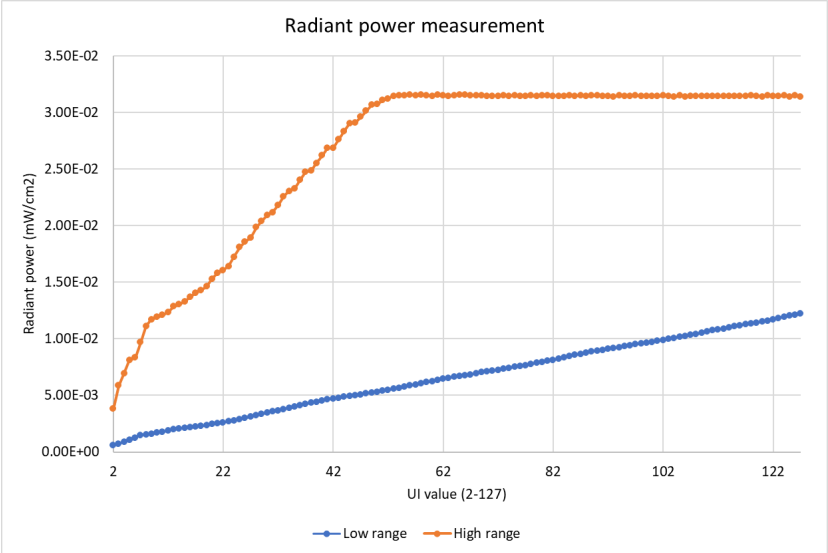

Figure 3.23: Matrix intensity measurement result

Shown in the figure, the high range output is no linear lower than $12\,\mathrm{mW\,m^{-2}}$, where low range output can compensate this nonlinearity. The maximum output intensity is $32\,\mathrm{mW\,m^{-2}}$. This is limited by the output capacity of the power supply.

3.4 RESULTS

A series of optogenetics experiments using epicardial cell monolayers was performed in LUMC using the *Interactive optoelectronic system*. The system is installed on the microscopy opto voltage mapping system shown in Figure 3.24.

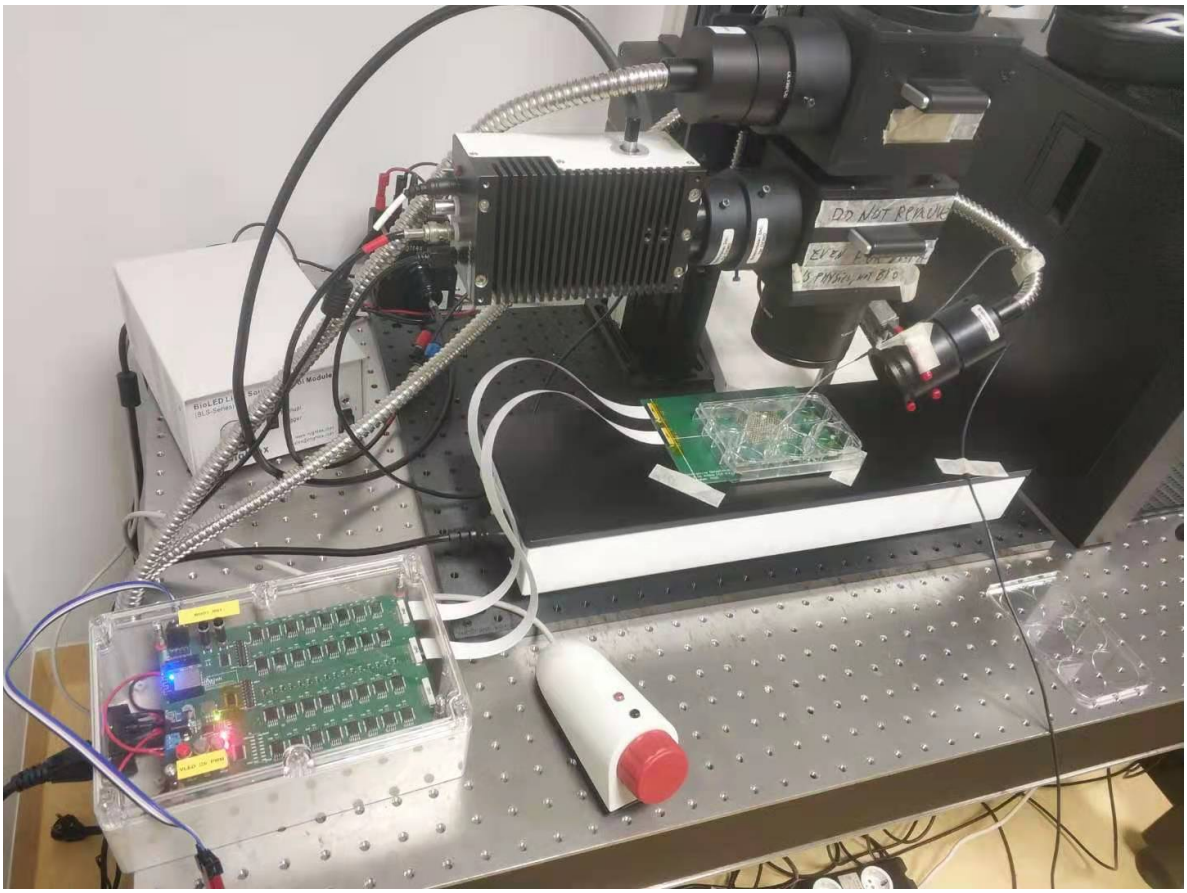

Figure 3.24: *Interactive opto-electronics system* installed on opto mapping system at LUMC

The biological experiments include pacing the epicardial cell using single-pixel flashing and AF termination test using global illumination and pattern illumination. The experiments show a single LED flash could pace the epicardial cell. AF termination is also successfully using both global illumination and pattern illumination.

During the experiment, a fluorescent dye indicator is introduced into the cells to indicate the membrane voltage. The membrane voltage of the epicardial cell can

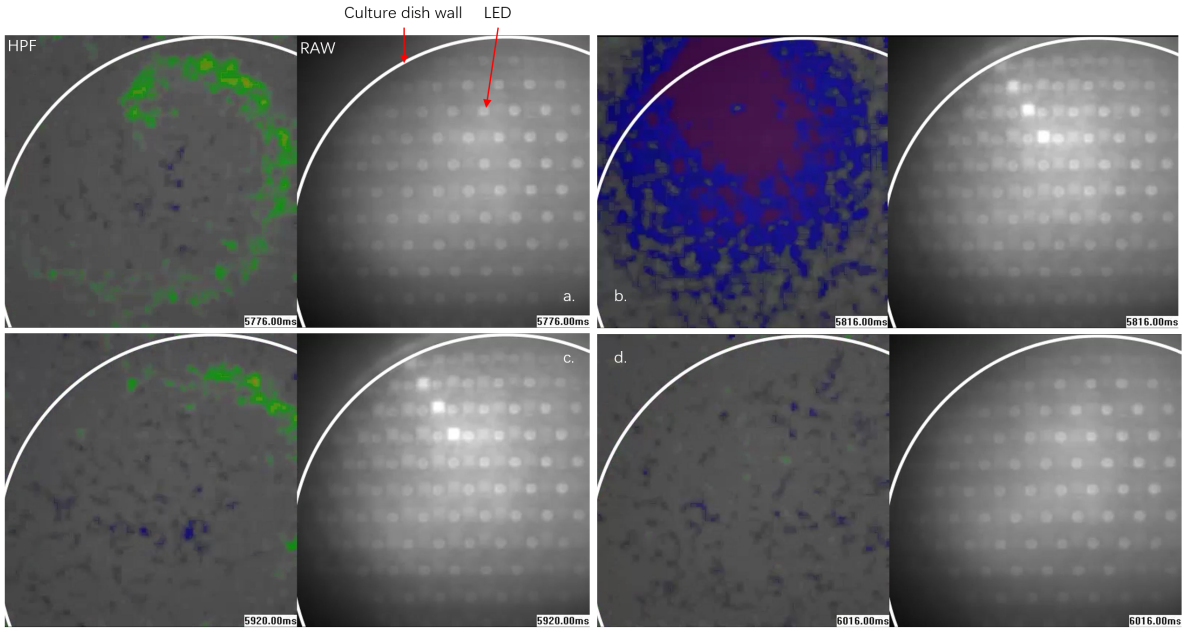

Figure 3.25: AF termination experiment result

represent the contraction activity. Figure 3.25 shows the result of the AF termination experiment. The cells are in the culture dish attached to the LED matrix. The wall of the culture dish and LEDs can be seen in the raw image. To see the cell activity better, a high pass filter (HPF) is applied to the raw image just to show the moving part of the image. In Figure 3.25 a, the AF is occurring in the shape of a spiral wave. Then the light pattern displayed in Figure 3.25 b, forming a line from the center of the spiral to the broader of the layer. The spiral wave is disintegration when touched by the light pattern in Figure 3.25 c, then disappears at last.

3.5 CONCLUSION

The driver module designed for *Interactive optoelectronics system* successfully driven the high-power LED matrix and fulfilled all the requirements. The biomedical experiments performed with the system also have a nice result. This project proved the design methodology for driving a high-power matrix system is feasible. Using the high power array driving method developed in *UVC virus inactivation test platform-Driver module* as the column driver adding a row scanning driver managed to drive this high power matrix.

The user interface on PC makes the operation much easier than onboard keypad and screen. A more advanced operation like real-time drawing and image processing can be performed with a PC interface. In the future, this PC interface could also

act as an entry point for other projects to control the *Interactive optoelectronics system*.

Though the driver system reaches the required target, there are some new issues that came up during the biomedical experiment. The light intensity is high enough to excite cells. However, the pattern resolution is not enough, 16×16 matrix resolution sometimes not enough to display some fine patterns. Moreover, the refresh speed is not high enough. 125 Hz refresh speed is high enough for consumer electronics displays but not for biomedical applications. The cells are occasionally triggered by the LED flash caused by refresh scan, a higher refreshing speed can effectively avoid this problem. These drawbacks should take into consideration in future designs.

3.5.1 Future developments

A next-generation design of optoelectronics matrix driving system will be shown. This design is aiming to drive a micro-LED matrix with much higher density. The global illumination radiant will be kept almost the same. The driving system diagram is shown in Figure 3.26. The next-generation driving system will drive a 96×96 micro-LED matrix with over 300 Hz refreshing speed. Instead of MCU, FPGA will become the controller in this design to handle much higher refresh speed and image data conversion load. In the diagram, all the chips and connections are marked.

3.5.2 Extend application

The design of high power LED matrix could also become a projector driver. The LED matrix has a total power of over 20 W, whose power is equal to a portable projector. If the micro-LED can reach a higher resolution to FHD (1920×1080), adding optics systems, a mini projector can be assembled using this technology. Because there is no reflection unit such as DMD (digital micromirror device) used in this projector design, the efficiency will be much higher than current projectors.

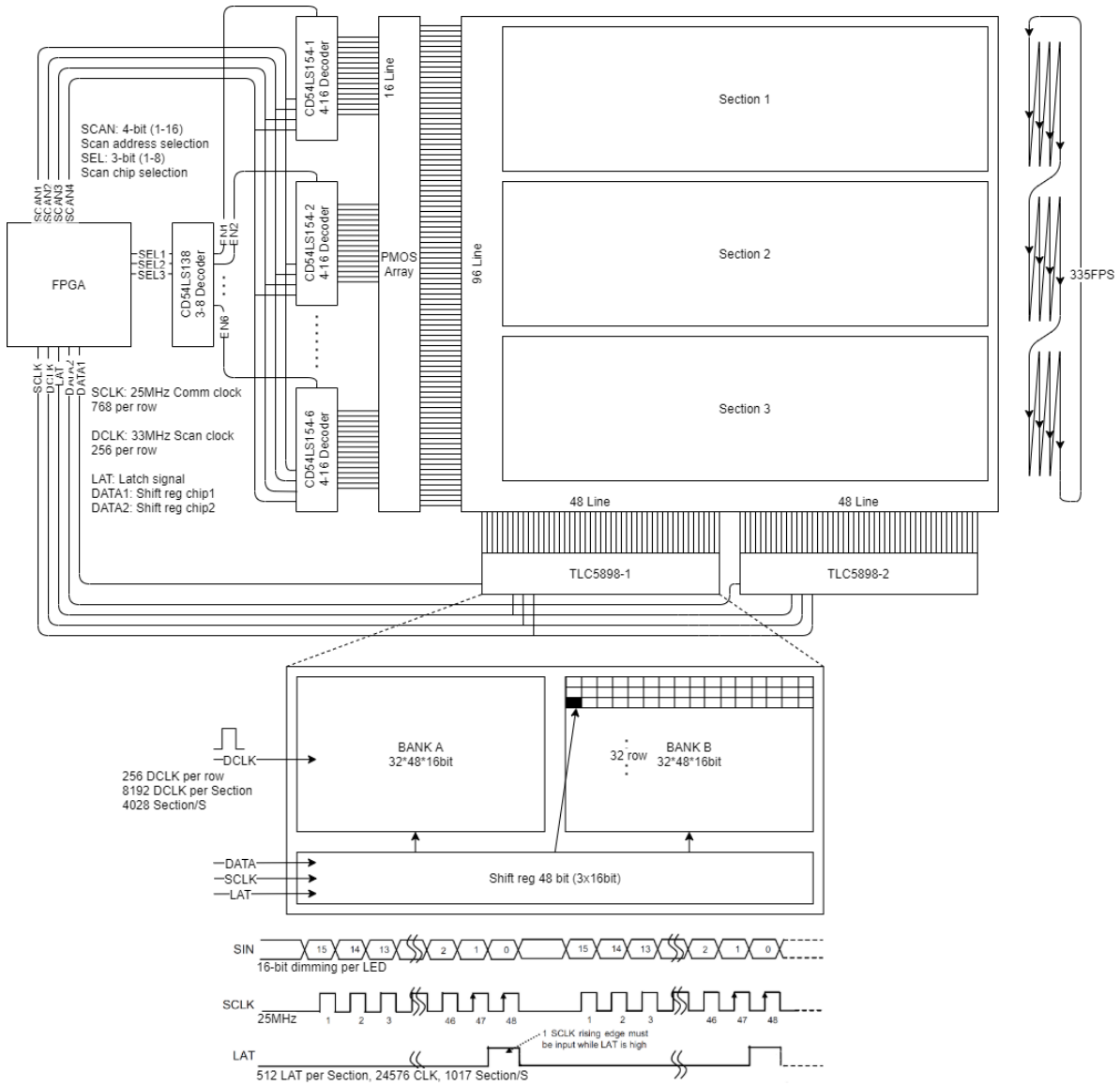

Figure 3.26: System diagram for next generation matrix driver.

4 SELF-POWERED DRIVER SYSTEM

4.1 INTRODUCTION

After developing the driver system itself, the next step is to power the driver system with the contactless or self-powering method. The ultimate goal of biomedical electronics is wearable or in-vivo implantation. Thus a power wire is not feasible in these circumstances. This chapter will first review existing technology, discuss its pros and cons, and then choose the most suitable method to design a self-powered advanced driver system.

4.1.1 Background

Apart from LED opto-stimulation moments, bio-electronics devices are in standby mode most of the time. Only sensors are activating to monitor biomedical signals. For example, the *Interactive optoelectronics system* will only flash the LED for less than 0.1s to terminate AF when triggered, while the ECG sensor will continuously monitor the heart condition. As a result, powering biomedical sensors is another important feature of the driver system. At present, almost all biomedical sensors are powered by external power supplies or batteries, bulky and need to charge or change regularly[53]. The powering issue becomes a big obstacle between research and the real application of implantable and wearable biomedical devices[54]. As a result, developing a driver system that requires no external power supplies becomes significant to push the further application of biomedical devices.

In response to this demand, all kinds of power generation technology have been tried to collect energy from the environment surrounding human bodies shown in Figure 4.1. This power generation technology includes solar cells[55], electromagnetic generators[56], biofuel cells,[57] and thermoelectric generator[58]. In 2006, Wang's team came up with a nanogenerator (NG), which can collect low-frequency mechanical energy and transfer it into electric energy[59]. Moreover, in recent years, using the electromagnetic generator theory, wireless power transfer (WPT) technology reaches a high system efficiency of 70% and a power rate of 80 W[60]. Using one or a combination of these self-power technologies, there will be more options for biomedical sensors' energy supply method.

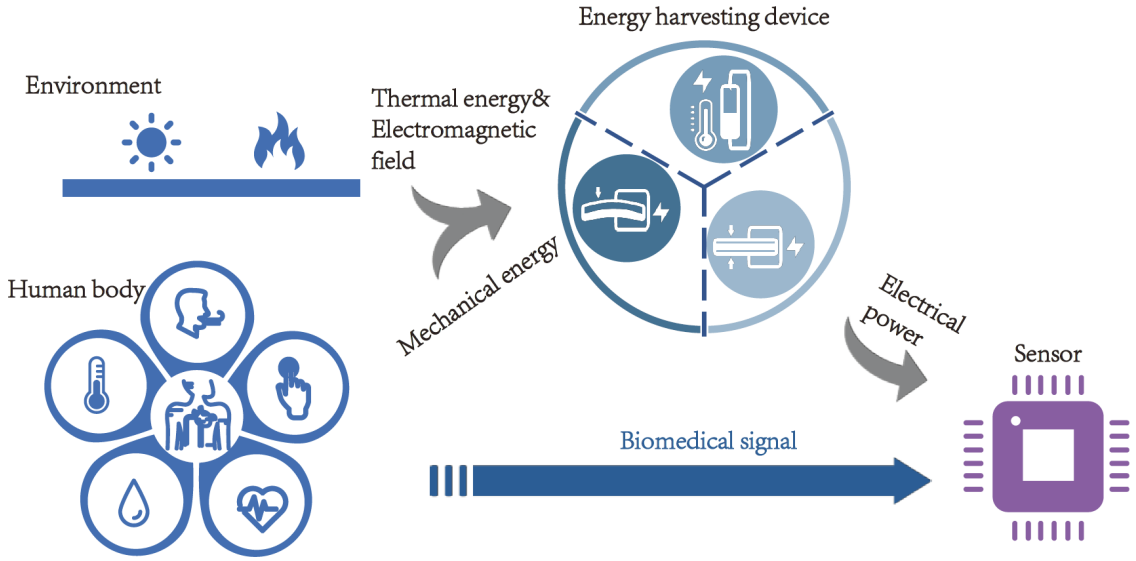

Figure 4.1: Self-power driver system diagram

Moreover, besides powering up sensors, the power generator itself can become sensors. The output power of the generator indicates the state of the medium used to harvest power[61]. For example, a triboelectric nanogenerator (TENG) can act as a movement sensor[62].

However, it is not enough for the driver system to only power up the sensors. It also needs to make respond to the bio-activities, in this case, triggering the LED. The actuators need more power to drive. An ECG sensor costs less than 10mA at a maximum sampling rate[63], comparing to 1 A per LED. There are few reports that evaluate the output availability of self-power generators.

4.1.2 Objective

After reviewing and understanding the theory of the self-power method, evaluate the feasibility of designing a self-powered advanced driver system. Apart from driving the sensors, the drive system also needs to drive high-power LEDs, requiring much more power than sensors. Though the self-power method has already proven can drive biomedical low-power sensors, its ability to drive high-power optoelectrical devices is still debatable.

4.2 THEORY OF NANOGENERATOR

Nanogenerator (NG) is an energy conversion technology that converts mechanical or thermal energy produced by small-scale physical change into electrical energy.

There are three typical NG types: piezoelectric (PE), triboelectric (TE), and thermoelectric generators. Both PENG and TENG can convert mechanical energy to electricity. While thermoelectric generators can harvest energy from temperature fluctuation[4, 64].

4.2.1 Piezoelectric nanogenerator

The piezoelectric effect was discovered by scientists for a long time. In recent years, it has been widely used in the field of bio-electronic devices[65]. The piezoelectric effect refers to the phenomenon that when an external force deforms a piezoelectric material in a certain direction, the internal polarization occurs, and a piezoelectric potential is generated. ZnO crystal is a classic piezoelectric material, Zn^{2+} and O^{2-} inside it stacked in regular octahedral structure along its c axis, shown in Figure 4.2a. When there is no external force applied to the crystal, the center of positive charge and negative charge are at the same position. If the external force is applied to any crystal axis, the center of the charges will form an offset that causes a dipole moment. This dipole moment generates a potential difference along the axis naming piezoelectric potential, illustrate in Figure 4.2b. Connect the piezoelectric material into a load circuit along its axis, a current will form[66].

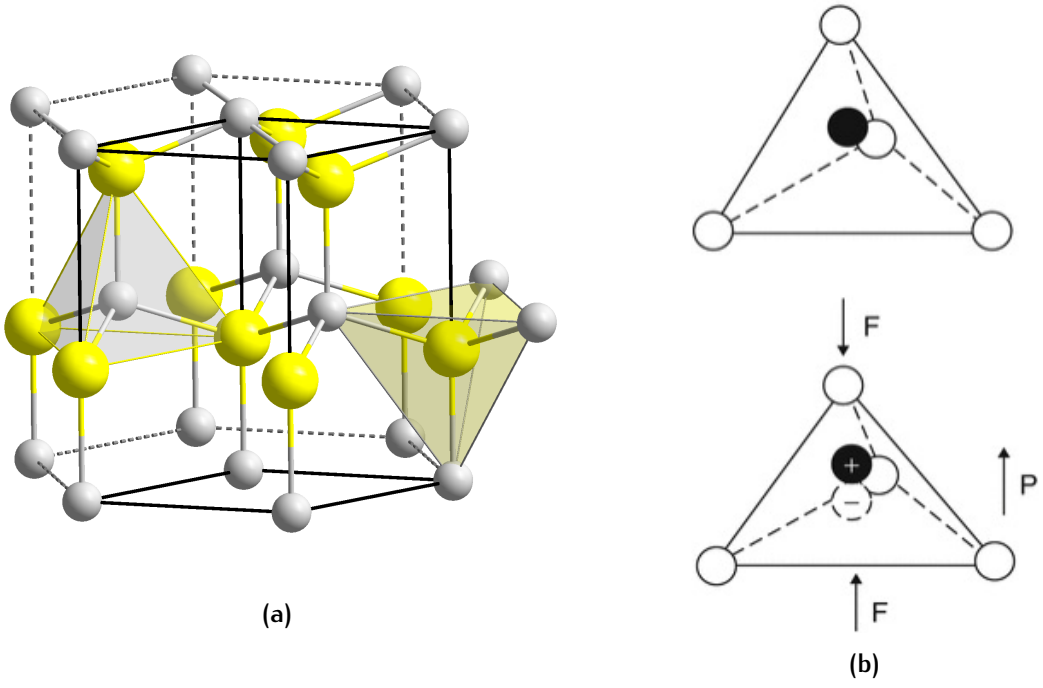

Figure 4.2: (a)Crystal structure of *Zno*. (b)Piezoelectric potential of *ZnO* when pressed.

Based on this theory, in 2006, Wang came up with PENG[59]. The early stage of PENG chose brittle inorganic material, which not suitable for biomedical application. New organic piezoelectric material like *PVDF* has been discovered with further

research, pushing piezoelectric material towards flexible and thin-film. This enables PENG a suitable technology for powering bio-electronics.

In 2010, Li et al. designed an implantable PENG, harvest energy from mice heart beating[67]. This device's output capacity is relatively low, with a peak voltage of 50 mV and a current of 500 pA. However, this work first proves the possibility of PENG being an electrical power provider for in-vivo biomedical devices. Later increasing researchers put forward new designs with better performance.

4.2.2 Triboelectric nanogenerator

In 2012, Fan et al. proposed a new nanogenerator structure using a combination of the triboelectric effect and electrostatic induction effect[68]. After two different materials rub against each other, one material will be positively charged due to the difference in their ability to absorb electrons. In contrast, the other material will be negatively charged. Meanwhile, induced charges are generated on the back electrode placed on the materials. Like PENG, connecting the electrode to an external load, a current will produce when the materials are moving. This kind of nanogenerator is called a triboelectric nanogenerator (TENG).

Charge	Materials
Positive	Air
	Human hands
	Glass
	Wool
	Nylon
	Viscose
	Cotton
	Silk
	Acetate
	Polymethyl methacrylate
	Polyester
	Orlon
	Polyethylene
	Vinyl (PVC)
	Silicon
Negative	Teflon

Table 4.1: Triboelectric series of common materials

TENG can be formed by many kinds of materials. In principle, any two different materials can form a TENG[69]. However, materials far away in *triboelectric series*, which arrange the materials by the relative polarity of the contact charge

acquisition ability, will have better efficiency[70]. Some common materials are listed in Table 4.1[71, 72]. On the other hand, TENG can harvest low-frequency mechanical power at high efficiency. Because human movements are mainly categorized as low-frequency motion, TENG is especially suitable for biomedical energy harvesting[73].

There are 4 basic modes of TENG. They are

- Vertical contact-separation mode
- Lateral sliding mode
- Single electrode mode
- Freestanding triboelectric-layer mode

. Which can be used in different applications.

Vertical contact-separation mode

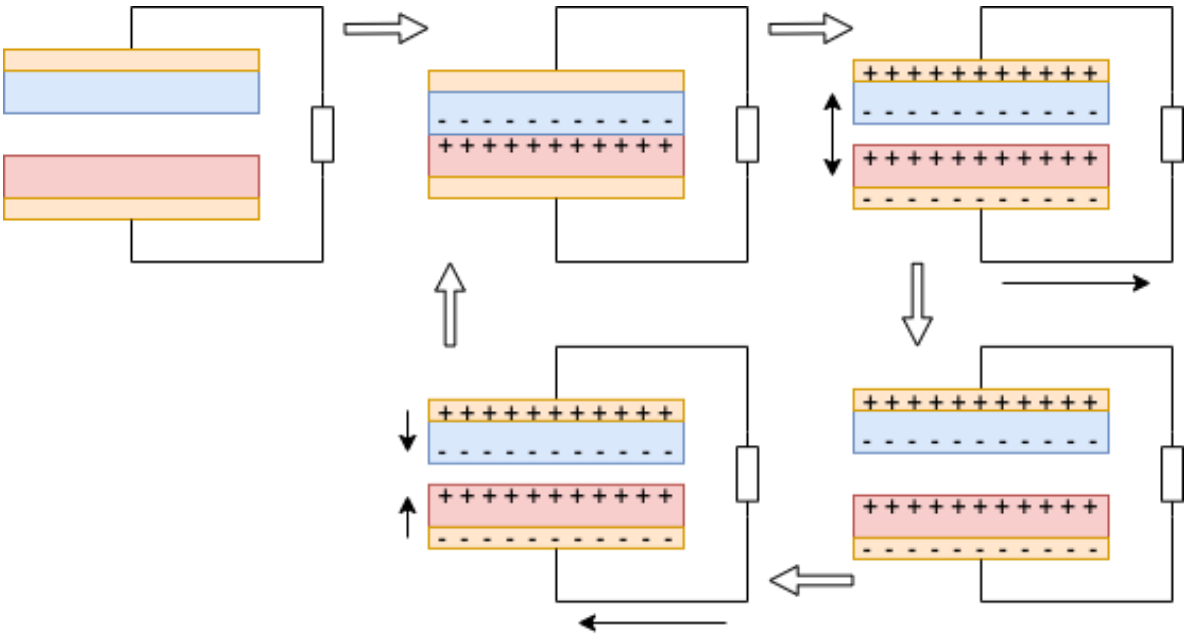

Figure 4.3: Vertical contact-separation mode TENG operation principal

Two sheets of insulate material with an electrode at external surface connecting to load. When the insulator is contacted, the charge transfer will begin, resulting in one surface positive charged and another negative. Then the layers are separated and induct the opposite charge on the electrode at the external surface, creating a potential difference. Current will flow through the load to balance the potential difference. Subsequently, the layers are pressed back again, and the triboelectric generated potential difference will become zero, the current will flow back. If the

layers move separately and re-contact in the cycle, an alternate current (AC) will be generated continuously[68]. Figure 4.3 shows the operation cycle of this kind of working mode.

Lateral sliding mode

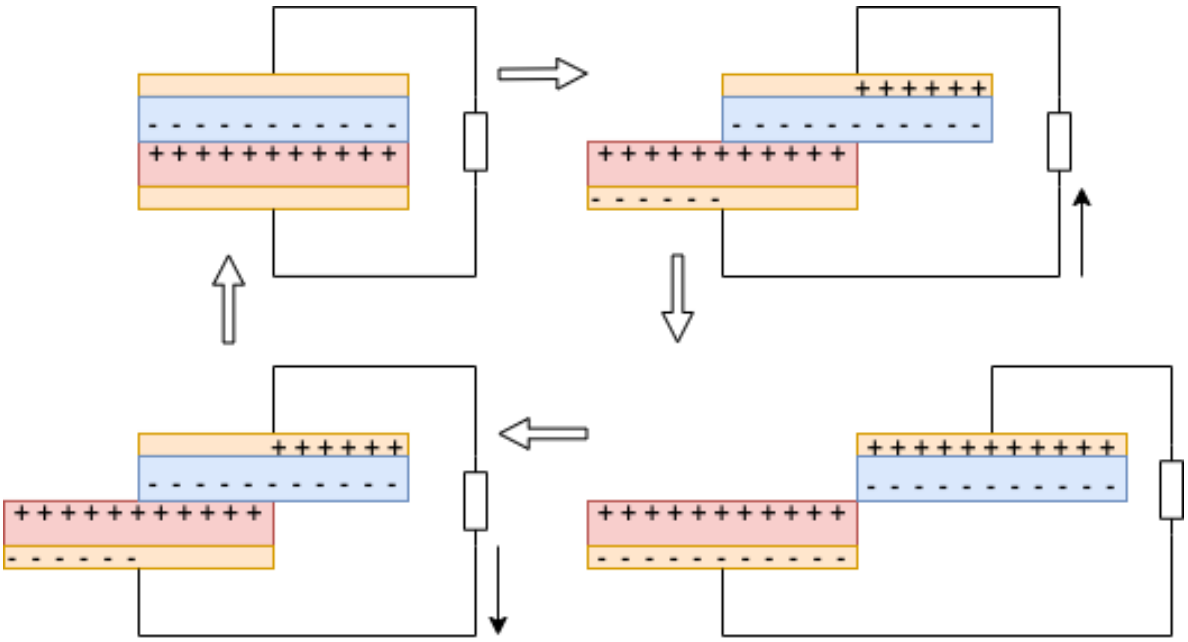

Figure 4.4: Lateral sliding mode TENG operation principal

In this mode, the structure is almost the same as vertical contact-separation mode. Unlike contact-separation, in lateral mode, the two insulating layers are making an in-plane motion and will not separate. When the two layers are right above each other, there will be no induction charge on the electrode at the backside. If the layers sliding apart, surfaces not in contact with each other will generate triboelectric charge-induced potential at the back electrode. This can form a current through external load until the plates are fully separated. Subsequently, when the layers moving back, the triboelectric charge-induced potential begins decreasing to zero, the current flowing back until the surface right to each other. Cycling this motion will create an AC, shown in Figure 4.4. Moreover, the lateral sliding mode can operate either in-plane moving or rotation[74, 75].

Single electrode mode

Single electrode mode is a more practical design with less structure. There is only one electrode on the backside of one insulator comparing to both in vertical contact-separation mode. This electrode is connected to ground via the external load. When the two insulators separate, similar to vertical contact-separation mode, triboelectric

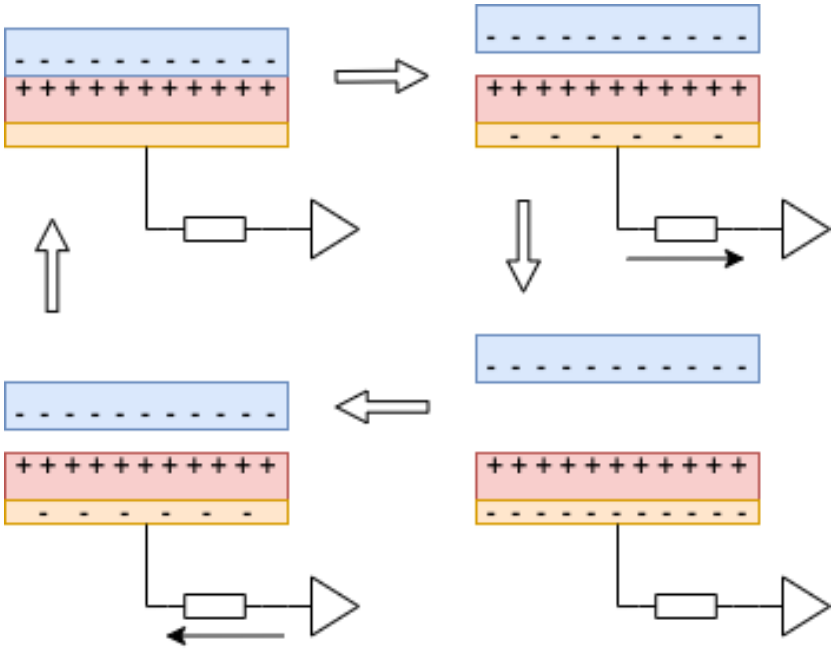

Figure 4.5: Single electrode mode TENG operation principal

charge induced potential will charge the electrode. The current will flow through the load to balance the potential from ground. Later, the layers move back to each other, the potential comes to zero, and current flows back to ground[76]. Figure 4.5 shows the operation cycle of this mode, also creating an AC power.

Freestanding triboelectric-layer mode

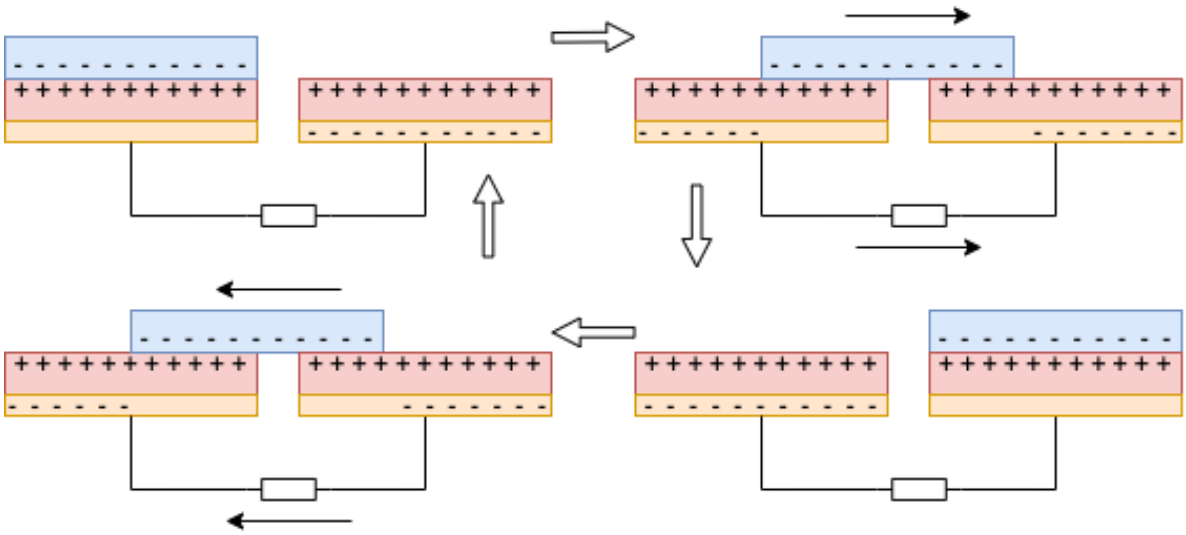

Figure 4.6: Freestanding triboelectric-layer mode TENG operation principal

In this mode, three insulators are used. Two same material layers with electrodes on the backside were fixed, with a load connected. A freestanding layer is sliding

above them. The triboelectric charge-induced charge will form at the part where the freestanding layer is not there. When the freestanding layer is moving, the charge will flow through the load to balance both electrodes' potential. If the freestanding layer moving in cycle shown in Figure 4.6, an AC will be generated[77].

4.2.3 Thermoelectric generators

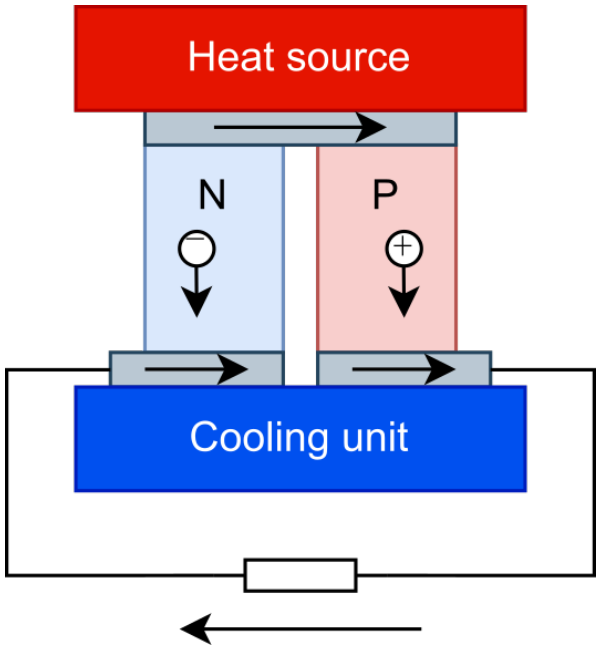

Figure 4.7: A thermoelectric generator structure

Thermal power is another common heat source in the environment. As a heat source, human can become the source of thermoelectric nanogenerators[78]. The thermoelectric effect converts temperature difference into voltage difference and vice versa a thermocouple[79] through a phenomenon called the *Seebeck effect*. A thermoelectric generator consists of two different materials connected at their ends. Usually an N-type and a P-type semiconductor, shown in Figure 4.7.

Direct current (DC) will flow through the generator and circuit when there is a temperature difference between the end of the semiconductor materials. The current strength is linear to the temperature difference according to Equation 4.1:

$$J = -\sigma S \bigtriangledown T \tag{4.1}$$

where J is current density, σ is local conductivity, S is Seebeck coefficient of the material, $\bigtriangledown T$ is the temperature gradient.

4.3 THEORY OF WIRELESS POWER TRANSFER

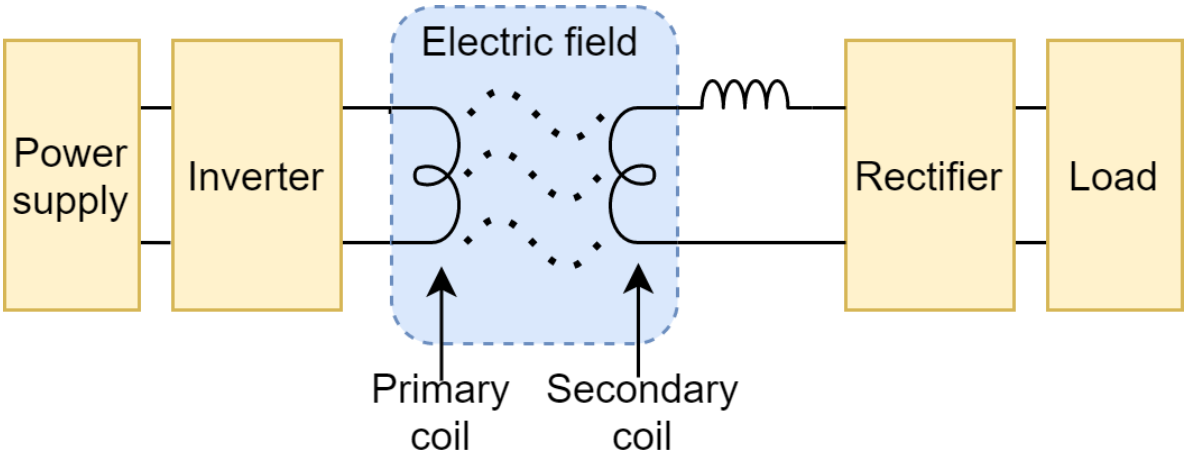

Figure 4.8: WPT block system diagram

Wireless power transfer (WPT) offers a new method for energy acquisition of electronics devices, thus alleviating the dependence on batteries[60]. The basic structure of WPT system is shown in Figure 4.8. The left part is the power transmitter, and the right part is the receiver. The electrical power will be transmitted as an alternate electrical field form between the transmitter and receiver. As a result, the load connected to the receiver can be placed in a different place from the power supply. There are three challenges as well as important technical parameters of the WPT system.

Energy Efficiency

Energy efficiency is one of the most important technical parameters of the WPT system. Each part Figure 4.8 has its own power efficiency in the transmission path. These parts define the total WPT system efficiency[80]. To improve the WPT system power efficiency, optimization can be made by better coil design[81, 82], circuit structure, and power control. A WPT system could reach 70% efficiency in some applications at a working frequency of 13.26 MHz[83].

Transmitted power

The transmitted power of a WPT system is also essential. The transmitted power is limited by switching components in inventors and control scheme[84]s. A 120 W wireless charger is currently available for commercial products according to *Qi* wireless charging standard by Wireless Power Consortium (WPC)[85].
Because the driver system needs to be implanted or worn on the body, it is impossible to put the WPT transmitter directly on the receiver. Thus the transmit distance is also a key parameter that should be taken into consideration. There are currently

some techniques that enable wireless power transfer in serial meters[86].

4.4 STATE-OF-ART

Since 2006, the first nanogenerator was proposed, there are already improvements made to increase the nanogenerator's efficiency. Besides, WPT technology has been wildly applied in smartphone charging. In this part, some state-of-the-art research results will be introduced to show the self-powered technology feasibility of driving the optoelectronics driver system.

4.4.1 Nanogenerator (NG)

Though NG is a relatively new technology. There are more than 500 publications related to NG in 2020. New design and applications have been wildly discovered in recent years. A summary of NGs is listed in Table 4.2 with a series of the most cited NG designs.

PENG

The first PENG was developed in 2006 based on ZnO nanowires[59]. The ZnO nanowire was pressed by a conductive AFM tip and output a voltage of 8 mV and 0.5 pW power. In 2007, Wang et al. designed a ZnO PENG driven by an ultrasonic wave at 41 kHz, generating an open-circuit voltage of 0.7 mV and 0.15 nA short current[87]. Qin et al. developed a PENG based on microfiber electrode and ZnO thin film in 2008. This structure generates 1 mV to 3 mV open-circuit voltage and 4 nA short current[88].

Yang et al. designed a laterally composited PENG rather than vertical mode[89]. It gives an AC output voltage of 50 mV with a low strain (0.05%-0.1%). Using this concept in 2010, Zhu et al. designed a PENG reaching an open circuit voltage of 2.03V and a short current of 107 nA[90]. A commercial LED could be lit up by storing the power generated by this structure in a capacitor. Later, Xu et al. integrated 700 ZnO nanowires together, producing a peak voltage of 1.26V and an open circuit current of 28.8 nA[91].

In 2011, Cha et al. enhanced the piezoelectric potential using different material naming polyvinylidene fluoride (PVDF), reaching 2.6V and 0.6 µA output[92]. In 2012, Zhu et al. introduced a PENG with high open-circuit voltage, which is 58V. The short current is 134 µA[93].

Ghosh et al. uses fish scale as bio-piezoelectric nanogenerator in 2016, reaching better robustly. This PENG has an output voltage of 4V and a current of 1.5 µA[94].

Xu et al. found that NKN (polymorphic phase sodium-potassium niobate) has a much more significant piezoelectric strain constant because of its special crystal structure[95].

TENG

In the year 2012, the first flexible TENG was developed by Wanf et al., which generated an open circuit voltage of 3.3V and a short current of 0.6 µA[68]. Later in the same year, Wang's team designed an arc-shaped TENG to reach a voltage of 230V[96].

In 2013, Chen et al. designed a vibrating sensor using TENG. It can produce a stable output of 284V voltage and 76.8 µA current[97]. Also, by changing the shape of TENG contact layers, TENG's efficiency can be improved a lot[98]. Zhu et al. designed a TENG using a sliding structure, which introducing a new mechanism for TENG[99].

In 2014, Lin et al. designed a TENG to harvest energy from water drops. When a 30 µL water drops on this TENG surface, it can achieve 9.3 V and 17 µA current[100].

In 2015, Sun et al. designed a bio-compatible TENG that can flash several commercial LEDs, reaching 310.5V voltage output and 16.2 µA current[101]. Later in the same year, Tao et al. using a book-shaped TENG to improve the TENG's output capability[102].

In 2016, Chen et al. designed a single electrode TENG becoming a movement sensor as well as a power generator for the reading circuit[103].

In 2017, Mallineni et al. designed a TENG with over 2000V output voltage [104].Later, more kinds of materials have been used to fabricate TENG. In 2018, a kind of sea algae has been tested as TENG layers[105]. More recently, TENG has been tested to harvest energy from all kinds of energy sources like water wave[106] and wind energy[107].

Year	Author	Open Circuit Voltage	Short Current	Area Power density	Volume Power Density	Technology
2006	Wang et al.[59]	6 mV to 9 mV		1mW/cm2		PENG
2007	Wang et al.[87]	0.7 mV	0.15 nA		4W/cm3	PENG
2008	Qin et al.[88]	1 mV to 3 mV	4 nA	20-80mW/cm2		PENG
2009	Yang et al.[89]	50 mV	400-750pA			PENG
2010	Zhu et al.[90]	2.03V	107 nA	22uW/cm2	11mW/cm3	PENG
2010	Xu et al.[91]	1.26V	28.8 nA		2.7mW/cm3	PENG
2011	Cha et al.[92]	3.6V	0.6 µA		0.17	PENG
2012	Zhu et al.[93]	58V	134 µA		0.78W/cm3	PENG
2012	Wang et al.[68]	3.3V	0.6 µA		10.4mW/cm3	TENG
2012	Wang et al.[96]	230V		15.5 µA/cm2	128mW/cm3	TENG
2013	Zhu et al.[99]	615V	0.44 µA			TENG
2013	Hu et al.[98]	110V	15 µA	276uW/cm2		TENG
2013	Chen et al.[97]	287V	76 µA	72.6uW/cm2		TENG
2013	Yang et al.[76]	428V	1.395 µA	30uW/cm2		TENG
2014	Lin et al.[100]	9.3V	17 µA	20mW/cm2		TENG
2015	Sun et al.[101]	310.5V	16.2 µA			TENG
2015	Huang et al.[102]	340V	78 µA	230uW/cm2		TENG
2016	Ghosh et al.[94]	4V	1.5 µA	1.14uW/cm2		PENG
2016	Chen et al.[103]	150V	78 µA			TENG
2017	Xu et al.[95]	35V	5 µA			PENG
2017	Mallineni et al.[104]	2000V				TENG
2018	Lee et al.[108]	65V	1.6 µA			PENG
2018	Dudem et al.[109]	14V	0.96 µA	98uW/cm2		PENG
2018	Lei et al.[108]	707V	75 µA		9.559uW/cm3	TENG
2018	Pang et al.[105]	33V	0.15 µA			TENG
2019	Maria et al.[110]	12.5V	100n	562uW/cm2		PENG
2019	Hao et al.[106]	13V	2mA			TENG

Table 4.2: Summary of designs and researches on different types of NGs

4.4.2 WPT

Near-field WPT

Wireless power transfer technology is already wildly applied in smart devices as wireless chargers. This kind of wireless charger usually uses inductive coupling[111] and capacitive coupling[112]. Using these technologies, wireless chargers can provide a maximum of 120W power.

In 2007, Kurs et al. first developed a WPT system using resonance inductive coupling. This WPT system can transfer 60W power within 2m distance with 40% power efficiency[113].

In later years, some designs for implantable biomedical sensors have been made, reaching higher efficiency listed in Table 4.3 [114, 115, 116, 117, 118]. The transmitted power is varied by the purpose of applications.

Year	Author	Power	Efficiency	Frequency	Range
2010	Kiani[114]	11.2mW	14%	13.56M	5-20mm
2015	Knecht[115]	30W	95%	800K	20-70mm
2016	Jiang[116]	100mW	60%	13.56M	5-15mm
2017	Mirbozorgi[117]	1.3mW	2.40%	60M	14-18mm
2018	Wang[118]	9.2mW	75%	13.56M	

Table 4.3: WPT designs for biomedical applications

Long-range WPT

Long-range WPT usually uses microwave[119] or laser[120] technology. It can transmit power in the kilometer range. This technology can be used to transfer the solar energy collected in space to ground[121]. This technology requires complex transmitter and receiver antenna arrays to transmit and receive power.

4.5 DISCUSSION

During the optoelectronics driver system's operation, the implanted LED matrix is only turned on for a short time when necessary. For example, to defibrillation the AF, the LEDs need to be turned on for 100ms to reach a good termination rate[1]. When the LED matrix in *Interactive optoelectronics system* is turned on at full power, it will consume 48W power. Thus, a total maximum of 4.8J power is required for each flash.

For NGs, using currently available technology, it is impossible to drive the LED array directly. Thus, an energy storage method should be included. A capacitor can store the energy generated by NG and release energy when needed. Figure 4.9 shows a possible design of an NG system with an energy storage unit. The AC will be regulated to DC by a diode bridge and stored on the capacitor. A buck converter is connected to the capacitor, adjusting the output voltage to fit the driver system.

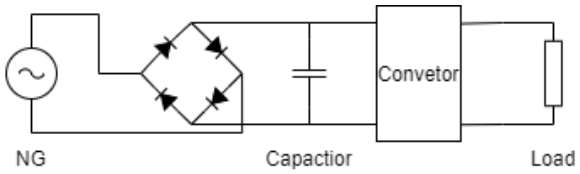

Figure 4.9: A NG power generate system with energy storage capactior

The energy stored in the capacitor can be calculated using Equation 4.2:

$$E = \frac{V^2 C}{2} \tag{4.2}$$

where V is the voltage across the capacitor, C is the capacitance of the capacitor. Using an existing TENG design, when the output voltage of NG is 200V and set capacitance as 20uF, the energy stored in the capacitor is 4J. This can supply one flash of the LED matrix. Assuming the short circuit current is 100 µA, referring to the existing TENG design, the capacitor's charging process is shown in Figure 4.10. It takes 90s to reach 90% of the final voltage, which allows the LED array to be trigged every 90s.

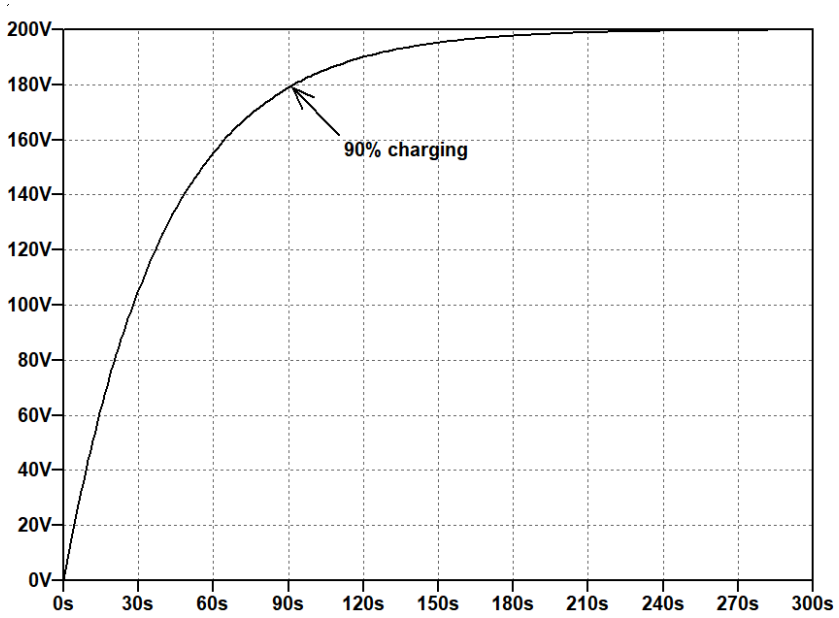

Figure 4.10: The voltage across the capactor charging with TENG at 20 µA short current and 200V open circuir voltage

If using WPT system to power up the driver system, the existing technology is already enough to provide enough power. A battery is necessary in WPT system to store the energy shown in Figure 4.11. Considering the implanting application, the size of battery should be as small as possible. In this case, an 100mAh Li-ion battery with a typical voltage of 3.6 V is used. This battery can store 1269 J energy, which can support 270 flash.

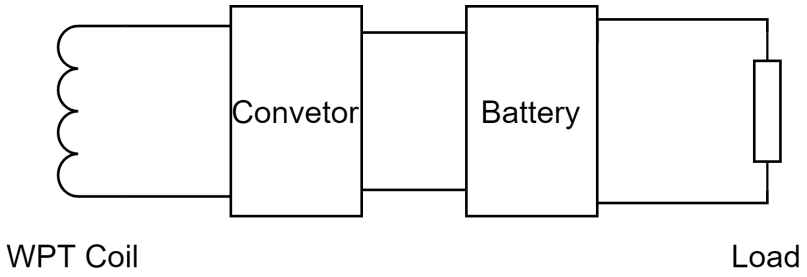

Figure 4.11: A WPT power system with energy storage battery

Comparing these two self-powered technologies, NGs will not rely on external devices after implanting, while the WPT system needs charging at certain time intervals. However, WPT can provide higher power if the LED matrix needs to be turned on more frequently.

4.6 CONCLUSION

As a result, self-powered design is feasible for the advanced optoelectronics driver system designs by reviewing existing researches. Not only the bio-sensors can be self-powered, but also the optoelectronics devices. A suitable self-powering method should be chosen depending on the application. If the LED is only triggered rarely, NGs will be a good choice. On the contrary, WPT technology can be applied when LED is needed more frequently.

5 CONCLUSION

The main goal of this thesis work is to develop a design methodology of advanced optoelectronics driver system for biomedical applications. This methodology will fill the blank area of optoelectronics drivers designed especially for complex biomedical applications. To fulfill the opto-biomedical experiments demand, the driver system should reach the following requirements: quick response speed; enough intensity; precise control; complex logic; customized pattern; user friendly; self-powered.

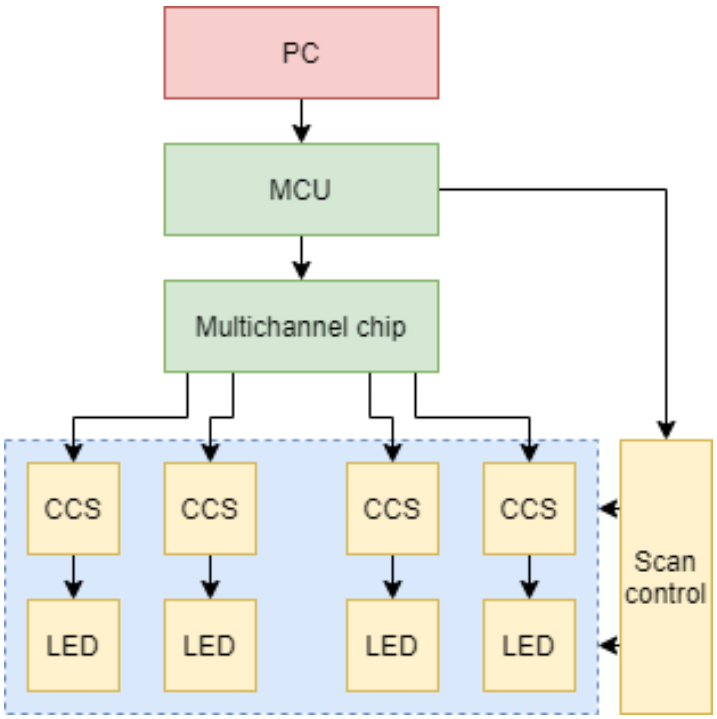

Figure 5.1: Design methodology of advnced optoelectronics driver system for biomedical applications

After the research work, a verified methodology was proposed. Shown in Figure 5.1, *controlable CCSs in conbination with multichannel indication LED control chip is adoped as the core control method*. CCSs controls the current through each LED individually according to the output of LED control chip. The multichannel LED control chips are controlled by MCUs, the MCU will receive control data from PC, perform LED logic control, and control the scan driver. Each part of the system is not coupled with the other parts, which makes the system easy to test and design. Using this

methodology, two fully functional test platforms were designed for special biomedical applications and successfully performed the UVC virus inactivation test and optogenetices sitmulation test. These two driver systems fulfilled the first 6 requirements. Moreover, a literature review is performed to prove the self-powered driver system's feasibility.

During the design process, the first system *UVC virus inactivation test platform* is designed to verfiy the array control methodology. Virus inactivation experimnets were scussfully performed in Erasmus MC using this platform. Based on array control method, stacking multiple array together makes a matrix, which is second system *Interactive optoelectronics system*. This system is aiming to stimulate optogenetices cell mono layers. Using row-column scan control, turn on one row each moment and switch through all rows to drive a matrix. AF termination test was scussfully performed on this platform in LUMC. Finally, after verifying all designed driver systems, self-powered method should be designed for the driver system. By reviewing recent works of nanogenerator technology and wireless power transfer technology, it is feasible to power up the driver using these technologies depending on the energy requirement.

The challenge of this thesis work is balancing light intensity and logic complexity. It is easy to drive a single high power light source like car headlights or complex LED matrix like OLED screen. The LED used in *Interactive optoelectronics system* is >3 W each, higher than the total power consumption of a smartphone. The matrix has 256 such LEDs and reaches a refresh speed of 125Hz. Conventional LED matrix controllers only have a total output capacity of 3W maximum, the combination of multichannel LED controller and high power CCSs is the key method to solve this problem.

To conclude, the optoelectronics driver system methodology put forward in this thesis was a successful guideline to design an advanced optoelectronics driver system for biomedical applications. New drivers for other biomedical applications can also be designed using this methodology.

However, there are still some drawbacks existing. The size of the driver module is still not small enough for future implantation applications. Further optimization is still required to diminish the driver size. Moreover, the self-powered research is still in the theoretical stage. More research is needed to determine the best powering method before the biomedical optoelectronics system is fully implantable.

BIBLIOGRAPHY

[1] E. C. Nyns, R. H. Poelma, L. Volkers, J. J. Plomp, C. I. Bart, A. M. Kip, T. J. van Brakel, K. Zeppenfeld, M. J. Schalij, G. Q. Zhang *et al.*, "An automated hybrid bioelectronic system for autogenous restoration of sinus rhythm in atrial fibrillation," *Science translational medicine*, vol. 11, no. 481, 2019.

[2] B. Calgua, A. Carratala, L. Guerrero-Latorre, A. de Abreu Corrêa, T. Kohn, R. Sommer, and R. Girones, "Uvc inactivation of dsdna and ssrna viruses in water: Uv fluences and a qpcr-based approach to evaluate decay on viral infectivity," *Food and environmental virology*, vol. 6, no. 4, pp. 260–268, 2014.

[3] D.-K. Kim and D.-H. Kang, "Uvc led irradiation effectively inactivates aerosolized viruses, bacteria, and fungi in a chamber-type air disinfection system," *Applied and environmental microbiology*, vol. 84, no. 17, 2018.

[4] B. Bera, "Literature review on triboelectric nanogenerator," *Imperial Journal of Interdisciplinary Research (IJIR)*, vol. 2, no. 10, pp. 1263–1271, 2016.

[5] N. Koch, *Supramolecular materials for opto-electronics*. Royal Society of Chemistry, 2014.

[6] A. Downes and T. P. Blunt, "Iv. on the influence of light upon protoplasm," *Proceedings of the Royal Society of London*, vol. 28, no. 190-195, pp. 199–212, 1879.

[7] A. J. Lewy, T. A. Wehr, F. K. Goodwin, D. A. Newsome, and S. Markey, "Light suppresses melatonin secretion in humans," *Science*, vol. 210, no. 4475, pp. 1267–1269, 1980.

[8] A. J. Lewy, H. A. Kern, N. E. Rosenthal, and T. A. Wehr, "Bright artificial light treatment of a manic-depressive patient with a seasonal mood cycle." *The American journal of psychiatry*, 1982.

[9] N. E. Rosenthal, D. A. Sack, J. C. Gillin, A. J. Lewy, F. K. Goodwin, Y. Davenport, P. S. Mueller, D. A. Newsome, and T. A. Wehr, "Seasonal affective disorder: a description of the syndrome and preliminary findings with light therapy," *Archives of general psychiatry*, vol. 41, no. 1, pp. 72–80, 1984.

[10] C. A. Czeisler, J. S. Allan, S. H. Strogatz, J. M. Ronda, R. Sanchez, C. D. Rios, W. O. Freitag, G. S. Richardson, and R. E. Kronauer, "Bright light resets the human circadian pacemaker independent of the timing of the sleep-wake cycle," *Science*, vol. 233, no. 4764, pp. 667–671, 1986.

[11] A. J. Lewy, R. L. Sack, L. S. Miller, and T. M. Hoban, "Antidepressant and circadian phase-shifting effects of light," *Science*, vol. 235, no. 4786, pp. 352–354, 1987.

[12] J. Perera, "The healing laser comes into the limelight," 1987.

[13] V. Sigurdsson, A. Knulst, and H. Van Weelden, "Phototherapy of acne vulgaris with visible light," *Dermatology*, vol. 194, no. 3, pp. 256–260, 1997.

[14] K. D. Edwards, "Light emitting diodes," *University of California at Irvine. p. 2. Retrieved January*, vol. 12, 2019.

[15] L. Lang-Bicudo, F. D. P. Eduardo, C. D. P. Eduardo, and D. M. Zezell, "Led phototherapy to prevent mucositis: a case report," *Photomedicine and laser surgery*, vol. 26, no. 6, pp. 609–613, 2008.

[16] S. H. Liew, "Laser hair removal," *American journal of clinical dermatology*, vol. 3, no. 2, pp. 107–115, 2002.

[17] K. D. Desmet, D. A. Paz, J. J. Corry, J. T. Eells, M. T. Wong-Riley, M. M. Henry, E. V. Buchmann, M. P. Connelly, J. V. Dovi, H. L. Liang *et al.*, "Clinical and experimental applications of nir-led photobiomodulation," *Photomedicine and Laser Therapy*, vol. 24, no. 2, pp. 121–128, 2006.

[18] A. V. Corazza, J. Jorge, C. Kurachi, and V. S. Bagnato, "Photobiomodulation on the angiogenesis of skin wounds in rats using different light sources," *Photomedicine and laser surgery*, vol. 25, no. 2, pp. 102–106, 2007.

[19] W. Lim, S. Lee, I. Kim, M. Chung, M. Kim, H. Lim, J. Park, O. Kim, and H. Choi, "The anti-inflammatory mechanism of 635 nm light-emitting-diode irradiation compared with existing cox inhibitors," *Lasers in Surgery and Medicine: The Official Journal of the American Society for Laser Medicine and Surgery*, vol. 39, no. 7, pp. 614–621, 2007.

[20] M. A. D. Agnol, R. A. Nicolau, C. J. de Lima, and E. Munin, "Comparative analysis of coherent light action (laser) versus non-coherent light (light-emitting diode) for tissue repair in diabetic rats," *Lasers in medical science*, vol. 24, no. 6, pp. 909–916, 2009.

[21] G. Glickman, B. Byrne, C. Pineda, W. W. Hauck, and G. C. Brainard, "Light therapy for seasonal affective disorder with blue narrow-band light-emitting diodes (leds)," *Biological psychiatry*, vol. 59, no. 6, pp. 502–507, 2006.

[22] T. Tokuda, T. Noda, K. Sasagawa, and J. Ohta, "Optoelectronics devices for biomedical applications," in *Conference on Lasers and Electro-Optics/Pacific Rim*. Optical Society of America, 2013, p. TuJ1_1.

[23] M. Eickmann, U. Gravemann, W. Handke, F. Tolksdorf, S. Reichenberg, T. H. Müller, and A. Seltsam, "Inactivation of ebola virus and middle east respiratory syndrome coronavirus in platelet concentrates and plasma by ultraviolet c light and methylene blue plus visible light, respectively," *Transfusion*, vol. 58, no. 9, pp. 2202–2207, 2018.

[24] J. Casamayor, D. Su, and M. Sarshar, "Extending the lifespan of led-lighting products," *Architectural Engineering and Design Management*, vol. 11, no. 2, pp. 105–122, 2015.

[25] E. A. Pelaez and E. R. Villegas, "Led power reduction trade-offs for ambulatory pulse oximetry," in *2007 29th Annual International Conference of the IEEE Engineering in Medicine and Biology Society*. IEEE, 2007, pp. 2296–2299.

[26] H. E. Lee, J. H. Shin, J. H. Park, S. K. Hong, S. H. Park, S. H. Lee, J. H. Lee, I.-S. Kang, and K. J. Lee, "Micro light-emitting diodes for display and flexible biomedical applications," *Advanced Functional Materials*, vol. 29, no. 24, p. 1808075, 2019.

[27] N. G. Yeh, C.-H. Wu, and T. C. Cheng, "Light-emitting diodes—their potential in biomedical applications," *Renewable and Sustainable Energy Reviews*, vol. 14, no. 8, pp. 2161–2166, 2010.

[28] C.-A. Cheng, H.-L. Cheng, and T.-Y. Chung, "A novel single-stage high-power-factor led street-lighting driver with coupled inductors," *IEEE Transactions on Industry Applications*, vol. 50, no. 5, pp. 3037–3045, 2014.

[29] X. Zhang, P. Li, X. Zou, J. Jiang, S. H. Yuen, C. W. Tang, and K. M. Lau, "Active matrix monolithic led micro-display using gan-on-si epilayers," *IEEE Photonics Technology Letters*, vol. 31, no. 11, pp. 865–868, 2019.

[30] H. HABIB, *Sterilization & Disinfection*, 1980.

[31] S. S. Block, *Disinfection, sterilization, and preservation*. Lippincott Williams & Wilkins, 2001.

[32] T. Bintsis, E. Litopoulou-Tzanetaki, and R. K. Robinson, "Existing and potential applications of ultraviolet light in the food industry–a critical review," *Journal of the Science of Food and Agriculture*, vol. 80, no. 6, pp. 637–645, 2000.

[33] J. R. Bolton and C. A. Cotton, *The ultraviolet disinfection handbook*. American Water Works Association, 2011.

[34] A. P. French, *An introduction to quantum physics*. Routledge, 2018.

[35] C. Bowker, A. Sain, M. Shatalov, and J. Ducoste, "Microbial uv fluence-response assessment using a novel uv-led collimated beam system," *Water research*, vol. 45, no. 5, 2011.

[36] S. Vilhunen and M. Sillanpää, "Recent developments in photochemical and chemical aops in water treatment: a mini-review," *Reviews in Environmental Science and Bio/Technology*, vol. 9, no. 4, pp. 323–330, 2010.

[37] S. E. Beck, H. Ryu, L. A. Boczek, J. L. Cashdollar, K. M. Jeanis, J. S. Rosenblum, O. R. Lawal, and K. G. Linden, "Evaluating uv-c led disinfection performance and investigating potential dual-wavelength synergy," *Water research*, vol. 109, pp. 207–216, 2017.

[38] B. Calgua, A. Carratala, L. Guerrero-Latorre, A. de Abreu Corrêa, T. Kohn, R. Sommer, and R. Girones, "Uvc inactivation of dsdna and ssrna viruses in water: Uv fluences and a qpcr-based approach to evaluate decay on viral infectivity," *Food and environmental virology*, vol. 6, no. 4, pp. 260–268, 2014.

[39] D.-K. Kim, S.-J. Kim, and D.-H. Kang, "Inactivation modeling of human enteric virus surrogates, ms2, q, and x174, in water using uvc-leds, a novel disinfecting system," *Food Research International*, vol. 91, pp. 115–123, 2017.

[40] S. Bernhard, R. Dieter, N. Joachim, S. Marc, R. Martin, and S. Bernd, "Flexible flat cable (ffc) for mounting conduction paths on flexible carrier material, uses integrated electrical functional component for directly contacting conduction path," 2002.

[41] M. Alli, M. Mahalingam, and J. Andrews, "Thermal characteristics of plastic small outline transistor (sot) packages," *IEEE Transactions on Components, Hybrids, and Manufacturing Technology*, vol. 9, no. 4, pp. 353–363, 1986.

[42] K. Deisseroth, G. Feng, A. K. Majewska, G. Miesenböck, A. Ting, and M. J. Schnitzer, "Next-generation optical technologies for illuminating genetically targeted brain circuits," *Journal of Neuroscience*, vol. 26, no. 41, pp. 10 380–10 386, 2006.

[43] G. P. Pathak, J. D. Vrana, and C. L. Tucker, "Optogenetic control of cell function using engineered photoreceptors," *Biology of the Cell*, vol. 105, no. 2, pp. 59–72, 2013.

[44] A. Hoffmann, V. Hildebrandt, J. Heberle, and G. Büldt, "Photoactive mitochondria: in vivo transfer of a light-driven proton pump into the inner mitochondrial membrane of schizosaccharomyces pombe," *Proceedings of the National Academy of Sciences*, vol. 91, no. 20, pp. 9367–9371, 1994.

[45] B. V. Zemelman, G. A. Lee, M. Ng, and G. Miesenböck, "Selective photostimulation of genetically charged neurons," *Neuron*, vol. 33, no. 1, pp. 15–22, 2002.

[46] B. O. Bingen, M. C. Engels, M. J. Schalij, W. Jangsangthong, Z. Neshati, I. Feola, D. L. Ypey, S. F. Askar, A. V. Panfilov, D. A. Pijnappels *et al.*, "Light-induced termination of spiral wave arrhythmias by optogenetic engineering of atrial cardiomyocytes," *Cardiovascular research*, vol. 104, no. 1, pp. 194–205, 2014.

[47] E. C. Nyns, A. Kip, C. I. Bart, J. J. Plomp, K. Zeppenfeld, M. J. Schalij, A. A. de Vries, and D. A. Pijnappels, "Optogenetic termination of ventricular arrhythmias in the whole heart: towards biological cardiac rhythm management," *European heart journal*, vol. 38, no. 27, pp. 2132–2136, 2017.

[48] C. Crocini, C. Ferrantini, R. Coppini, M. Scardigli, P. Yan, L. M. Loew, G. Smith, E. Cerbai, C. Poggesi, F. S. Pavone *et al.*, "Optogenetics design of mechanistically-based stimulation patterns for cardiac defibrillation," *Scientific reports*, vol. 6, no. 1, pp. 1–7, 2016.

[49] D. Peng, K. Zhang, and Z. Liu, "Design and fabrication of fine-pitch pixelated-addressed micro-led arrays on printed circuit board for display and communication applications," *IEEE Journal of the Electron Devices Society*, vol. 5, no. 1, pp. 90–94, 2016.

[50] M. Coltheart, "Iconic memory and visible persistence," *Perception & psychophysics*, vol. 27, no. 3, pp. 183–228, 1980.

[51] "Ieee standard serial interface for programmable instrumentation," *IEEE Std 1174-2000*, pp. 1–40, 2001.

[52] "Ieee standard for information technology– local and metropolitan area networks– specific requirements– part 11: Wireless lan medium access control (mac) and physical layer (phy) specifications: Further higher data rate extension in the 2.4 ghz band," *IEEE Std 802.11g-2003 (Amendment to IEEE Std 802.11, 1999 Edn. (Reaff 2003) as amended by IEEE Stds 802.11a-1999, 802.11b-1999, 802.11b-1999/Cor 1-2001, and 802.11d-2001)*, pp. 1–104, 2003.

[53] Y. Hong, X.-L. Cheng, G.-J. Liu, D.-S. Hong, S.-S. He, B.-J. Wang, X.-M. Sun, and H.-S. Peng, "One-step production of continuous supercapacitor fibers for a flexible power textile," *Chinese Journal of Polymer Science*, vol. 37, no. 8, pp. 737–743, 2019.

[54] B. Shi, Z. Liu, Q. Zheng, J. Meng, H. Ouyang, Y. Zou, D. Jiang, X. Qu, M. Yu, L. Zhao *et al.*, "Body-integrated self-powered system for wearable and implantable applications," *ACS nano*, vol. 13, no. 5, pp. 6017–6024, 2019.

[55] J. Xu, Z. Ku, Y. Zhang, D. Chao, and H. J. Fan, "Integrated photo-supercapacitor based on pedot modified printable perovskite solar cell," *Advanced Materials Technologies*, vol. 1, no. 5, p. 1600074, 2016.

[56] X. Wang, S. Wang, Y. Yang, and Z. L. Wang, "Hybridized electromagnetic–triboelectric nanogenerator for scavenging air-flow energy to sustainably power temperature sensors," *ACS nano*, vol. 9, no. 4, pp. 4553–4562, 2015.

[57] A. J. Bandodkar and J. Wang, "Wearable biofuel cells: a review," *Electroanalysis*, vol. 28, no. 6, pp. 1188–1200, 2016.

[58] V. Leonov and R. J. Vullers, "Wearable electronics self-powered by using human body heat: The state of the art and the perspective," *Journal of Renewable and Sustainable Energy*, vol. 1, no. 6, p. 062701, 2009.

[59] Z. L. Wang and J. Song, "Piezoelectric nanogenerators based on zinc oxide nanowire arrays," *Science*, vol. 312, no. 5771, pp. 242–246, 2006.

[60] Z. Zhang, H. Pang, A. Georgiadis, and C. Cecati, "Wireless power transfer—an overview," *IEEE Transactions on Industrial Electronics*, vol. 66, no. 2, pp. 1044–1058, 2018.

[61] Z. Lin, Z. Wu, B. Zhang, Y.-C. Wang, H. Guo, G. Liu, C. Chen, Y. Chen, J. Yang, and Z. L. Wang, "A triboelectric nanogenerator-based smart insole for multifunctional gait monitoring," *Advanced Materials Technologies*, vol. 4, no. 2, p. 1800360, 2019.

[62] C. Zhang, K. Dai, D. Liu, F. Yi, X. Wang, L. Zhu, and Z. You, "Ultralow quiescent power-consumption wake-up technology based on the bionic triboelectric nanogenerator," *Advanced Science*, vol. 7, no. 12, p. 2000254, 2020.

[63] E. Nemati, M. J. Deen, and T. Mondal, "A wireless wearable ecg sensor for long-term applications," *IEEE Communications Magazine*, vol. 50, no. 1, pp. 36–43, 2012.

[64] F. R. Fan, W. Tang, and Z. L. Wang, "Flexible nanogenerators for energy harvesting and self-powered electronics," *Advanced Materials*, vol. 28, no. 22, pp. 4283–4305, 2016.

[65] X. Yu, Y. Fu, X. Cai, H. Kafafy, H. Wu, M. Peng, S. Hou, Z. Lv, S. Ye, and D. Zou, "Flexible fiber-type zinc–carbon battery based on carbon fiber electrodes," *Nano Energy*, vol. 2, no. 6, pp. 1242–1248, 2013.

[66] Y. Zhang, Y. Liu, and Z. L. Wang, "Fundamental theory of piezotronics," *Advanced Materials*, vol. 23, no. 27, pp. 3004–3013, 2011.

[67] Z. Li, G. Zhu, R. Yang, A. C. Wang, and Z. L. Wang, "Muscle-driven in vivo nanogenerator," *Advanced materials*, vol. 22, no. 23, pp. 2534–2537, 2010.

[68] F.-R. Fan, Z.-Q. Tian, and Z. L. Wang, "Flexible triboelectric generator," *Nano energy*, vol. 1, no. 2, pp. 328–334, 2012.

[69] V. Nguyen, R. Zhu, and R. Yang, "Environmental effects on nanogenerators," *Nano Energy*, vol. 14, pp. 49–61, 2015.

[70] A. Diaz and R. Felix-Navarro, "A semi-quantitative tribo-electric series for polymeric materials: the influence of chemical structure and properties," *Journal of Electrostatics*, vol. 62, no. 4, pp. 277–290, 2004.

[71] S. Hersh and D. Montgomery, "Static electrification of filaments: experimental techniques and results," *Textile Research Journal*, vol. 25, no. 4, pp. 279–295, 1955.

[72] C. K. Adams, *Nature's electricity*. Blue Ridge Summit, PA: Tab Books, 1987, 1987, no. 537 A211n.

[73] S. S. Kwak, H. Kim, W. Seung, J. Kim, R. Hinchet, and S.-W. Kim, "Fully stretchable textile triboelectric nanogenerator with knitted fabric structures," *ACS nano*, vol. 11, no. 11, pp. 10 733–10 741, 2017.

[74] M. Sala de Medeiros, D. Chanci, C. Moreno, D. Goswami, and R. V. Martinez, "Waterproof, breathable, and antibacterial self-powered e-textiles based on omniphobic triboelectric nanogenerators," *Advanced Functional Materials*, vol. 29, no. 42, p. 1904350, 2019.

[75] L. Zhou, D. Liu, S. Li, Z. Zhao, C. Zhang, X. Yin, L. Liu, S. Cui, Z. L. Wang, and J. Wang, "Rationally designed dual-mode triboelectric nanogenerator for harvesting mechanical energy by both electrostatic induction and dielectric breakdown effects," *Advanced Energy Materials*, vol. 10, no. 24, p. 2000965, 2020.

[76] Y. Yang, H. Zhang, J. Chen, Q. Jing, Y. S. Zhou, X. Wen, and Z. L. Wang, "Single-electrode-based sliding triboelectric nanogenerator for self-powered displacement vector sensor system," *Acs Nano*, vol. 7, no. 8, pp. 7342–7351, 2013.

[77] H. Wang, T. Wu, Q. Zeng, and C. Lee, "A review and perspective for the development of triboelectric nanogenerator (teng)-based self-powered neuroprosthetics," *Micromachines*, vol. 11, no. 9, p. 865, 2020.

[78] D. Zhang, K. Zhang, Y. Wang, Y. Wang, and Y. Yang, "Thermoelectric effect induced electricity in stretchable graphene-polymer nanocomposites for ultrasensitive self-powered strain sensor system," *Nano energy*, vol. 56, pp. 25–32, 2019.

[79] S. Price, "The peltier effect and thermoelectric cooling," *WWW-dokumentti. Saatavilla: http://ffden-2. phys. uaf. edu/212_spring2007. web. dir/sedona_price/phys_212_webproj_peltier. html [viitattu 20.5. 2017]*, 2007.

[80] M. Pinuela, D. C. Yates, S. Lucyszyn, and P. D. Mitcheson, "Maximizing dc-to-load efficiency for inductive power transfer," *IEEE transactions on power electronics*, vol. 28, no. 5, pp. 2437–2447, 2012.

[81] S. R. Cove, M. Ordonez, N. Shafiei, and J. Zhu, "Improving wireless power transfer efficiency using hollow windings with track-width-ratio," *IEEE Transactions on Power Electronics*, vol. 31, no. 9, pp. 6524–6533, 2015.

[82] S. Moon, B.-C. Kim, S.-Y. Cho, C.-H. Ahn, and G.-W. Moon, "Analysis and design of a wireless power transfer system with an intermediate coil for high efficiency," *IEEE Transactions on Industrial Electronics*, vol. 61, no. 11, pp. 5861–5870, 2014.

[83] H. Li, J. Li, K. Wang, W. Chen, and X. Yang, "A maximum efficiency point tracking control scheme for wireless power transfer systems using magnetic resonant coupling," *IEEE Transactions on Power Electronics*, vol. 30, no. 7, pp. 3998–4008, 2014.

[84] A. P. Sample, D. T. Meyer, and J. R. Smith, "Analysis, experimental results, and range adaptation of magnetically coupled resonators for wireless power transfer," *IEEE Transactions on industrial electronics*, vol. 58, no. 2, pp. 544–554, 2010.

[85] X. Lu, D. Niyato, P. Wang, D. I. Kim, and Z. Han, "Wireless charger networking for mobile devices: Fundamentals, standards, and applications," *IEEE Wireless Communications*, vol. 22, no. 2, pp. 126–135, 2015.

[86] R. Tseng, B. Von Novak, S. Shevde, and K. A. Grajski, "Introduction to the alliance for wireless power loosely-coupled wireless power transfer system specification version 1.0," in *2013 IEEE Wireless Power Transfer (WPT)*. IEEE, 2013, pp. 79–83.

[87] X. Wang, J. Song, J. Liu, and Z. L. Wang, "Direct-current nanogenerator driven by ultrasonic waves," *Science*, vol. 316, no. 5821, pp. 102–105, 2007.

[88] Y. Qin, X. Wang, and Z. L. Wang, "Microfibre–nanowire hybrid structure for energy scavenging," *nature*, vol. 451, no. 7180, pp. 809–813, 2008.

[89] R. Yang, Y. Qin, L. Dai, and Z. L. Wang, "Power generation with laterally packaged piezoelectric fine wires," *Nature nanotechnology*, vol. 4, no. 1, pp. 34–39, 2009.

[90] G. Zhu, R. Yang, S. Wang, and Z. L. Wang, "Flexible high-output nanogenerator based on lateral zno nanowire array," *Nano letters*, vol. 10, no. 8, pp. 3151–3155, 2010.

[91] S. Xu, Y. Qin, C. Xu, Y. Wei, R. Yang, and Z. L. Wang, "Self-powered nanowire devices," *Nature nanotechnology*, vol. 5, no. 5, pp. 366–373, 2010.

[92] S. Cha, S. M. Kim, H. Kim, J. Ku, J. I. Sohn, Y. J. Park, B. G. Song, M. H. Jung, E. K. Lee, B. L. Choi *et al.*, "Porous pvdf as effective sonic wave driven nanogenerators," *Nano letters*, vol. 11, no. 12, pp. 5142–5147, 2011.

[93] G. Zhu, A. C. Wang, Y. Liu, Y. Zhou, and Z. L. Wang, "Functional electrical stimulation by nanogenerator with 58 v output voltage," *Nano letters*, vol. 12, no. 6, pp. 3086–3090, 2012.

[94] S. K. Ghosh and D. Mandal, "High-performance bio-piezoelectric nanogenerator made with fish scale," *Applied Physics Letters*, vol. 109, no. 10, p. 103701, 2016.

[95] H. Xu, T.-G. Lee, S.-J. Park, B.-Y. Kim, and S. Nahm, "Sodium-potassium niobate nanorods with various crystal structures and their application to nanogenerator," *Journal of the American Ceramic Society*, vol. 100, no. 4, pp. 1673–1681, 2017.

[96] G. Zhu, C. Pan, W. Guo, C.-Y. Chen, Y. Zhou, R. Yu, and Z. L. Wang, "Triboelectric-generator-driven pulse electrodeposition for micropatterning," *Nano letters*, vol. 12, no. 9, pp. 4960–4965, 2012.

[97] J. Chen, G. Zhu, W. Yang, Q. Jing, P. Bai, Y. Yang, T.-C. Hou, and Z. L. Wang, "Harmonic-resonator-based triboelectric nanogenerator as a sustainable power source and a self-powered active vibration sensor," *Advanced materials*, vol. 25, no. 42, pp. 6094–6099, 2013.

[98] Y. Hu, J. Yang, Q. Jing, S. Niu, W. Wu, and Z. L. Wang, "Triboelectric nanogenerator built on suspended 3d spiral structure as vibration and positioning sensor and wave energy harvester," *ACS nano*, vol. 7, no. 11, pp. 10 424–10 432, 2013.

[99] G. Zhu, J. Chen, Y. Liu, P. Bai, Y. S. Zhou, Q. Jing, C. Pan, and Z. L. Wang, "Linear-grating triboelectric generator based on sliding electrification," *Nano letters*, vol. 13, no. 5, pp. 2282–2289, 2013.

[100] Z.-H. Lin, G. Cheng, S. Lee, K. C. Pradel, and Z. L. Wang, "Harvesting water drop energy by a sequential contact-electrification and electrostatic-induction process," *Advanced Materials*, vol. 26, no. 27, pp. 4690–4696, 2014.

[101] J. Sun, W. Li, G. Liu, W. Li, and M. Chen, "Triboelectric nanogenerator based on biocompatible polymer materials," *The Journal of Physical Chemistry C*, vol. 119, no. 17, pp. 9061–9068, 2015.

[102] T. Huang, M. Lu, H. Yu, Q. Zhang, H. Wang, and M. Zhu, "Enhanced power output of a triboelectric nanogenerator composed of electrospun nanofiber mats doped with graphene oxide," *Scientific reports*, vol. 5, no. 1, pp. 1–8, 2015.

[103] S. W. Chen, X. Cao, N. Wang, L. Ma, H. R. Zhu, M. Willander, Y. Jie, and Z. L. Wang, "An ultrathin flexible single-electrode triboelectric-nanogenerator for mechanical energy harvesting and instantaneous force sensing," *Advanced Energy Materials*, vol. 7, no. 1, p. 1601255, 2017.

[104] S. S. K. Mallineni, Y. Dong, H. Behlow, A. M. Rao, and R. Podila, "A wireless triboelectric nanogenerator," *Advanced Energy Materials*, vol. 8, no. 10, p. 1702736, 2018.

[105] Y. Pang, F. Xi, J. Luo, G. Liu, T. Guo, and C. Zhang, "An alginate film-based degradable triboelectric nanogenerator," *RSC advances*, vol. 8, no. 12, pp. 6719–6726, 2018.

[106] C. Hao, J. He, C. Zhai, W. Jia, L. Song, J. Cho, X. Chou, and C. Xue, "Two-dimensional triboelectric-electromagnetic hybrid nanogenerator for wave energy harvesting," *Nano Energy*, vol. 58, pp. 147–157, 2019.

[107] A. Ahmed, I. Hassan, M. Hedaya, T. A. El-Yazid, J. Zu, and Z. L. Wang, "Farms of triboelectric nanogenerators for harvesting wind energy: A potential approach towards green energy," *Nano Energy*, vol. 36, pp. 21–29, 2017.

[108] E. J. Lee, T. Y. Kim, S.-W. Kim, S. Jeong, Y. Choi, and S. Y. Lee, "High-performance piezoelectric nanogenerators based on chemically-reinforced composites," *Energy & Environmental Science*, vol. 11, no. 6, pp. 1425–1430, 2018.

[109] B. Dudem, D. H. Kim, L. K. Bharat, and J. S. Yu, "Highly-flexible piezoelectric nanogenerators with silver nanowires and barium titanate embedded composite films for mechanical energy harvesting," *Applied Energy*, vol. 230, pp. 865–874, 2018.

[110] N. P. M. J. Raj, N. R. Alluri, G. Khandelwal, and S.-J. Kim, "Lead-free piezoelectric nanogenerator using lightweight composite films for harnessing biomechanical energy," *Composites Part B: Engineering*, vol. 161, pp. 608–616, 2019.

[111] S. S. Valtchev, E. N. Baikova, and L. R. Jorge, "Electromagnetic field as the wireless transporter of energy," *Facta universitatis-series: Electronics and Energetics*, vol. 25, no. 3, pp. 171–181, 2012.

[112] R. Erfani, F. Marefat, A. M. Sodagar, and P. Mohseni, "Transcutaneous capacitive wireless power transfer (c-wpt) for biomedical implants," in *2017 IEEE International Symposium on Circuits and Systems (ISCAS)*. IEEE, 2017, pp. 1–4.

[113] A. Kurs, A. Karalis, R. Moffatt, J. D. Joannopoulos, P. Fisher, and M. Soljačić, "Wireless power transfer via strongly coupled magnetic resonances," *science*, vol. 317, no. 5834, pp. 83–86, 2007.

[114] M. Kiani and M. Ghovanloo, "An rfid-based closed-loop wireless power transmission system for biomedical applications," *IEEE Transactions on Circuits and Systems II: Express Briefs*, vol. 57, no. 4, pp. 260–264, 2010.

[115] O. Knecht, R. Bosshard, and J. W. Kolar, "High-efficiency transcutaneous energy transfer for implantable mechanical heart support systems," *IEEE Transactions on Power Electronics*, vol. 30, no. 11, pp. 6221–6236, 2015.

[116] D. Jiang, D. Cirmirakis, M. Schormans, T. A. Perkins, N. Donaldson, and A. Demosthenous, "An integrated passive phase-shift keying modulator for biomedical implants with power telemetry over a single inductive link," *IEEE transactions on biomedical circuits and systems*, vol. 11, no. 1, pp. 64–77, 2016.

[117] S. A. Mirbozorgi, P. Yeon, and M. Ghovanloo, "Robust wireless power transmission to mm-sized free-floating distributed implants," *IEEE transactions on biomedical circuits and systems*, vol. 11, no. 3, pp. 692–702, 2017.

[118] Y. Wang, D. Ye, L. Lyu, Y. Xiang, H. Min, and C.-J. R. Shi, "A 13.56 mhz wireless power and data transfer receiver achieving 75.4% effective-power-conversion efficiency with 0.1% ask modulation depth and 9.2 mw output power," in *2018 IEEE International Solid-State Circuits Conference-(ISSCC)*. IEEE, 2018, pp. 142–144.

[119] A. Massa, G. Oliveri, F. Viani, and P. Rocca, "Array designs for long-distance wireless power transmission: State-of-the-art and innovative solutions," *Proceedings of the IEEE*, vol. 101, no. 6, pp. 1464–1481, 2013.

[120] A. Sahai and D. Graham, "Optical wireless power transmission at long wavelengths," in *2011 International Conference on Space Optical Systems and Applications (ICSOS)*. IEEE, 2011, pp. 164–170.

[121] G. A. Landis, "Applications for space power by laser transmission," in *Laser Power Beaming*, vol. 2121. International Society for Optics and Photonics, 1994, pp. 252–255.

A UVC LED CONFIGURATION

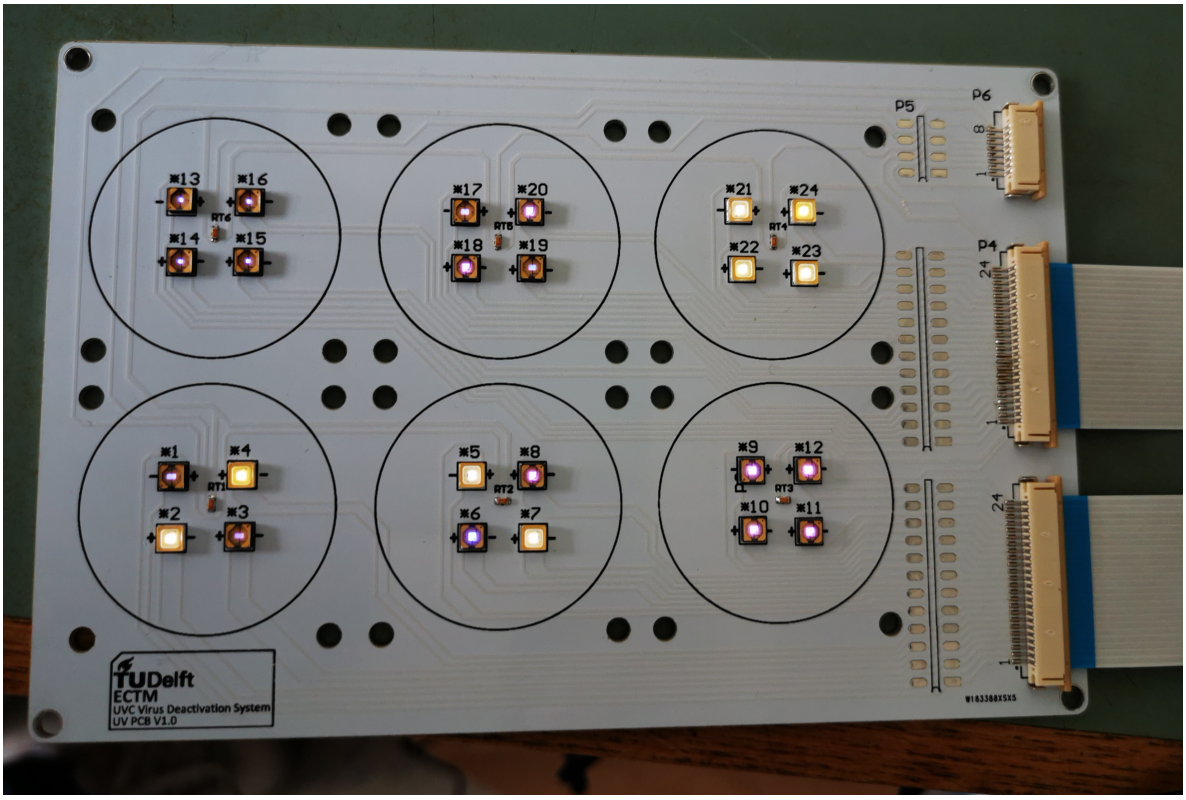

Figure A.1: UVC LED array operation status visible light image of array No.2

UVC LED Array nr.1								
LED nr.	**1**	**2**	**3**	**4**	**5**	**6**	**7**	**8**
λ (nm)	255	278	255	278	265	278	265	278
Max. Id (mA)	30	150	30	150	200	150	200	150
LED nr.	**9**	**10**	**11**	**12**	**13**	**14**	**15**	**16**
λ (nm)	278	285	278	285	255	265	255	265
Max. Id (mA)	150	200	150	200	30	200	30	200
LED nr.	**17**	**18**	**19**	**20**	**21**	**22**	**23**	**24**
λ (nm)	255	285	255	285	265	285	265	285
Max. Id (mA)	30	200	30	200	200	200	200	200

UVC LED Array nr.2								
LED nr.	**1**	**2**	**3**	**4**	**5**	**6**	**7**	**8**
λ (nm)	255	278	255	278	278	285	278	285
Max. Id (mA)	30	150	30	150	150	200	150	200
LED nr.	**9**	**10**	**11**	**12**	**13**	**14**	**15**	**16**
λ (nm)	285	285	285	285	255	255	255	255
Max. Id (mA)	200	200	200	200	30	30	30	30
LED nr.	**17**	**18**	**19**	**20**	**21**	**22**	**23**	**24**
λ (nm)	255	285	255	285	278	278	278	278
Max. Id (mA)	30	200	30	200	150	150	150	150

Figure A.2: The UVC LED configuration of *UVC virus inactivation test platform*

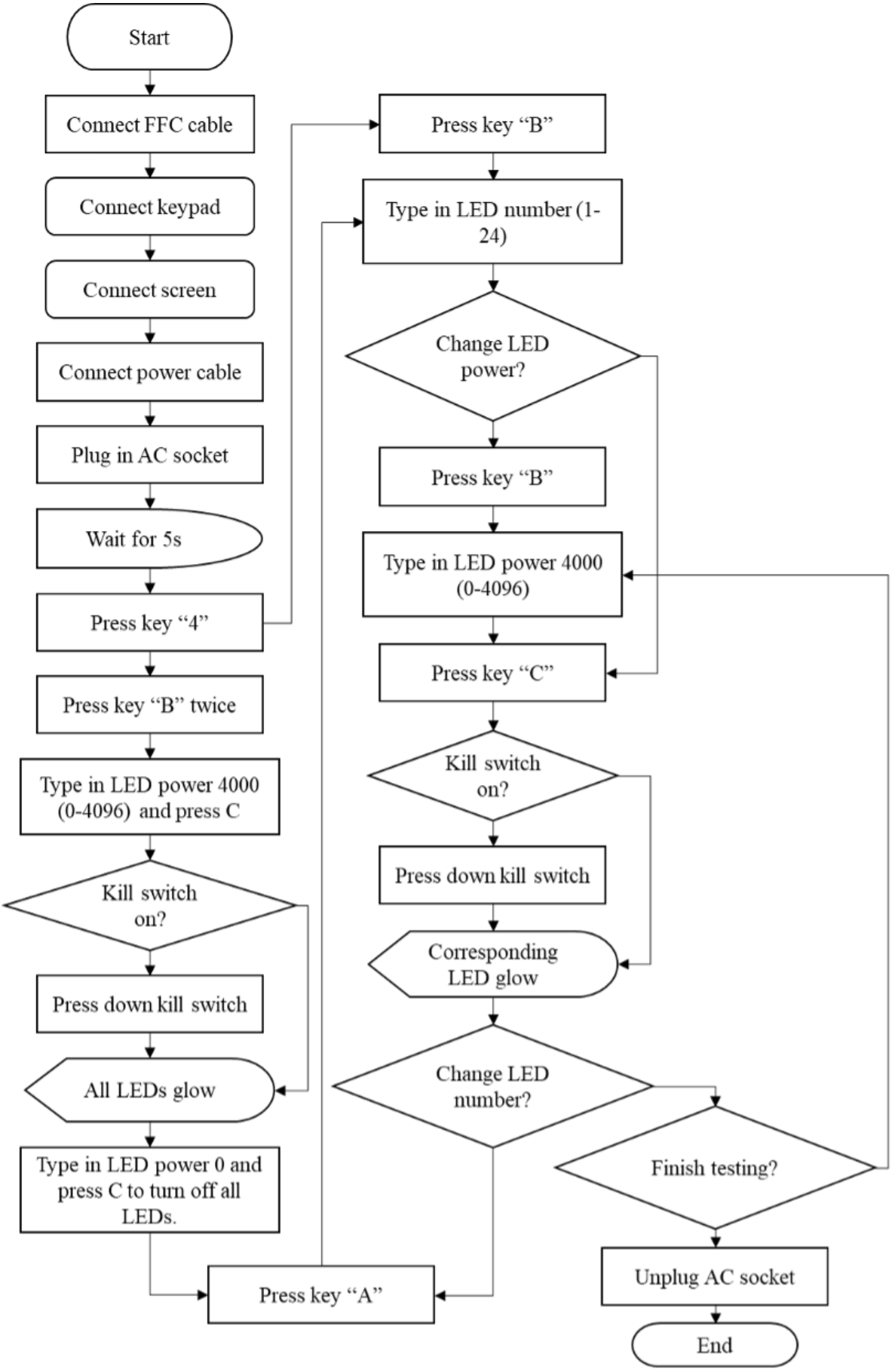

Figure A.3: Test protocol of *UVC virus inactivation test platform*

B DRIVER SCHMATIC FILES

B.1 UVC VIRUS INACTIVATION TEST PLATFORM

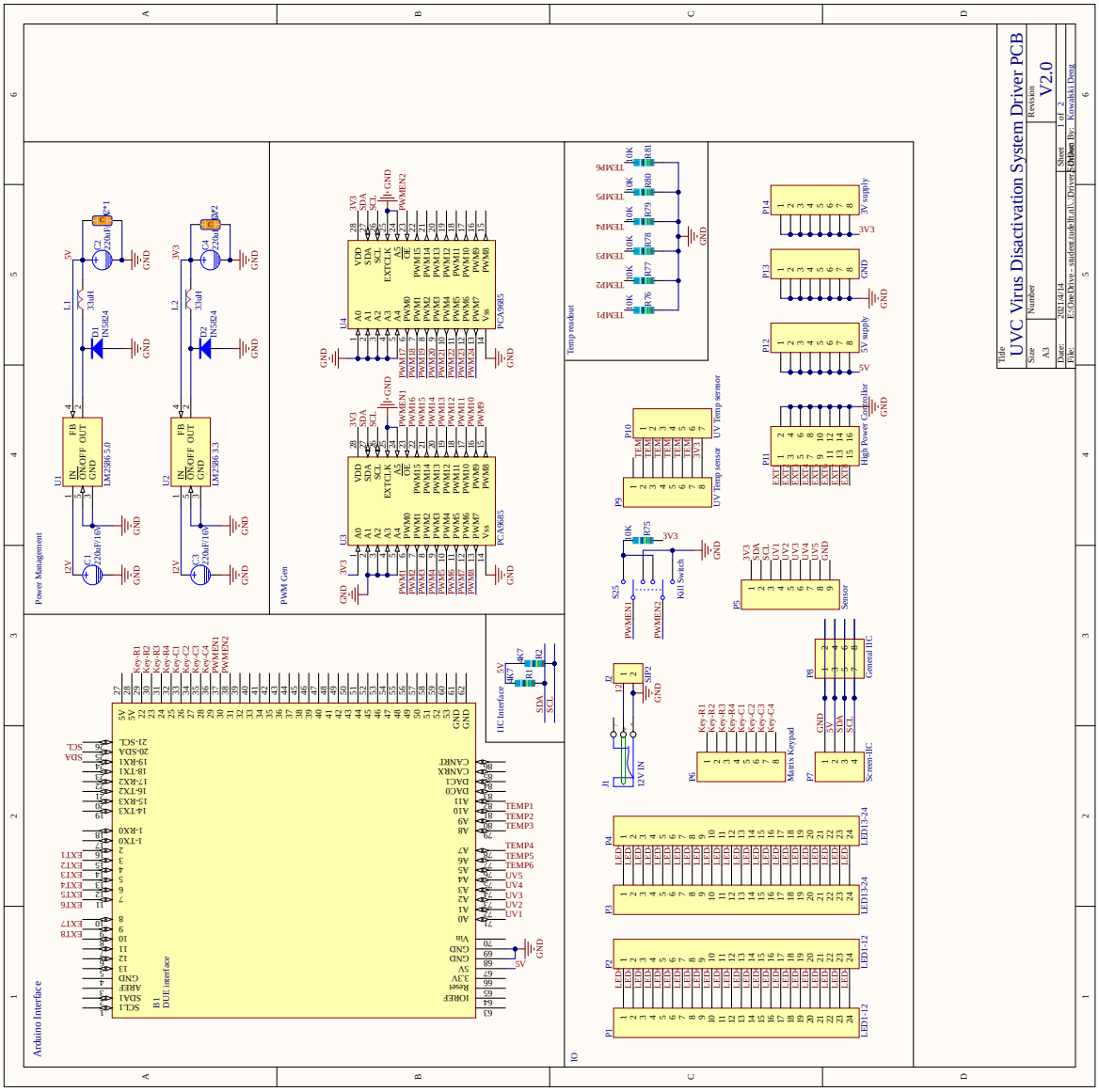

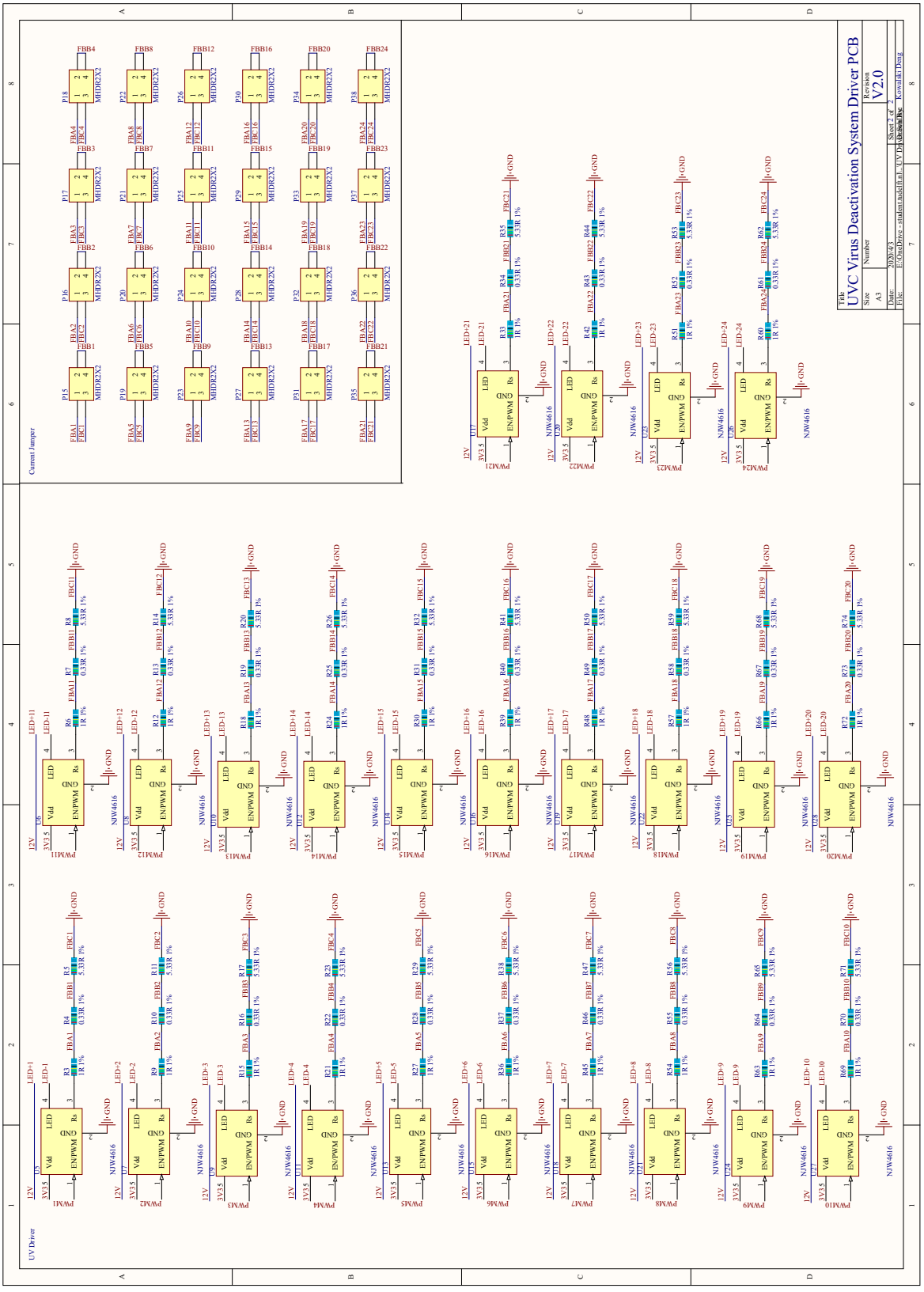

Figure B.1: Schematic file of *UVC Virus Inactivation Test Platform*

B.2 INTERACTIVE OPTOELECTRONICS SYSTEM

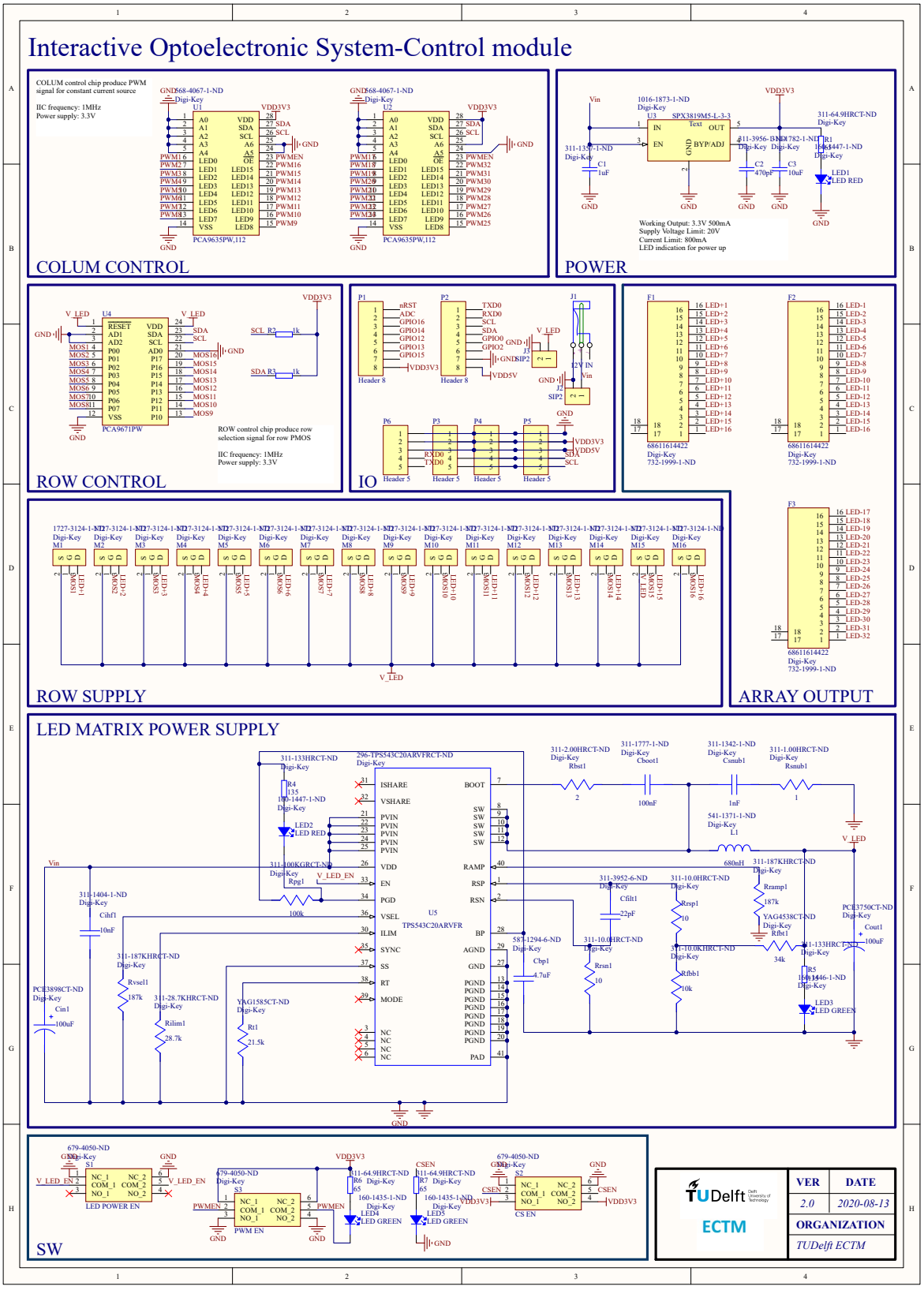

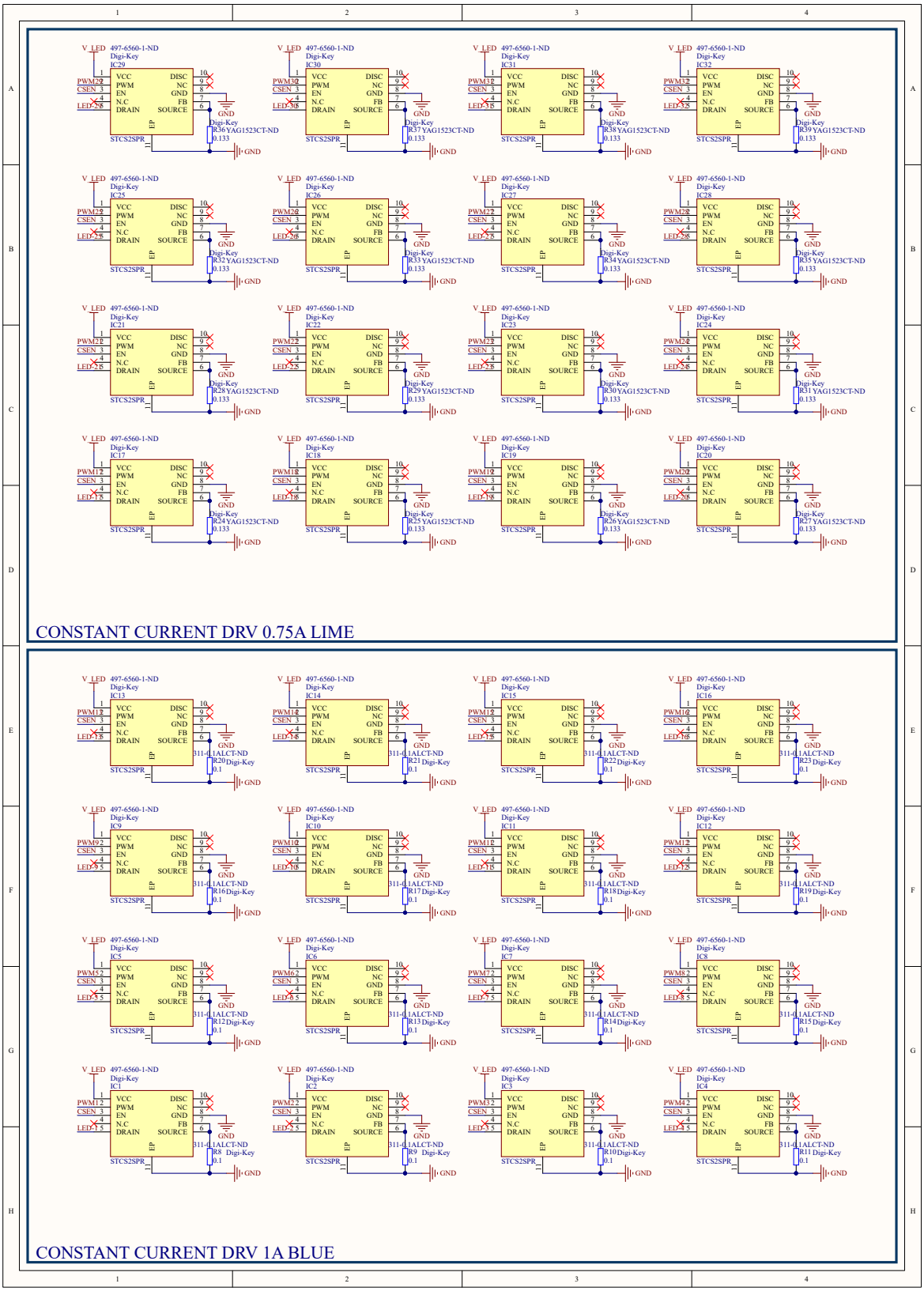

Figure B.2: Schmatic file of *Interactive Optoelectronics System*

C PCB FILES

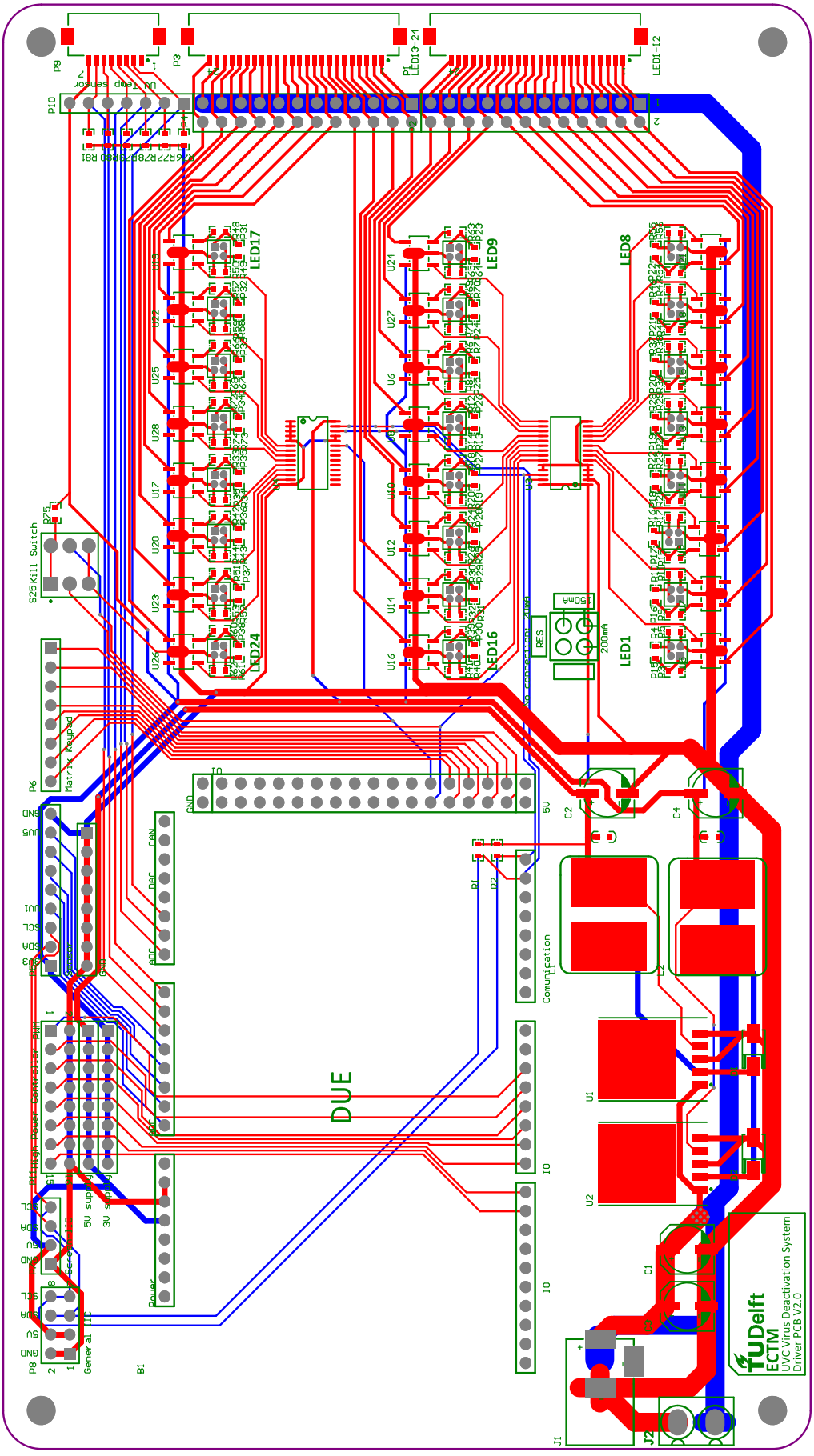

Figure C.1: PCB design file of *UVC Virus Inactivation Test Platform*

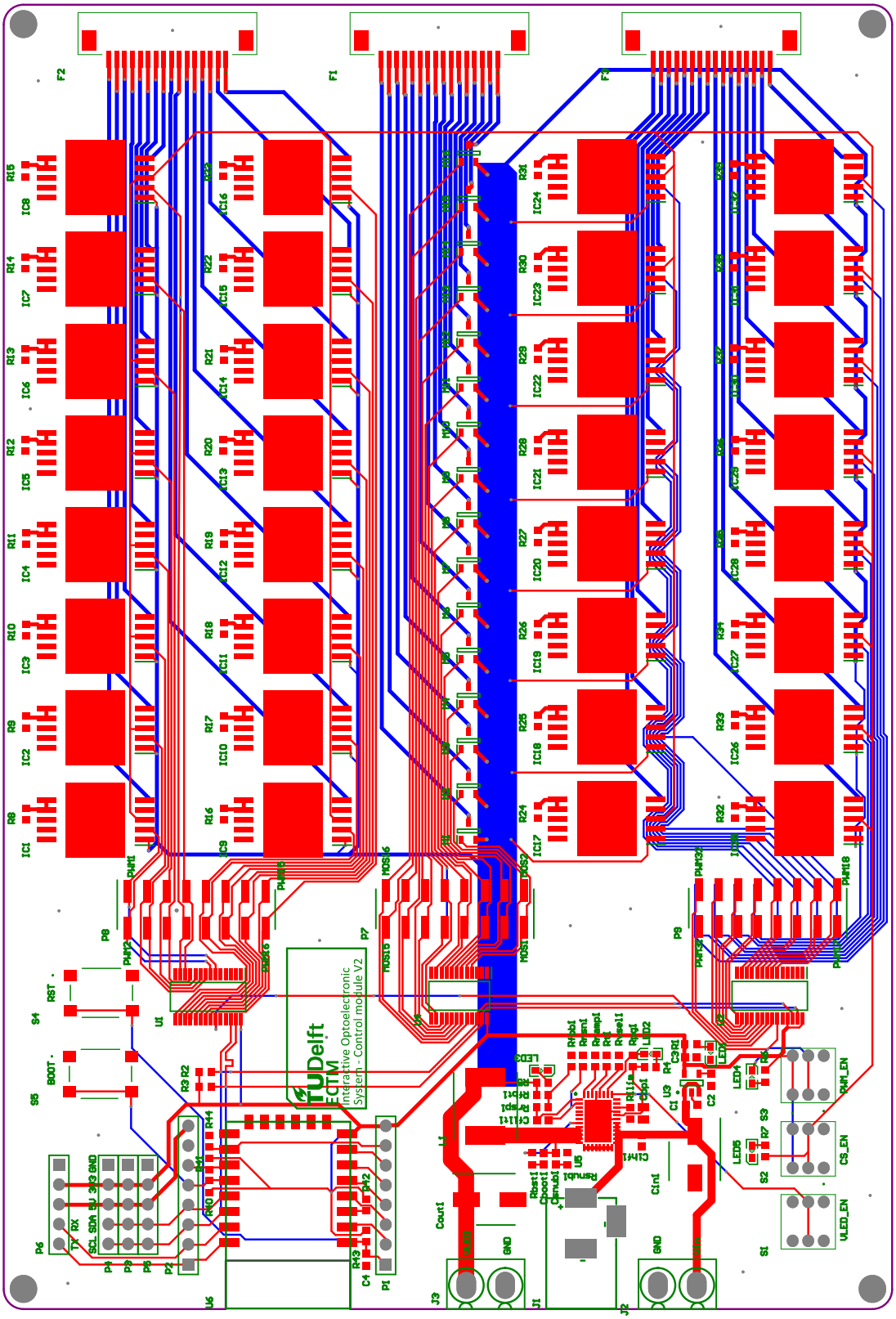

Figure C.2: PCB design file of *Interactive Optoelectronics System*